High-Frequency Asymptotic Methods for Analyzing the EM Scattering by Open-Ended Waveguide Cavities

R.J. Burkholder and P.H. Pathak

The Ohio State University

ElectroScience Laboratory

Department of Electrical Engineering
Columbus, Ohio 43212

METHODS FOR ANALYZING THE EM SCATTERING BY
OPEN-ENDED WAVEGUIDE CAVITIES (Ohio State
Univ.) 271 p   CSCL 20N
                                                                  N90-16100

                                                                  Unclas
                                                 G3/32 0255755

NOTICES

50272-101

REPORT DOCUMENTATION PAGE	1. REPORT NO.	2.	3. Recipient's Accession No.

4. Title and Subtitle

High-Frequency Asymptotic Methods for Analyzing the EM Scattering by Open-Ended Waveguide Cavities

5. Report Date

September 1989

6.

7. Author(s)

R.J. Burkholder and P.H. Pathak

8. Performing Org. Rept. No.

719630-3

9. Performing Organization Name and Address

The Ohio State University

ElectroScience Laboratory

1320 Kinnear Road

Columbus, OH 43212

10. Project/Task/Work Unit No.

11. Contract(C) or Grant(G) No.

(C)

(G) NAG3-476

12. Sponsoring Organization Name and Address

NASA Lewis Research Center

21000 Brookpark Road

Cleveland, Ohio 44135

13. Report Type/Period Covered

Technical Report

14.

15. Supplementary Notes

16. Abstract (Limit: 200 words)

Four high-frequency methods are described for analyzing the electromagnetic (EM) scattering by electrically large open-ended cavities. They are: (1) a hybrid combination of waveguide modal analysis and high-frequency asymptotics, (2) geometrical optics (GO) ray shooting, (3) Gaussian beam (GB) shooting, and (4) the generalized ray expansion (GRE) method. The hybrid modal method gives very accurate results but is limited to cavities which are made up of sections of uniform waveguides for which the modal fields are known. The GO ray shooting method can be applied to much more arbitrary cavity geometries and can handle absorber treated interior walls, but it generally only predicts the major trends of the RCS pattern and not the details. Also, a very large number of rays need to be tracked for each new incidence angle. Like the GO ray shooting method, the GB shooting method can handle more arbitrary cavities, but it is much more efficient and generally more accurate than the GO method because it includes the fields diffracted by the rim at the open end which enter the cavity. However, due to beam divergence effects the GB method is limited to cavities which are not very long compared to their width. The GRE method overcomes the length-to-width limitation of the GB method by replacing the GB's with GO ray tubes which are launched in the same manner as the GB's to include the interior rim diffracted field. This method gives good accuracy and is generally more efficient than the GO method, but a large number of ray tubes need to be tracked.

17. Document Analysis   a. Descriptors

b. Identifiers/Open-Ended Terms

c. COSATI Field/Group

18. Availability Statement

A. Approved for public release; Distribution is unlimited.

19. Security Class (This Report)

Unclassified

20. Security Class (This Page)

Unclassified

21. No. of Pages

270

22. Price

(See ANSI-Z39.18)

See Instructions on Reverse

OPTIONAL FORM 272 (4-77)

Department of Commerce

TABLE OF CONTENTS

iii

PRECEDING PAGE BLANK NOT FILMED

APPENDIX

LIST OF FIGURES

xi

xiv

CHAPTER I

INTRODUCTION

An analysis of the electromagnetic (EM) plane wave scattering by open-ended waveguide cavity configurations is useful for dealing with radar cross-section (RCS) and EM penetration problems. In this report, four different approximate but useful approaches are described for analyzing the high frequency EM scattering by a fairly general class of semi-infinite open-ended waveguide cavities which admit treatment by these methods. The cavities under consideration may contain an interior termination; in addition, the interior cavity walls may be perfectly-conducting with or without a layer of absorbing material coating them, or the walls may be characterized by an impedance boundary condition. For the present analysis, the rim edge at the open end of the cavity is assumed to be sharp and the scattering by the rim is included in addition to the scattering by the interior of the waveguide cavity. All other external scattering features are not of interest and will not be considered in the present work, although in many instances they can be analyzed using the geometrical theory of diffraction (GTD) [1], and its uniform version (UTD) [2,3].

The four different approaches considered in this report for analyzing the EM scattering/penetration by the above class of open-ended waveguide cavities are respectively based on:
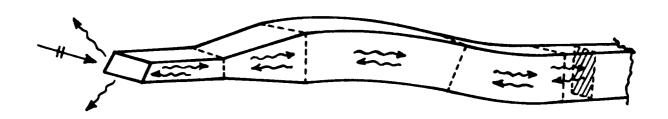
(1) a hybrid combination of asymptotic high frequency and modal methods,

(2) the geometrical optics ray method,

(3) the use of Gaussian beams, and

(4) a generalized ray expansion method.
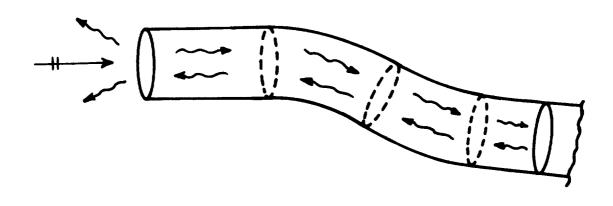
It is noted that a rigorous analysis of the problem under consideration is possible only for a very small number of special cavity shapes, e.g., cavities formed by open-ended semi-infinite parallel plate and circular waveguides with a planar interior termination. Hence, it is necessary to resort to approximate techniques of analysis such as those indicated above. All of these approaches involve the use of high frequency approximations.

The approach based on a hybrid combination of asymptotic and modal techniques, which is employed within the framework of the self-consistent multiple scattering method (or the generalized scattering matrix method) [4], can be applied to efficiently treat the EM scattering by open-ended cavities which can be built up by joining together waveguide sections for which the modes and their corresponding modal rays are known analytically in closed form [5]-[9]. Some examples of cavities which can be built up from different piecewise separable waveguide sections are illustrated in Figure 1. The high frequency asymptotic methods, e.g., GTD [1] and UTD [2,3] as well as the equivalent current method (ECM) [3,10] and also the physical theory of diffraction (PTD) [3]-[12], are employed in this hybrid formulation to find the elements of the generalized modal scattering matrices which describe the wave reflection and transmission properties of the junctions between the different waveguide sections. The asymptotic methods provide relatively simple expressions for the elements of the generalized modal scattering matrices in contrast to the more cumbersome and far less efficient numerical modal matching or integral equation techniques.

In principle, the sizes of the generalized modal scattering matrices are infinite

2

a) cavity with varying rectangular cross-section

b) cavity with circular cross-section
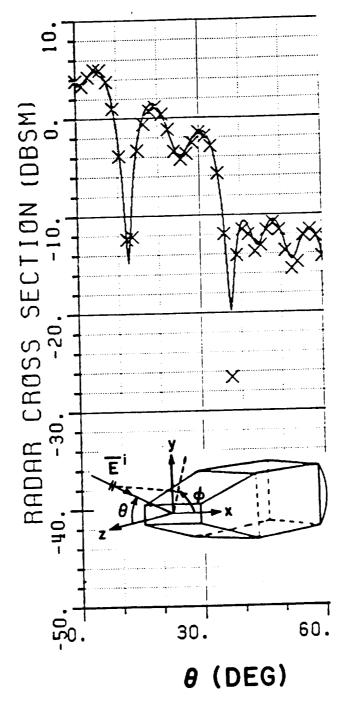
Figure 1: Examples of open-ended waveguide cavities made up of piecewise uniform waveguide sections.

as the concept of ordinary scattering matrices is generalized to include both the finite number of propagating as well as the infinite number of evanescent modes in closed waveguide regions. However, in practice, the sizes of the scattering matrices are dictated by just the number of propagating modes and a few significant evanescent modes which exist within the waveguide sections on either side of the junctions. If the waveguide sections are sufficiently long then the effects of the evanescent modes can be ignored.

Finally, the field scattered by the waveguide cavity which includes the effects of all the multiple wave interactions between the various junctions is calculated in terms of the junction scattering matrices via the self-consistent multiple scattering method, or the generalized scattering matrix technique [4]; it is assumed in this calculation that the scattering (or reflection) matrix of the interior termination can also be found.

An interesting selective modal behavior which can be inferred from the hybrid asymptotic-modal analysis is that the modes most strongly coupled into (or radiated from) the open end are those whose modal ray angles are most nearly parallel to the direction of incidence (or scattering) [6,13]. The modal ray angles alluded to in the preceding statement regarding the selective modal scheme are those associated with the modes in the first waveguide section containing the open end. This selective modal scheme, which is demonstrated in Figure 2, can be employed to increase the efficiency of computation of the field scattered from open-ended cavities, especially at high frequencies where a large number of modes can be excited.

It is noted that a perturbation of the hybrid approach can also be employed in some relatively simple cases to efficiently but approximately take into account the effect of a thin absorber coating on the interior walls of the waveguide sections

4

Figure 2: RCS pattern of a piecewise linearly tapered open-ended waveguide cavity, calculated using the hybrid asymptotic modal method, which demonstrates the selective modal scheme.

comprising the cavity [7]. On the other hand, one could also use a more rigorous procedure, but that would in general be very cumbersome both analytically and numerically.

While the hybrid asymptotic modal procedure is useful, it is primarily suitable, as mentioned previously, to treat cavities which can be built up from piecewise separable waveguide configurations for which the modes (and modal rays) can be found analytically in closed form. On the other hand, modes cannot be defined in the conventional sense for waveguide cavities with non-uniformly varying cross-sections, i.e., with walls that do not coincide with constant coordinate surfaces in a separable coordinate system. An analysis of the EM scattering by slowly varying but otherwise relatively arbitrarily shaped open-ended cavities, for which the effects of diffraction by interior walls are small, can be performed approximately via the geometrical optics (GO) ray approach used in conjunction with the aperture integration (AI) method. [14]-[22]. In this technique, the part of the incident plane wave which is intercepted by the aperture at the open end is initially divided into a sufficiently large number of parallel ray tubes which are shot into the cavity as in Figure 3. These ray tubes (or a dense grid of rays) are then tracked via all possible cavity wall reflections to the interior termination and then back to the open end. Figure 4 shows one such ray tube. Each reflection off the cavity wall is calculated via the laws of ordinary GO. The polarization, divergence, phase and magnitude of each ray tube is kept track of as it is traced through the cavity.

It is noted that the ray tubes which arrive from the termination to exit from the open end generally exist only in a discrete set of directions, and hence give rise to a discontinuous field behavior. Consequently, it is necessary to evaluate the radiation integral over the equivalent sources defined by the exiting ray tubes in the aperture to obtain a continuous value for the field that comes back out of

6
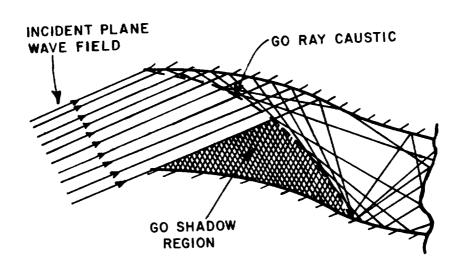
Figure 3: GO ray tubes launched into an open-ended cavity demonstrating a ray caustic and a shadow region.
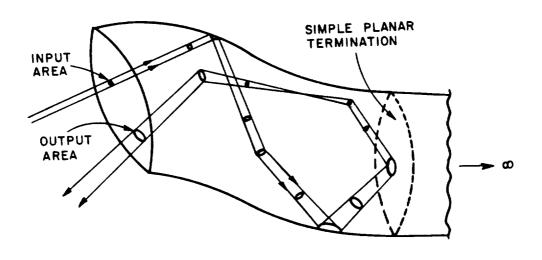
Figure 4: GO ray tube tracked inside a waveguide cavity until it exits through the open end.
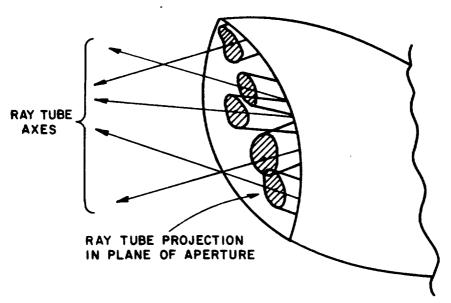
Figure 5: Projections of exiting ray tubes in the plane of the aperture of an open-ended cavity.

the cavity [7], [14]-[19]. Figure 5 demonstrates several ray tubes exiting the cavity and their projections in the plane of the aperture. This combination of GO and AI procedures may be more precisely called the GO/AI technique, rather than just the GO technique. The GO/AI technique has also been referred to as the "shooting and bouncing rays" (SBR) technique in [16]-[19].

In [16], the EM scattering by a non-uniform S-shaped, three-dimensional waveguide cavity with a planar short circuit termination is analyzed. It is noted that such a conceptually simple GO/AI or SBR approach can also include the effect of absorber coating on the interior cavity walls, or walls which are characterized by a surface impedance condition. In general, one finds that the GO/AI (SBR) based calculations usually provide the dominant trends present in the corresponding results based on the more rigorous hybrid asymptotic-modal analysis. The details of the scattered field patterns are generally not reproduced accurately at moderately high frequencies by the GO/AI (SBR) procedure; on the other hand,

this technique in general predicts the peak envelope of the RCS quite well and it tends to become increasingly more accurate at higher frequencies.

It is noted that one typically requires the density of ray tubes entering the cavity aperture to be about 350 per square wavelength (in the aperture) or more for convergence in the GO/AI (SBR) approach [16]. Thus, at high frequencies, an extremely large number of ray tubes must be allowed to enter the cavity, and each tube must be tracked through the whole length of the waveguide cavity and back via multiple wall bounces in the GO/AI (SBR) approach. Likewise, at high frequencies, an extremely large number of modes are excited which must be included in the hybrid asymptotic-modal analysis of separable (or piecewise separable) waveguide cavity configurations. Therefore, both the GO/AI (SBR), and the hybrid approaches discussed above become cumbersome and inefficient at high frequencies. Recently, a hybrid ray-mode analysis, which is more efficient than either the ray or the modal techniques used separately, has been developed in [23,24] for describing the fields coupled into large open-ended parallel plate and circular waveguides. A different approach which potentially retains the simplicity and generality of the GO approach, but which at the same time is more efficient and overcomes some of the limitations of the GO ray technique, is considered here. The latter approach, which like the GO/AI (SBR) approach is also a high frequency approach, employs spectrally narrow or well collimated Gaussian beams (GB's) to represent the fields launched from the open end into the waveguide cavity. Each Gaussian beam (GB) is then tracked axially as a ray along the beam axis. This GB approach, again like the GO/AI approach, is valid for slowly varying but otherwise relatively arbitrarily shaped open-ended waveguide cavities for which the effects of diffraction by the interior walls are small; furthermore, it can also account for the effects of absorber coating on the interior cavity walls. In previous related work, a

9

single focussed beam (e.g., a laser beam) injected into a closed parallel plate or an open dielectric waveguide of infinite extent was tracked paraxially as one GB via the complex source point method [25]; also GB's have been employed to represent the far zone radiation fields of aperture antennas in free space [26]. This aperture expansion method along with the complex source point method was applied in [27] where an array of GB's representing an aperture field was propagated in the presence of a curved dielectric layer, such as through a radome. However, the present use of GB's is somewhat different and novel in that they are employed to represent the coupling of waves through an aperture into a closed interior waveguide region when the initial excitation at the aperture is a non-Gaussian incident plane wave, and the GB's are tracked approximately like rays along their beam axes to the interior termination via successive reflections at the cavity walls; furthermore, these GB's need to be tracked only once since the expansion of the GB's in the aperture can be made independent of the incident angle thereby making this approach quite efficient. The GB expansion used here is different from the Gabor type expansion used in [26] and [27] in the respect that all the beams are identical and equally spaced in angle when initially launched. In contrast, the Gabor expansion [28,29] gives rise to GB's which have different parameters depending on the rotation of their axes, and which are not equally spaced in angle [26]. While one can employ this Gabor expansion for the aperture field here as well, the present approach is chosen as it appears to be more convenient for our particular application to interior cavity configurations by allowing more freedom to select the GB parameters suitable for axial GB tracking within the cavity. Basically, in the present GB approach, the fields in the cavity are found by first expanding the fields incident at the open end in terms of shifted and rotated GB's. In order to track beams axially and maintain sufficient resolution even after successive reflections off the interior

10

walls it is necessary to have well focussed or spectrally narrow GB's. However, such spectrally narrow GB's have wide waists. It is thus important to be able to have spectrally narrow GB's whose waists can fit easily within the waveguide cavity. Typically, the initial waists of the GB's at the aperture plane should be about half the width of the original aperture. The latter can be accomplished by dividing the aperture at the open end into equally sized sub-apertures, and then expanding the fields of each sub-aperture into a superposition of rotated GB's with equal angular spacing between each rotated beam. A procedure is then developed to determine the size of the sub-apertures and the number of GB's launched per sub-aperture, as well as the initial GB parameters.

There appear to be some important advantages to be gained by using the GB approach over the GO/AI approach for the following reasons. The GO approximation neglects the effects of rays diffracted by the aperture edges at the open end which can enter into the waveguide cavity; these effects (in addition to the effects of interior cavity wall curvature) significantly diffuse the initially collimated GO incident field as it propagates large distances into the cavity. Furthermore, the GO field description fails at and near ray caustics; such ray caustics can occur if the GO rays undergo reflections from portions of the interior cavity walls which are concave (see Figures 3 and 4) or exhibit points of inflection. On the other hand, the field of the GB's launched from the aperture into the interior waveguide cavity region as in Figure 6 includes the contribution of the aperture edge diffracted fields which enter the cavity, and the GB description remains valid at ray caustics. It also appears that one needs to launch less than 25 GB's per square wavelength in the aperture to accurately represent the interior fields over a sufficient distance within the slowly varying waveguide cavity provided the aperture is large enough to launch well collimated GB's inside the cavity. As mentioned above, another

Pth SUBAPERTURE

TYPICAL BEAM FIELD

INCIDENT WAVE

BEAM AXES
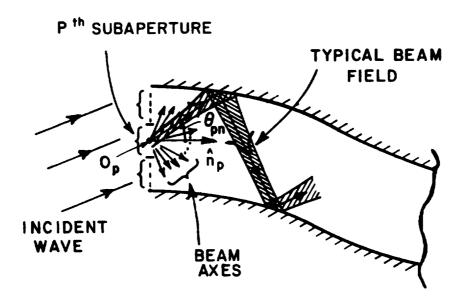
Figure 6: Example of one typical Gaussian beam launched into an open-ended cavity from the pth sub-aperture.

significant advantage of the GB's which is not present in the GO/AI approach is that if the density of the GB's is appropriately increased to about 100 per square wavelength in the aperture, then the GB's become independent of the incident angle over a sufficiently large range of angles, and therefore need to be tracked only once within the interior. In contrast, the GO rays need to be tracked each time the incident angle is changed. This advantage of the GB's comes from the fact that they can be launched as a phase-space like array which is sufficiently dense to cover the entire angular range of interest. Thus, if the expansion in terms of GB's is selected to be independent of the incident angle, then only the initial GB amplitudes change with the incident angle. Moreover, this suggests that not all GB amplitudes are significant so that one can even pre-select the most strongly excited GB's, just as in the selective modal scheme mentioned earlier [13], to once again further reduce the computational times. On the other hand, one finds that the axial (real ray) tracking of the GB's requires one to launch well focussed GB's

12

5 SUB-APERTURES

INCIDENT WAVE
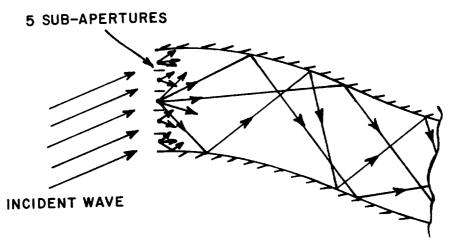
Figure 7: Rays launched from sub-apertures into a cavity using the GRE method.

whose spatially wide waists must fit well within the waveguide cavity. The spatially wide GB's sample a wide portion of the reflecting cavity walls and undergo distortion at each reflection thus limiting their use to waveguide cavities which are not long relative to their width.

An alternative ray method for analyzing the scattering by open-ended waveguide cavities which will be referred to as the generalized ray expansion (GRE) method, is also developed here to avoid the problems of beam distortion due to successive reflections in the axial GB tracking approach. In the GRE, the rays are launched into the cavity from each sub-aperture as in Figure 7; this is done in a manner which is very similar to the launching of the GB's from the sub-apertures as shown earlier in Figure 6, but is different from that in the GO/AI or SBR approach shown in Figure 3. Thus, the rays launched in the GRE method implicitly contain effects of waves diffracted into the cavity via the edges at the open end as in the GB approach; also, each of the many rays launched from the sub-apertures needs to be tracked only once independent of the incident angle, again as in the GB

method. The GO ray tubes in the GRE can be made as narrow as is necessary, unlike the GB's, so that they can be traced (via the laws of GO) much farther inside the waveguide cavity than the GB's. This allows the GRE method to be applicable to cavity configurations of virtually unlimited depth and generality. The limitation of the GRE method is that it uses the laws of GO to trace the ray tubes within the cavity so errors can accumulate from the effects of ray caustics, creeping waves and surface diffraction. Also, the GRE method like the GB and GO/AI (or SBR) also does not include diffraction from interior discontinuities, such as from the junctions between waveguide sections in the cavities of Figure 1, for example. However, realistic cavity configurations have smooth, slowly varying walls so the higher order diffraction effects are minimal and can be neglected.

In general, the termination within the cavity can be quite complex. It is therefore convenient to characterize the termination in terms of a scattering matrix which can be found separately via the method of moments (MM), or via some approximation scheme (e.g., physical optics (PO) if appropriate), or by measurements, etc. This scattering matrix provides the fields scattered by the termination over some fictitious aperture plane in the neighborhood of the termination, when a given field distribution is incident on this plane, but in the absence of the termination, after propagating into the cavity from the open end where it originates due to the plane wave illumination. If the waveguide cavity region containing the termination and its vicinity is separable, as it is assumed here, then the termination scattering matrix can be expressed in terms of the modes of that region. This termination scattering information obtained separately from an analysis dictated by only the shape of the waveguide cavity region containing the termination and its vicinity, and by the termination itself, can be combined effectively via a generalized reciprocity principle with the information on the fields propagating from

14

the open end into the waveguide cavity region (without the termination) obtained by any appropriate approach (e.g., the hybrid modal, GO/AI (or SBR), GB or GRE methods, etc.). This generalized reciprocity integral involves a reaction of these two separate fields over the conveniently chosen fictitious plane near the termination. Such a generalized reciprocity (or reaction) integral formulation thus allows one to systematically and independently study the effects of various terminations and waveguide cavity shapes, respectively, on the overall scattering by such open-ended waveguide cavities with complex terminations. It is noted once again that the use of this generalized reciprocity result requires one to track the fields from the open end to the fictitious termination plane and not back again to the open end [30]; thereby further adding to the computational efficiency. This method, referred to as the reciprocity integral (RI) method, is described in detail in Appendix C.

The format of this report is as follows. The hybrid asymptotic-modal analysis will be described in Chapter II, the GO/AI (SBR) method in Chapter III, the GB method in Chapter IV and the GRE method in Chapter V. Numerical results based on each of the methods will be included at the end of Chapters II through V, respectively, and conclusions will be discussed in Chapter VI. Appendices A thru D will describe the waveguide modes of 2-D parallel-plate and annular waveguides, the aperture integration of GO ray-tubes, the reciprocity integral method, and the sub-aperture expansion method in 2-D, respectively. The aspects of incidence and scattering of interest in the present work are restricted primarily to the sector $0° < \theta, \theta_i < 60°$ where the incident and scattering directions θ_i and θ, respectively, are with respect to the axis of the waveguide cavity at the open end. Furthermore, as mentioned earlier, the scattering from all external features except by the edges at the open end of the cavities will be excluded in this report. Only the scattering

15

by the edges at the open end and by the interior cavity termination are of main concern here. Finally, an $e^{j\omega t}$ time dependence for the EM fields will be assumed and suppressed in the analyses to follow.

CHAPTER II

THE HYBRID ASYMPTOTIC MODAL METHOD

In the hybrid asymptotic modal method (henceforth referred to as simply the hybrid modal method) for analyzing the EM scattering of an incident plane wave by an open-ended waveguide cavity, sections of uniform waveguides are joined together to build up a more general cavity configuration. The fields within these uniform waveguide configurations are separable; i.e., the modes and the associated modal rays for the waveguide sections can be described analytically in closed form [5,6,7]. Some typical open cavities which can be built up in this manner are shown in Figure 1. The multiple wave interactions between the junctions formed by connecting the different waveguide sections, the open end and the termination, respectively, are handled using a self-consistent multiple scattering matrix (MSM) method, sometimes referred to as the generalized scattering matrix method. In this method the scattering by isolated scattering centers (e.g., the open end, junctions and the termination) is represented in terms of transmission and reflection matrices which the MSM ties together self-consistently to include all possible interactions between the scattering centers.

Because realistic cavity geometries can be large in terms of wavelength, there are typically many propagating waveguide modes which can be supported within the cavity (the number increases exponentially with the cross-sectional area). This makes it very inefficient to find the elements of the individual scattering matrices

17

using numerical methods such as mode matching or integral equation methods. However, these large waveguide structures do lend themselves well to high frequency asymptotic methods. The hybrid approach to the modal method finds the elements of the individual scattering matrices directly and efficiently using high frequency asymptotic methods such as GTD [1], ECM [3,10] and PTD [3,11,12].

As implied earlier, the hybrid modal method is limited to cavities that can be "built up" from joining sections of uniform waveguides for which the modal fields are known. Also, these waveguide sections are most often perfectly conducting because cumbersome numerical procedures are usually required to solve the complex eigenfunction equations for the modes of waveguides whose walls are non-perfectly conducting [16]. It is possible to use perturbation techniques as in [7] where it is assumed that the walls can be modeled by impedance surfaces which are nearly perfectly conducting, but this unfortunately has limited practicality. Finally, because the number of modes which must be included increases exponentially with frequency, even the hybrid modal method becomes cumbersome and inefficient for larger perfectly conducting cavities. The main advantage of using this hybrid modal method, aside from being efficient compared with numerical methods, is that it can give highly accurate results when applied properly. This allows the method to be very useful in verifying more approximate methods that can handle general cavity geometries and surface characteristics, such as the methods described in the next three chapters. Often there is no other reasonable means of verification other than direct measurement.

In this chapter, the MSM will be formulated in terms of the individual scattering matrices of the open end and termination of a simple open-ended cavity made up of a single waveguide section. It will be discussed how a simple extension of the MSM of the single section cavity can be applied to cavities made up of mul-
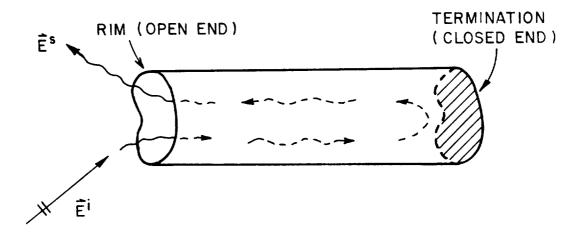
Figure 8: Open-ended waveguide cavity made up of a single waveguide section illuminated by a plane wave.

tiple waveguide sections, such as in Figure 1. High frequency asymptotic methods will then be used to find the elements of the individual scattering matrices in an efficient way. Finally, some numerical results from [5]-[9] will be presented.

2.1 Self-Consistent Multiple Scattering Matrix Formulation

2.1.1 Formulation for a cavity with a single waveguide section.

The MSM will be derived in this section to describe the scattering by an open-ended waveguide cavity made up of a single terminated waveguide section illuminated by an incident EM plane wave in free space, as shown in Figure 8. The electric and magnetic fields $\vec{E}^i$ and $\vec{H}^i$, respectively, of this plane wave can be written as

$$\vec{E}^i = \left(\hat{\theta}^i A_\theta^i + \hat{\phi}^i A_\phi^i \right) e^{-j\vec{k}^i \cdot \vec{r}} \tag{2.1}$$

$$\vec{H}^i = Z_o^{-1} \hat{k}^i \times \vec{E}^i, \tag{2.2}$$

19

where

$$\vec{k}^i = k\hat{k}^i \qquad (2.3)$$

$$\hat{\phi}^i = \hat{k}^i \times \hat{\theta}^i \qquad (2.4)$$

$$k = \text{free space wavenumber } (2\pi/\lambda),$$

$$\hat{k}^i = \text{direction of the incident plane wave},$$

$$Z_o = \text{plane wave impedance in free space.}$$

In terms of the incidence angles,

$$\hat{k}^i = -\hat{x}\sin\theta^i\cos\phi^i - \hat{y}\sin\theta^i\sin\phi^i - \hat{z}\cos\theta^i \qquad (2.5)$$

where

$$\theta^i, \phi^i = \text{elevation and azimuth angles of incident plane wave.}$$

The scattered field due to this plane wave incident field can be written as a sum of its rectangular vector components as

$$\vec{E}^s = \hat{x}E_x^s + \hat{y}E_y^s + \hat{z}E_z^s. \qquad (2.6)$$

The multiple scattering matrix $[S]$ for this problem relates the scattered field components of (2.6) to the incident field components of (2.1) and is defined by

$$\begin{bmatrix} E_x^s \\ E_y^s \\ E_z^s \end{bmatrix} = [S] \begin{bmatrix} A_\theta^i \\ A_\phi^i \end{bmatrix}. \qquad (2.7)$$

It is clear from (2.7) that $[S]$ has three rows and two columns (i.e., it is of order 3×2).

20

Referring again to Figure 8, the total forward or backward ($\pm \hat{\eta}$) propagating fields inside the waveguide section, which include all the effects of multiple interactions between the open end and the termination, can be written as a sum of waveguide modes:

$$\left(\vec{E}_w^{\pm}, \vec{H}_w^{\pm} \right) \;=\; \sum_{n=1}^{N} A_n^{\pm} \left(\hat{e}_n^{\pm}, \hat{h}_n^{\pm} \right) e^{\mp j\beta_n \eta} \qquad (2.8)$$

where

$$
\begin{aligned}
\hat{e}_n^{\pm}, \hat{h}_n^{\pm} \;&=\; n^{th} \text{ waveguide modal fields,} \\
\beta_n \;&=\; \text{propagation constant of the } n^{th} \text{ mode,} \\
\eta \;&=\; \text{axial coordinate of the waveguide,} \\
A_n^{\pm} \;&=\; \text{modal expansion coefficients,} \\
N \;&=\; \text{number of included modes.}
\end{aligned}
$$

These waveguide modal fields are complete orthogonal eigenfunction solutions to the vector wave equation, with appropriate boundary conditions, for a separable waveguide geometry of infinite length. The open-ended cavities of this analysis are made up of finite length sections of these waveguides. The exact closed-form expressions for the modal fields of some simple waveguide geometries and the method of derivation can be found in [31]. The expressions for the modal fields of a two-dimensional (2-D) parallel-plate waveguide and a 2-D annular (curved) waveguide are derived in Appendix A of this report as examples.

It is noted that a waveguide supports a finite number of propagating modes and an infinite number of evanescent modes; so if all the modes are included, N is infinite. However, because the evanescent modes die out very quickly as they propagate down the waveguide (β_n is pure imaginary for evanescent modes) and the higher the mode number the faster they decay, the summation of (2.8) is

truncated at some value N which includes all the propagating modes and only the few significant evanescent modes. Usually, the effect of evanescent modes is so small that they can be neglected completely. This occurs for waveguide sections which have a large number of propagating modes or are long enough for the lowest order evanescent modes to decay to a sufficiently low level. The sizes of the waveguides of interest to this study are usually large enough so that the evanescent modes can be neglected.

The components of the field scattered by the cavity, including only the scattering by the interior of the cavity and the rim at the open end, can be written as

$$
\begin{bmatrix} E_x^s \\ E_y^s \\ E_z^s \end{bmatrix} = [S_{11}] \begin{bmatrix} A_\theta^i \\ A_\phi^i \end{bmatrix} + [S_{12}][A^+]
\tag{2.9}
$$

where $[S_{11}]$ is the scattering matrix which relates the incident field components to the components of the field scattered by the edges or the rim at the open end of the cavity and is of order 3×2. $[A^+]$ is a column matrix of order N containing the coefficients A_n^+ of the $+\hat{\eta}$ propagating modes incident on the open end from within the cavity, and $[S_{12}]$ is the transmission type scattering matrix of order $3 \times N$ which relates these modal coefficients to the components of the field scattered by the interior of the waveguide cavity. These two scattering matrices are illustrated in Figure 9. η is an arbitrary axial coordinate for the waveguide under consideration and is shown in Figure 16.

The $+\hat{\eta}$ propagating modal fields incident on the open end from within the waveguide with coefficients A_n^+ are due to $-\hat{\eta}$ propagating modal fields with coefficients A_n^- which have reflected from the termination of the cavity. Therefore, $[A^+]$ can be related to $[A^-]$ via a termination modal reflection matrix denoted by $[S_{\Gamma}]$,

22
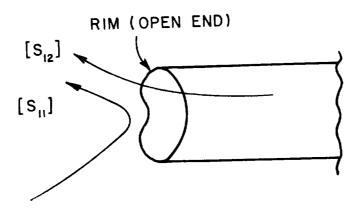
Figure 9: Open end of a waveguide cavity illustrating the scattering matrices $[S_{11}]$ and $[S_{12}]$.

with appropriate phase delays which account for the modal propagation down and back the length of the waveguide section:

$$[A^+] = [P][S_\Gamma][P][A^-]. \tag{2.10}$$

$[P]$ is a diagonal matrix of order $N \times N$ which describes the phase translation of a modal field down the length of the waveguide and is given by

$$[P] = \begin{bmatrix} \ddots & 0 & 0 \\ 0 & e^{-j\beta_n l} & 0 \\ 0 & 0 & \ddots \end{bmatrix} \tag{2.11}$$

where

$$l = \text{length of the waveguide section.}$$

$[S_\Gamma]$ is a reflection type scattering matrix of order $N \times N$ which relates coefficients of the $-\hat{\eta}$ propagating modal fields incident on the termination to coefficients of the $+\hat{\eta}$ propagating reflected modal fields. $[P]$ and $[S_\Gamma]$ are illustrated in Figure 10.

23

TERMINATION
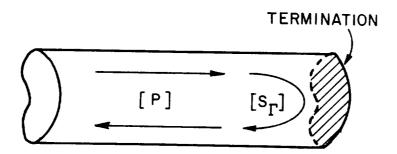
Figure 10: Open-ended waveguide cavity illustrating the matrices $[P]$ and $[S_\Gamma]$.

The $-\hat{\eta}$ propagating modal coefficients A_n^- can found in terms of the coupling of the incident plane wave into waveguide modes in addition to the reflection of modes incident on the open end from within the cavity. This is expressed as

$$[A^-] = [S_{21}] \begin{bmatrix} A_\theta^i \\ \\ A_\phi^i \end{bmatrix} + [S_{22}][A^+] \qquad (2.12)$$

where $[S_{21}]$ is the transmission type scattering matrix of order $N \times 2$ which relates the components of the incident plane wave to the coefficients of the $-\hat{\eta}$ propagating modes, and $[S_{22}]$ is the reflection type scattering matrix of order $N \times N$ which relates the coefficients of the $+\hat{\eta}$ propagating modes incident on the open end from within the cavity to the coefficients of the $-\hat{\eta}$ propagating modes. $[S_{21}]$ and $[S_{22}]$ are illustrated in Figure 11.

Equations (2.10) and (2.12) can be solved for $[A^+]$ which can then be substituted into (2.9) to give the components of the scattered field in terms of the components of the incident plane wave; the complete scattering matrix $[S]$ of (2.7)

24
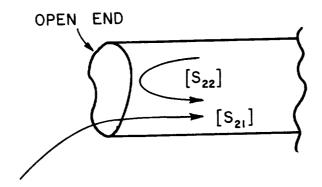
Figure 11: Open end of a waveguide cavity illustrating the scattering matrices $[S_{21}]$ and $[S_{22}]$.

will then be evident. Combining (2.10) and (2.12) yields

$$([I] - [S_{22}][P][S_\Gamma][P]) [A^-] = [S_{21}] \begin{bmatrix} A_\theta^i \\ \\ A_\phi^i \end{bmatrix} \qquad (2.13)$$

where

$$[I] = \text{identity matrix of order } N \times N.$$

Using (2.13) in (2.10) gives

$$[A^+] = [P][S_\Gamma][P] ([I] - [S_{22}][P][S_\Gamma][P])^{-1} [S_{21}] \begin{bmatrix} A_\theta^i \\ \\ A_\phi^i \end{bmatrix} \qquad (2.14)$$

and substituting this into (2.9) yields

$$\begin{bmatrix} E_x^s \\ \\ E_y^s \\ \\ E_z^s \end{bmatrix} = \left\{ [S_{11} + [S_{12}][P][S_\Gamma][P] ([I] - [S_{22}][P][S_\Gamma][P])^{-1} [S_{21}] \right\} \begin{bmatrix} A_\theta^i \\ \\ A_\phi^i \end{bmatrix} .$$

$$(2.15)$$

From (2.15) the complete MSM for the open-ended waveguide cavity of Figure 8 can be extracted as

$$[S] = [S_{11}] + [S_{12}][P][S_\Gamma][P]\left([I] - [S_{22}][P][S_\Gamma][P]\right)^{-1}[S_{21}].$$

(2.16)

Notice that this matrix is composed of two terms — the scattering matrix of the rim at the open end and a product of scattering matrices which together give the scattering matrix of the interior of the cavity. Also notice that if the multiple interactions between the open end and the termination can be neglected, i.e., if the elements of $[S_{22}]$ are assumed to be zero, then the inverted term of (2.16) disappears and the scattering matrix is approximated by

$$[S] \approx [S_{11}] + [S_{12}][P][S_\Gamma][P][S_{21}].$$

(2.17)

This can be interpreted physically as follows: reading from right to left, the matrix $[S_{21}]$ couples the components of the incident plane wave field into waveguide modes. $[P]$ propagates the modes down the guide to the termination where they are reflected via $[S_\Gamma]$. They are then propagated again by $[P]$ back to the open end where they are coupled to the components of the scattered field in the exterior region via $[S_{12}]$. The scattering by the rim at the open end is then added using $[S_{11}]$ to give the total field scattered by the open-ended cavity. Equation (2.17) is often used because the modal reflection by the open end ($[S_{22}]$) is usually negligible compared with the reflection by the termination ($[S_\Gamma]$). This eliminates the need to invert a rather large matrix of order $N \times N$, as in (2.16).

2.1.2 Extension to cavities made up of more than one waveguide section.

Figure 12 shows an open-ended cavity made up of two waveguide sections with a termination. The MSM can be easily extended to this cavity by simply

26
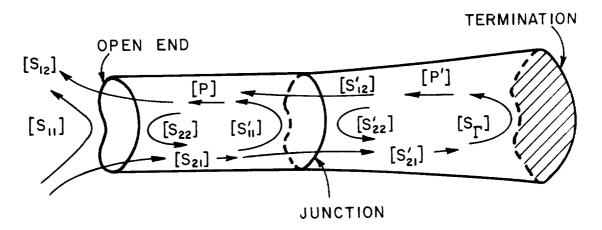
Figure 12: Open-ended cavity made up of two waveguide sections with a termination.

replacing $[S_\Gamma]$ in (2.16) of the single section case above, with an effective MSM which describes the multiple interactions between the termination and the junction between the two waveguide sections. This new reflection matrix is given by

$$[S_\Gamma] = [S_{11}'] + [S_{12}'][P'][S_\Gamma'][P'] \left([I'] - [S_{22}'][P'][S_\Gamma'][P'] \right)^{-1} [S_{21}'].$$

(2.18)

This is exactly analogous to (2.16) (and can be derived the same way) except that the scattering matrices of the junction between the sections, $[S_{11}']$, $[S_{12}']$ and $[S_{21}']$, now relate the coefficients of the modal fields on either side of the junction rather than relating the modal coefficients with the components of the incident and scattered fields of the exterior region, as is done for the open end. Figure 12 illustrates the individual scattering matrices associated with the two-section cavity.

In general, the two waveguide sections will have sets of waveguide modes differing in structure and number. Referring to Figure 12, let there be M included modes in the second section (the waveguide to the right) and once again there are

N included modes in the first section (the waveguide to the left). Then the transmission type scattering matrix $[S'_{21}]$ is of order $M \times N$ and relates the coefficients of the modal field incident on the junction from the first section to the coefficients of the modal fields coupled into the second section and $[S'_{12}]$, which is of order $N \times M$, does the reverse. $[S'_{11}]$ is of order $N \times N$ and relates the coefficients of the modal field incident on the junction from the first section to the coefficients of the modal fields reflected by the junction (note that this does not include the scattering by anything beyond the junction, which is accounted for using (2.18)). Likewise, $[S'_{22}]$ is of order $M \times M$ and relates the coefficients of the modal field incident on the junction from the second section to the coefficients of the field reflected by the junction. The new termination modal reflection matrix $[S'_{\Gamma}]$, the propagation matrix of the second section $[P']$ and the identity matrix $[I']$ in (2.18) are all of order $M \times M$.

The junction reflection type scattering matrices $[S'_{11}]$ and $[S'_{22}]$ are often negligible compared with the termination scattering matrix $[S_{\Gamma}]$ so they can be excluded, like $[S_{22}]$ was excluded in the last section. After removing these three matrices, the total self-consistent scattering matrix of the two-section open-ended cavity can be approximated similar to (2.17) as

$$[S] \approx [S_{11}] + [S_{12}][P][S'_{12}][P'][S'_{\Gamma}][P'][S'_{21}][P][S_{21}] \tag{2.19}$$

which can be physically interpreted the same way as (2.17) was in the last section.

It should now be clear that another waveguide section could be added by simply replacing $[S'_{\Gamma}]$ with the effective MSM of this additional section, exactly the same way as was done for the second section. This process could be repeated indefinitely to handle cavities made up of any number of waveguide sections. However, if all the multiple interactions are to be included, i.e., the junction reflection

matrices are not neglected, the number of necessary matrix inversions increases exponentially, making the method more and more inefficient. Therefore, it is desirable to exclude the junction reflection matrices whenever possible. Luckily, for the larger cavity geometries with smooth junctions encountered in practice, the approximation is quite adequate. For smaller waveguide cavities, the effects of the junction reflection matrices may become more important so it is suggested that they be included if the number of waveguide modes is not too large to be a limitation.

2.2 Development of the Elements of the Scattering Matrices in the Multiple Scattering Matrix (MSM) Method

In this section the individual scattering matrices associated with the open end, junctions and termination will be found using high-frequency asymptotic methods. In particular, the methods used are GTD, UTD, ECM and PTD [1]-[3], [10]-[12]. The equations presented here are for the general case; more explicit expressions for selected waveguide geometries can be found in [5]-[9].

2.2.1 The scattering matrix of the rim at the open end $[S_{11}]$.

$[S_{11}]$, the scattering matrix which relates the components of the plane wave incident on the open end to the components of the fields scattered by the rim is defined by

$$
\begin{bmatrix} E_x^{sr} \\ E_y^{sr} \\ E_z^{sr} \end{bmatrix} = [S_{11}] \begin{bmatrix} A_\theta^i \\ A_\phi^i \end{bmatrix} \tag{2.20}
$$

where

$$E_x^{sr}, E_y^{sr}, E_z^{sr} = \text{rectangular components of the electric field scattered by}$$

29
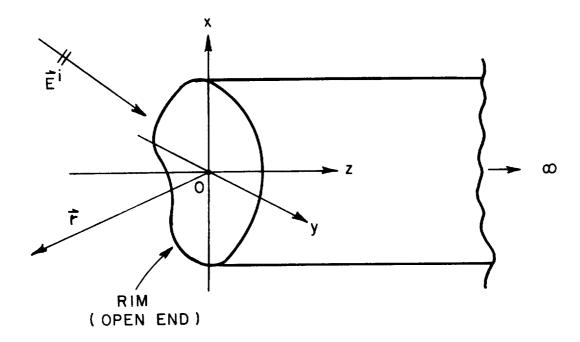
Figure 13: Geometry for finding the scattering matrix $[S_{11}]$.

the rim,

A_θ^i, A_ϕ^i = components of the electric field of the plane wave

incident on the open end.

It is clear from (2.20) that $[S_{11}]$ is of order 3×2 (i.e., it has two rows and three columns), as mentioned earlier. The geometry for finding this scattering matrix is a semi-infinite open-ended waveguide, as shown in Figure 13.

Using the equivalent current method (ECM) the scattered field is assumed to be produced by equivalent electric and magnetic currents that replace the rim and radiate in free space. The scattered field can then be written as an integral over these currents and is given by

$$\vec{E}^{sr} = \frac{jkZ_o}{4\pi} \int_{rim} \left[\hat{R} \times \hat{R} \times \vec{I}_{eq}(l') + Y_o \hat{R} \times \vec{M}_{eq}(l') \right] \frac{e^{-jkR}}{R} dl' \quad (2.21)$$

30

x

$\hat{k}^i$

$\overline{I}_{eq}$

$\overline{M}_{eq}$

z

$\overline{r}$

O

$\overline{r}'$

P

$\overline{R}$

$d\vec{\ell}'=\hat{\ell}'d\ell'$

y

RIM (OPEN END)
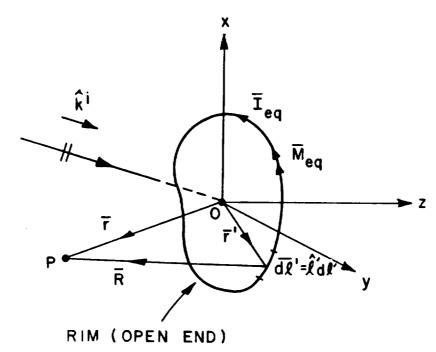
Figure 14: Equivalent currents which replace the rim at the open end of the
waveguide.

where

$$\vec{R} \;=\; \text{vector from a point on the rim to the receiver position,}$$

$$Y_o \;=\; \text{free space admittance } (= Z_o^{-1}),$$

$$l' \;=\; \text{coordinate of points on the rim.}$$

The geometry is shown in Figure 14.

The equivalent currents $\vec{I}_{eq}$ and $\vec{M}_{eq}$ are excited by the incident plane and are given by [3]

$$\vec{I}_{eq}(l') \;=\; -\frac{\hat{l}' \cdot \vec{E}^i(rim)}{Z_o\sqrt{\sin\beta_o \sin\beta}} D_s(\psi,\psi';\beta_o,\beta,\alpha)\sqrt{\frac{8\pi}{jk}}\hat{l}' \qquad (2.22)$$

$$\vec{M}_{eq}(l') \;=\; -\frac{\hat{l}' \cdot \vec{H}^i(rim)}{Y_o\sqrt{\sin\beta_o \sin\beta}} D_h(\psi,\psi';\beta_o,\beta,\alpha)\sqrt{\frac{8\pi}{jk}}\hat{l}' \qquad (2.23)$$

where D_s and D_h are the soft and hard GTD diffraction coefficients, respectively,

31

$$\beta = \beta_o \text{ ON KELLER CONE}$$
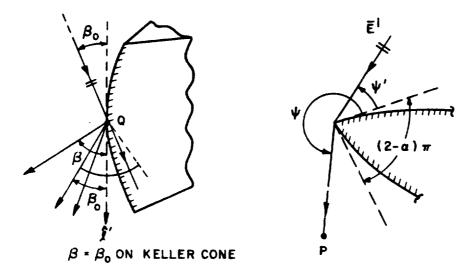
Figure 15: Geometry of the wedge diffraction coefficient showing the angles β_o, β, ψ, ψ' and α.

given by [1]

$$D_{s,h}(\psi,\psi';\beta_o,\beta,\alpha) = \frac{e^{-j\frac{\pi}{4}}\sin\frac{\pi}{\alpha}}{\alpha\sqrt{2\pi k}\sqrt{\sin\beta_o\sin\beta}}$$
$$\cdot \left[\frac{1}{\cos\frac{\pi}{\alpha} - \cos\frac{\psi-\psi'}{\alpha}} \mp \frac{1}{\cos\frac{\pi}{\alpha} - \cos\frac{\psi+\psi'}{\alpha}} \right] \quad (2.24)$$

with the angles defined in Figure 15. By substituting (2.24) into (2.22) and (2.23) and then (2.23) and (2.24) into (2.21) and integrating, one obtains the field scattered by the rim at the open end in terms of the incident plane wave. From this result, the elements of $[S_{11}]$ can then be easily identified and extracted.

It is noted that the GTD diffraction coefficients of (2.24) are non-uniform and therefore become singular at the shadow boundaries formed by the incident and reflected ray-optical fields and the wedge. However, this usually only occurs for cases where the incident plane wave comes close to grazing the aperture; nevertheless, this range of angles is not of interest as indicated previously. Furthermore, if the incident plane wave grazes the aperture, very little energy will be coupled into the waveguide cavity; also the specular contribution from the external surface

32
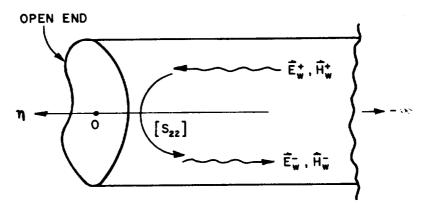
Figure 16: Reflection of modal fields from the open end of a semi-infinite open-ended waveguide.

of the cavity near the aperture can become important for this case and could be accounted for via the UTD [2,3].

2.2.2 The reflection modal scattering matrices of the open end $[S_{22}]$ and junctions $[S'_{11}]$, $[S'_{22}]$.

Figure 16 shows the geometry used for finding $[S_{22}]$, the reflection type scattering matrix which relates the coefficients of the modal field incident on the open end from within a semi-infinite open-ended waveguide to the coefficients of the reflected modal field. Let these incident or reflected waveguide modal fields be written as a sum of $+\hat{\eta}$ and $-\hat{\eta}$ propagating modes similarly to (2.8) as

$$\left(\vec{E}_w^{\pm}, \vec{H}_w^{\pm}\right) = \sum_{n=1}^{N} C_n^{\pm} \left(\hat{e}_n^{\pm}, \hat{h}_n^{\pm}\right) e^{\mp j\beta_n \eta}. \tag{2.25}$$

$[S_{22}]$ is then defined by

$$[C^-] = [S_{22}][C^+] \tag{2.26}$$

and is of order $N \times N$, as mentioned earlier.

The ECM will again be used to find the elements of $[S_{22}]$ by replacing the open end with equivalent magnetic line and dipole currents which coincide with the rim

33

EQUIVALENT CURRENTS
REPLACING OPEN END
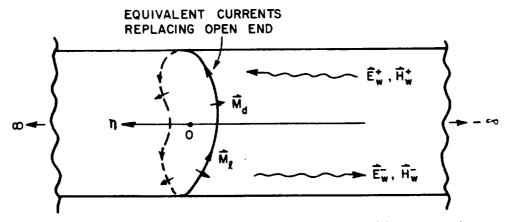
Figure 17: Equivalent problem with the open end replaced by magnetic current sources radiating on the walls of an infinite waveguide.

at the open end. These currents are then allowed to radiate on the walls inside the waveguide which now extends to infinity in both directions as illustrated in Figure 17. It is noted that electric currents are not used here because they would not radiate on the surface of the perfectly conducting waveguide walls. Also note that this is not the same case as in the last section where the equivalent currents were allowed to radiate in free space.

The radiating magnetic currents will excite modes inside the waveguide propagating in both directions away from the current sources. The excitation of waveguide modes can be found for any given current source distribution using the equation found in [31]:

$$C_n^{\pm} = -\frac{1}{2 \int \int_S \hat{e}_{nt} \times \hat{h}_{nt} \cdot \hat{\eta} dS} \int \int \int_V \left(\hat{e}_n^{\mp} \cdot \vec{J} - \hat{h}_n^{\mp} \cdot \vec{M} \right) e^{-j\beta_n \eta} dV.$$

$$(2.27)$$

The integration in (2.27) is over the volume containing the current sources. The waveguide modal fields have been decomposed into their transverse and axial com-

34

ponents in (2.27) and can be written as

$$\hat{e}_n^{\pm} = \hat{e}_{nt} \pm \hat{e}_{n\eta} \tag{2.28}$$

$$\hat{h}_n^{\pm} = \pm\hat{h}_{nt} + \hat{h}_{n\eta} \tag{2.29}$$

where

$\hat{e}_{nt}, \hat{h}_{nt}$ = transverse components of the electric and magnetic fields, respectively, of the nth waveguide mode,

$\hat{e}_{n\eta}, \hat{h}_{n\eta}$ = axial ($\hat{\eta}$) components of the electric and magnetic fields, respectively, of the nth waveguide mode.

$\int\int_S \hat{e}_{nt} \times \hat{h}_{nt} \cdot \hat{\eta} dS$ is a term which normalizes the power of the nth mode and S is an arbitrary cross-section inside the waveguide. To find the coefficients of the modes reflected by the open end, the volume integral in (2.27) reduces to a line integral and the coefficients are given by (setting $\eta = 0$ at the open end)

$$C_n^- = \frac{1}{2\int\int_S \hat{e}_{nt} \times \hat{h}_{nt} \cdot \hat{\eta} dS} \int_{rim} \hat{h}_n^+ \cdot \left[\vec{M}_l(l') + \vec{M}_d(l')\right] dl' \tag{2.30}$$

where

$\vec{M}_l(l'), \vec{M}_d(l')$ = equivalent magnetic line and dipole sources, respectively, replacing the rim at the open end

l' = coordinate of points along the rim.

The mn^{th} element of the $[S_{22}]$ is simply the coefficient of the nth reflected mode due to a single m^{th} mode incident on the open end of the waveguide and can be written using (2.30) as

$$[S_{22}]_{mn} = \frac{1}{2\int\int_S \hat{e}_{nt} \times \hat{h}_{nt} \cdot \hat{\eta} dS} \int_{rim} \hat{h}_n^+ \cdot \left[\vec{M}_{lm}(l') + \vec{M}_{dm}(l')\right] dl'$$

$$\tag{2.31}$$

35
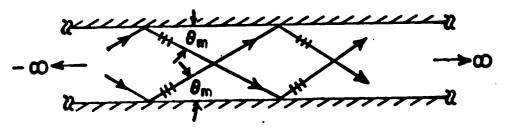
Figure 18: Ray-optical fields of the mth mode in a parallel-plate waveguide.

where

$$\vec{M}_{lm}(l'), \vec{M}_{dm}(l') \quad = \quad \text{equivalent magnetic line and dipole sources,}$$

respectively, due to the mth mode incident on the

open end.

So far we have the elements of $[S_{22}]$ given in terms of the equivalent magnetic current sources due to the mth incident mode, as in (2.31). To find the elements of $[S_{22}]$, we must know the excitation of these sources by an incident waveguide mode. This is done by decomposing the modal field into its high-frequency ray-optical equivalent. For example, the modal fields of a 2-D parallel-plate waveguide are expressed in terms of sine and cosine functions. When these are written in their exponential (Euler) form, it becomes clear that the modes in a parallel-plate waveguide are simply crossing plane waves which propagate at a characteristic mode angle θ_m, as shown in Figure 18. The modal fields and their ray-optical equivalents are derived for the parallel-plate and 2-D annular waveguides in Appendix A.

In general, it is found that in the vicinity of a waveguide wall, a modal field can be expressed as a sum of ray-optical fields which propagate toward and away

36

from the wall. For a point near a wall, this is written for the mth mode as

$$\left(\hat{e}_m^{\pm}, \hat{h}_m^{\pm}\right) e^{\mp j\beta_n \eta} \;=\; \sum_{p=1}^{P_m} \left[\left(\hat{e}_{mp,i}^{\pm}, \hat{h}_{mp,i}^{\pm}\right) + \left(\hat{e}_{mp,r}^{\pm}, \hat{h}_{mp,r}^{\pm}\right)\right] \qquad (2.32)$$

where

$$\left(\hat{e}_{mp,i}^{\pm}, \hat{h}_{mp,i}^{\pm}\right) \;=\; p^{th} \text{ ray-optical fields of the } m^{th} \text{ mode propagating towards}$$

the waveguide wall,

$$\left(\hat{e}_{mp,r}^{\pm}, \hat{h}_{mp,r}^{\pm}\right) \;=\; p^{th} \text{ ray-optical fields of the } m^{th} \text{ mode propagating away}$$

from the waveguide wall,

$$P_m \;=\; \text{number of ray-optical fields of the } m^{th} \text{ mode.}$$

These ray-optical fields can now be used to find the excitation of the equivalent magnetic current sources of the ECM, again using the Keller-type GTD wedge diffraction coefficient of (2.24). The only difference is that for this case the incident field is the ray-optical form of the incident modal field instead of a plane wave, and the equivalent currents radiate on the inner surface of a waveguide wall instead of in free space, as was done in Section 2.3.1. Physically, the ray-optical fields of the waveguide mode are incident on the rim at the open end and diffract, radiating energy into the exterior region and also back into the waveguide region. This scattered field is represented as being produced by equivalent magnetic line and dipole currents along the rim. The exterior region is not of interest in finding $[S_{22}]$, so the original semi-infinite geometry is replaced in this equivalence by an extension of the waveguide past the open end to infinity, and the equivalent magnetic currents located where the rim was in the original configuration now radiate inside, exciting waveguide modes in both directions, via (2.30) for this case.

The equivalent magnetic current sources of (2.31) due to the mth incident

37

mode and which are used to excite the nth reflected mode are given by [5]

$$\vec{M}_{lm}(l') = -\hat{l}' \sum_{p=1}^{P_m} \frac{1}{Y_o} \sqrt{\frac{8\pi}{jk}} \left(\hat{h}_{mp,i}^+ \cdot \hat{l}'\right) \frac{D_h(\psi'_{mp}, \psi_{np}; \beta_{mp}, \beta_{np}, \alpha)}{2\sqrt{\sin\beta_{mp}\sin\beta_{np}}}$$

(2.33)

$$\vec{M}_{dm}(l') = -\sum_{p=1}^{P_m} \sqrt{\frac{8\pi}{jk}} \left(\hat{e}_{mp,i}^+ \cdot \hat{l}'\right) \frac{D_s(\psi'_{mp}, \psi_{np}; \beta_{mp}, \beta_{np}, \alpha)}{2|\sin\psi_{np}|\sqrt{\sin\beta_{mp}\sin\beta_{np}}}$$

$$\cdot \left[\hat{\eta}\sqrt{1 - \left(\hat{l}' \cdot \hat{k}_{mp}\right)^2} + \hat{\eta} \times \hat{n}\left(\hat{l}' \cdot \hat{k}_{mp}\right)\cos\psi_{np}\right]$$

(2.34)

where

ψ'_{mp}, β_{mp} = wedge diffraction angles associated with the mp^{th} ray-optical incident modal field,

ψ_{np}, β_{np} = wedge diffraction angles associated with the np^{th} ray-optical reflected modal field,

$\hat{\eta}$ = waveguide axial direction,

$\hat{n}$ = unit vector normal to the waveguide walls,

$\hat{k}_{mp}$ = direction of propagation of the mp^{th} incident ray-optical field.

The GTD wedge diffraction coefficients $D_{s,h}$ are given by (2.24) and the associated angles are defined in Figure 15. Note that the expressions for the equivalent magnetic current sources depend on the modal ray angles of the nth reflected mode ψ_{np} and β_{np}. This is because the equivalent currents are not isotropic, i.e., they radiate with different strength in different directions to reproduce the correct scattered field. Therefore, to be consistent with reciprocity, the radiation by the equivalent currents is evaluated in the direction of the modal rays of the reflected modal field.

The elements of $[S_{22}]$ can now be found by substituting (2.33) and (2.34) into (2.31) and integrating. The junction scattering matrices $[S'_{11}]$ and $[S'_{22}]$ are

found in exactly the same way as $[S_{22}]$ except that the rim at the open end is replaced by the junction between waveguide sections. Also, for the case of $[S_{11}']$, the incident modes now propagate in the $-\hat{\eta}$ direction and the reflected modes now propagate in the $+\hat{\eta}$ direction. The expressions for the elements of these two scattering matrices will therefore not be repeated here.

It has been found that if the junction between two waveguide sections is fairly smooth, i.e., their is no slope discontinuity, the junction reflection matrices can most often be neglected [6,7] (all elements are assumed to be zero). In addition, if the reflection matrix of the open end $[S_{22}]$ is negligible compared to the termination reflection matrix $[S_\Gamma]$ (or the elements of both are small), $[S_{22}]$ can also be excluded. These two approximations are usually valid for most open-ended waveguide cavity configurations of interest and greatly simplify the analysis. A close examination of the scattering centers of a particular waveguide cavity and their higher order interactions should suggest what approximations are reasonable.

It should be mentioned that in some separable waveguide geometries there exist modes which have regions where the fields can not be expressed ray-optically in closed form. This occurs in the transition zones between regions of real ray-optical fields and evanescent fields, or in regions near caustics. The evanescent fields can be expressed as ray-optical fields which have been analytically extended to complex space and can therefore be handled by an analytic extension of the GTD wedge diffraction coefficient. However, this is usually not necessary because these fields are small due to their evanescent nature and can be neglected. But the fields in the transition region are sometimes not negligible and should be included using some other method, such as a complex plane wave spectral expansion of the modal fields [8]. The annular waveguide of Appendix A propagates such a mode, called a whispering gallery mode, which is ray-optic in the region near the outer
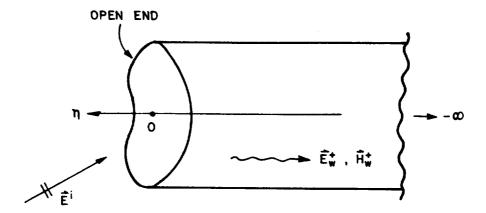
Figure 19: Open-ended semi-infinite waveguide illuminated by a plane wave which couples into waveguide modes.

wall, evanescent in the region near the inner wall, and has a transition (caustic) region between the two.

2.2.3 The transmission scattering matrices of the open end [S_{12} and $[S_{21}]$, and junctions $[S'_{12}]$ and $[S'_{21}]$.

Figure 19 shows the geometry for finding $[S_{21}]$, the transmission type scattering matrix which relates the components of the plane wave incident on the open end of a semi-infinite waveguide to the coefficients of the coupled modal fields propagating away from the open end. As before, these coupled modal fields can be written as a sum of $-\hat{\eta}$ propagating waveguide modes as

$$\left(\vec{E_w^-}, \vec{H_w^-}\right) = \sum_{n=1}^{N} C_n^- \left(\hat{e}_n^-, \hat{h}_n^-\right) e^{j\beta_n \eta}. \tag{2.35}$$

$[S_{21}]$ is then defined by

$$[C^-] = [S_{21}] \begin{bmatrix} A_\theta^i \\ A_\phi^i \end{bmatrix} \tag{2.36}$$

and is of order $N \times 2$, as mentioned earlier, and $[C^-]$ is a column matrix of order N.

40

The coefficients C_n^- of the coupled modal field are found again by using the modal excitation Equation of (2.27). The currents used in the integral of (2.27) are the equivalent currents of the physical theory of diffraction (PTD) [3,11,12] which replace the effects of the open end of the semi-infinite waveguide. These equivalent currents are, of course, based on the fields of the incident plane wave in the open end. The modal coefficients can be written for this case as (setting $\eta = 0$ in the open end)

$$
\begin{aligned}
C_n^- \ = \ & \frac{1}{2 \int \int_S \hat{e}_{nt} \times \hat{h}_{nt} \cdot \hat{\eta} dS} \left[\int \int_{open \ end} \left(\hat{e}_n^+ \cdot \vec{J}_s - \hat{h}_n^+ \cdot \vec{M}_s \right) dS \right. \\
& \left. + \int_{rim} \hat{h}_n^+ \cdot \left(\vec{M}_l^u + \vec{M}_d^u \right) dl' \right].
\end{aligned}
\tag{2.37}
$$

The first integral in (2.37) is an integration over the physical optics (PO) currents on the surface defined by the open end given simply by

$$
\vec{J}_s \ = \ \hat{n} \times \vec{H}^i
\tag{2.38}
$$

$$
\vec{M}_s \ = \ \vec{E}^i \times \hat{n}
\tag{2.39}
$$

where

$\hat{n}$ = unit surface vector of the open end pointing into the

waveguide region.

The second integral in (2.37) is a line integration over the Ufimtsev equivalent magnetic line and dipole edge sources [11,12] coinciding with the rim at the open end. Figure 20 shows the equivalent geometry with the open end replaced by surface and line current sources in an infinite waveguide region.

Again using the ECM, the Ufimtsev magnetic current sources are given similarly to (2.33) and (2.34) by [6]

$$
\vec{M}_l^u \ = \ -\hat{l}' \sum_{p=1}^{P_m} \frac{1}{Y_o} \sqrt{\frac{8\pi}{jk}} \left(\vec{H}^i \cdot \hat{l}' \right) \frac{D_h^u(\psi', \psi_{np}; \beta, \beta_{np})}{2\sqrt{\sin \beta \sin \beta_{np}}}
\tag{2.40}
$$

41

EQUIVALENT LINE AND SURFACE
CURRENTS REPLACING OPEN END
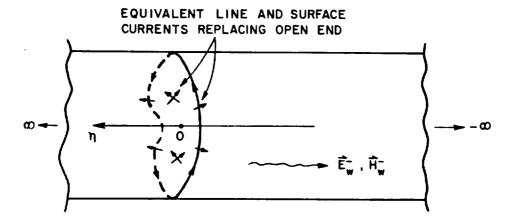
Figure 20: Equivalent surface and line sources replacing the open end of the
semi-infinite waveguide of Figure 19.

$$\vec{M}_d^u = \hat{\eta} \sum_{p=1}^{P_m} \sqrt{\frac{8\pi}{jk}} \left(\vec{E}^i \cdot \hat{l}'\right) \frac{D_s^u(\psi', \psi_{np}; \beta, \beta_{np})}{2|\sin\psi_{np}|\sqrt{\sin\beta \sin\beta_{np}}} \qquad (2.41)$$

where

$D_{s,h}^u$ = Ufimtsev's wedge diffraction coefficients,

ψ', β = wedge diffraction angles associated with the incident plane

wave,

ψ_{np}, β_{np} = wedge diffraction angles associated with the pth modal ray of

the nth coupled mode

$\hat{l}'$ = unit vector along the rim

$\hat{\eta}$ = waveguide axial direction.

The angles associated with the PTD wedge diffraction coefficient are defined in Fig-
ure 15. After substituting Equations (2.38) thru (2.41) into (2.37) and integrating,
the elements of $[S_{21}]$ can easily be identified and extracted.

The Ufimtsev equivalent currents of (2.40) and (2.41) are corrections to the
PO currents of (2.38) and (2.39) and they may be neglected for most open-ended

42

waveguide geometries of interest leading to the Kirchhoff approximation which simplifies the analysis considerably. Cases where the Ufimtsev currents should be included are for waveguides which do not have a large cross-section (in wavelength) and for cases of very steep incidence angles (i.e., very far off axis or near grazing).

As might be expected, there is a simple relationship between $[S_{12}]$ and $[S_{21}]$ which eliminates the need to calculate the elements of $[S_{12}]$ independently. This relationship is derived via reciprocity and is given by [5,6]

$$[S_{12}]^T = -2 \left[\int \int_S \hat{e}_{nt} \times \hat{h}_{nt} \cdot \hat{\eta} dS \right] [S_{21}] \qquad (2.42)$$

where

$$\left[\int \int_S \hat{e}_{nt} \times \hat{h}_{nt} \cdot \hat{\eta} dS \right] = \text{diagonal matrix of order } N \times N,$$

$$[S_{12}]^T = \text{transpose of } [S_{12}].$$

The transmission type scattering matrix $[S'_{21}]$ which relates the coefficients of the modal field incident on a junction between two semi-infinite waveguides to the coefficients of the modal field coupled through the junction into the second waveguide region, is found in an analogous manner to $[S_{21}]$. Figure 21 shows the geometry.

Let the incident modal field of the left waveguide be given by

$$\left(\vec{E}_w^i, \vec{H}_w^i \right) = \sum_{n=1}^{N} C_n^- \left(\hat{e}_n^-, \hat{h}_n^- \right) e^{j\beta_n \eta} \qquad (2.43)$$

and let the transmitted modal field of the right waveguide be given by

$$\left(\vec{E}_w^t, \vec{H}_w^t \right) = \sum_{m=1}^{M} D_m^- \left(\hat{e}_m'^-, \hat{h}_m'^- \right) e^{j\beta_m' \eta'} \qquad (2.44)$$

where the primed quantities indicate they are of the modal fields of the waveguide on the right. Note that in general the modal fields of the two waveguides are

43
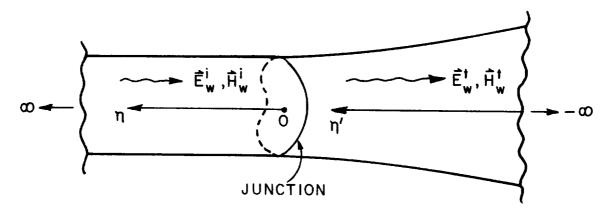
Figure 21: Junction between two semi-infinite waveguide sections with an
incident and transmitted modal field.

different and there are a different number of included modes. $[S'_{21}]$ is then defined
by

$$[D^-] = [S'_{21}][C^-] \qquad (2.45)$$

and is of order $M \times N$, as mentioned earlier. Similar to (2.37), the nm^{th} element
of $[S'_{21}]$ is simply the coefficient of the mth transmitted mode due to a single n^{th}
mode incident on the junction and is given by

$$[S'_{21}]_{nm} = \frac{1}{2\int\int_S \hat{e}'_{mt} \times \hat{h}'_{mt} \cdot \hat{\eta}' dS} \left[\int\int_{junction} \left(\hat{e}'^+_m \cdot \vec{J}_{sn} - \hat{h}'^+_m \cdot \vec{M}_{sn} \right) dS \right.$$
$$\left. + \int_{edge} \hat{h}'^+_m \cdot \left(\vec{M}^u_{ln} + \vec{M}^u_{dn} \right) dl' \right] \qquad (2.46)$$

where

$$\vec{J}_{sn} = \hat{n} \times \hat{h}^-_n \qquad (2.47)$$

$$\vec{M}_{sn} = \hat{e}^-_n \times \hat{n} \qquad (2.48)$$

$\hat{n}$ = unit surface normal of junction pointing into the waveguide

on the right,

$$\vec{M}^u_{ln} = -\hat{l}' \sum_{p=1}^{Pn} \frac{1}{Y_o} \sqrt{\frac{8\pi}{jk}} \left(\hat{h}^-_{np,i} \cdot \hat{l}' \right) \frac{D^u_h(\psi'_{np}, \psi_{mp}; \beta_{np}, \beta_{mp})}{2\sqrt{\sin \beta_{np} \sin \beta_{mp}}} \qquad (2.49)$$

44

$$\vec{M}_{dn}^u = \hat{\eta} \sum_{p=1}^{P_n} \sqrt{\frac{8\pi}{jk}} \left(\hat{e}_{np,i}^- \cdot \hat{l}'\right) \frac{D_s^u(\psi_{np}', \psi_{mp}; \beta_{np}, \beta_{mp})}{2|\sin\psi_{mp}|\sqrt{\sin\beta_{np}\sin\beta_{mp}}} \qquad (2.50)$$

and

ψ_{np}', β_{np} = wedge diffraction angles associated with the np^{th} ray-optical incident modal field,

ψ_{mp}, β_{mp} = wedge diffraction angles associated with the mp^{th} ray-optical transmitted modal field,

$\hat{l}'$ = unit vector along the edge of the junction,

$\hat{\eta}$ = waveguide axial direction for the waveguide on the left,

$\hat{\eta}'$ = waveguide axial direction for the waveguide on the right.

The angles associated with the PTD wedge diffraction coefficients $D_{s,h}^u$ are defined in Figure 15. Equations (2.47) thru (2.50) can now be substituted into (2.46) and integrated to give the elements of $[S_{12}']$. Once again it is noted that the radiation from the Ufimtsev equivalent currents of (2.49) and (2.50) does not contribute significantly and may therefore be neglected (as in the Kirchhoff approximation) especially for junctions between waveguide sections which are smooth and continuous and for large waveguide cross-sections. However, the Ufimtsev current contributions become more important for smaller waveguides and for junctions which are highly discontinuous or abrupt, and so they should therefore be included for such cases.

The transmission type scattering matrix $[S_{12}']$ which is defined by

$$[C^+] = [S_{12}'][D^+] \qquad (2.51)$$

and is of order $N \times M$ is found in exactly the same way as $[S_{21}']$ except that the incident modal field is from the waveguide on the right in Figure 21 and the
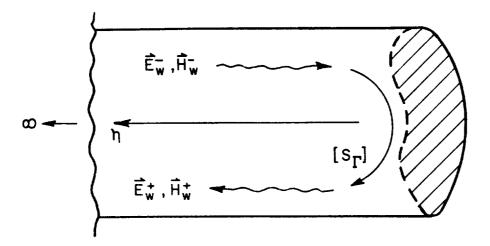
Figure 22: Termination geometry for finding $[S_\Gamma]$.

transmitted field propagates in the $+\hat{\eta}$ direction in the waveguide on the left. Therefore, the expressions for the elements of $[S'_{12}]$ will not be repeated here. Although there does not appear to be a simple reciprocal relationship between $[S'_{12}]$ and $[S'_{21}]$ for the general case as might be expected, there often is such a relationship for some specific cases. For example, in [7] it is shown that these matrices are transposes of each other for the case of a junction between a parallel-plate and annular waveguide.

2.2.4 The termination scattering matrix $[S_\Gamma]$.

The reflection type termination scattering matrix $[S_\Gamma]$ relates the coefficients of the modal field incident on the termination of the waveguide cavity to the coefficients of the reflected modal field. The geometry is shown in Figure 22. Let the incident modal field be given by

$$\left(\vec{E}_w^-, \vec{H}_w^-\right) \;=\; \sum_{n=1}^{N} C_n^- \left(\hat{e}_n^-, \hat{h}_n^-\right) e^{j\beta_n \eta} \tag{2.52}$$

46

and the reflected modal field by

$$\left(\vec{E}_w^+, \vec{H}_w^+\right) \ = \ \sum_{n=1}^{N} C_n^+ \left(\hat{e}_n^+, \hat{h}_n^+\right) e^{-j\beta_n \eta}. \tag{2.53}$$

$[S_\Gamma]$ is then defined by

$$[C^+] \ = \ [S_\Gamma][C^-] \tag{2.54}$$

and is of order $N \times N$ as mentioned earlier.

For simple terminations, such as a perfectly conducting or impedance surface which is everywhere transverse to the axial coordinate η, it is a straightforward task to find $[S_\Gamma]$ by enforcing boundary conditions on the termination surface. For these two cases, it is easy to show that $[S_\Gamma]$ is always diagonal using the orthogonality property of the modes and conservation of power. In other words, the nth incident mode reflects only into the nth reflected mode. For a perfectly conducting termination and the mode conventions used here, $[S_\Gamma] = -[I]$, the negative of the identity matrix of order $N \times N$. This is easy to see by requiring that the tangential electric field vanishes on the termination surface, and using the modal decomposition of (2.28).

For an impedance surface at the termination, the ratio of the tangential electric and magnetic fields is defined by

$$\frac{E_t}{H_t} \ = \ Z_s \tag{2.55}$$

where

$$Z_s \ = \ \text{equivalent surface impedance}$$

It is assumed that the vector directions of the tangential electric and magnetic fields are orthogonal. This is true if the waveguide modes are separated into

47

transverse-to-η electric (TE_η) and magnetic (TM_η) categories. For TE_η modes the axial electric field $\hat{e}_{n\eta}$ is zero, and for TM_η modes the axial magnetic field $\hat{h}_{n\eta}$ is zero. Furthermore, it can be shown that if the waveguide modes are separated into TE_η and TM_η categories, then the transverse electric and magnetic fields of any given mode have the same functional form and are related by a constant, as well as being orthogonal.

In terms of the nth incident and reflected modes, using (2.28) and (2.29), (2.55) can be written as

$$\frac{e_{nt} + [S_\Gamma]_{nn} e_{nt}}{-h_{nt} + [S_\Gamma]_{nn} h_{nt}} = Z_s \qquad (2.56)$$

where

$$e_{nt}, h_{nt} = \text{scalar portions of } \hat{e}_{nt} \text{ and } \hat{h}_{nt}, \text{ respectively,}$$

$$[S_\Gamma]_{nn} = n^{th} \text{ diagonal element of } [S_\Gamma].$$

Solving (2.56) gives the elements of $[S_\Gamma]$ for the impedance termination as

$$[S_\Gamma]_{mn} = \begin{cases} \frac{Z_s h_{nt} + e_{nt}}{Z_s h_{nt} - e_{nt}} & : \text{ for } m = n \\ 0 & : \text{ for } m \neq n. \end{cases} \qquad (2.57)$$

It is noted that h_{nt} and e_{nt} are functions of the transverse coordinates of the waveguide, which would suggest that the elements of (2.57) are not constant. However, as mentioned above, it can be shown that h_{nt} and e_{nt} always have the same functional form, which will cancel itself in (2.57), provided the waveguide modes are divided into TE_η and TM_η categories. Also, it is clear from (2.57) that for a perfectly conducting termination ($Z_s = 0$), $[S_\Gamma]$ is the negative of the identity matrix, as expected.

For more complicated terminations it is not nearly so easy to find $[S_\Gamma]$. It is necessary to resort to other methods such as high-frequency asymptotic approximations and the method of moments. In [5], the reflection matrix for planar blade

48

structures with concentric conical or hemispherical hubs terminating a circular waveguide was found approximately using physical optics (PO). The termination was replaced with equivalent PO currents due to an incident mode and these currents were then allowed to radiate inside the waveguide, exciting reflected modes. Also in [5], a termination which was an open-ended circular waveguide was also analyzed. This reflection matrix was found in the same way as $[S_{22}]$ was found earlier in Section 2.3.2 of this chapter using the hybrid modal method. In [8], the reflection matrix for some simple 2-D waveguide terminations was found using the method of moments. In this method, the termination is replaced with unknown surface currents excited by an incident mode inside the waveguide. These unknown currents are solved for using the method of moments, adapted to the interior waveguide problem. These currents then radiate inside the waveguide exciting reflected modes.

Currently, research is under way at The Ohio State University ElectroScience Laboratory to find a means of obtaining $[S_\Gamma]$ experimentally so that terminations of arbitrary complexity could be coupled to the open-ended waveguide. This would be a very useful tool because many realistic terminations are of such size and complexity that they are nearly impossible to model using analytic techniques.

2.3 Numerical Results and Discussion of the Hybrid Modal Method

In this section some numerical results obtained using the hybrid asymptotic modal method will be presented and in some cases will be compared with measurement. All of the results of this section have appeared in previous reports and publications, and the appropriate references will be cited. Because of its accuracy, the hybrid modal method will be used again in later chapters as a reference solution for comparison against more approximate methods.

In [5], perfectly conducting, single section rectangular and circular open-ended waveguide cavities with cone/hub and disk/blade terminations were analyzed using the methods of this chapter as indicated earlier. The modal termination reflection matrix $[S_\Gamma]$ was obtained by replacing the conducting terminations with their physical optics (PO) currents due to an incident mode, and then finding the excitation of the reflected modes radiated by these currents inside an equivalent waveguide of infinite extent. Figure 23 shows a typical backscatter (RCS) vs. aspect angle result from [5], compared with a measurement performed in the indoor compact range at The Ohio State University ElectroScience Laboratory (OSU-ESL). Figure 24 shows a typical RCS vs. frequency result from [5], compared with a measurement from OSU-ESL. It was found that the calculations agreed well with the measurements and that the terminations used did not drastically change the overall pattern features when compared to a simple planar "short circuit" termination, for the relatively small guide cross-sections considered. Also, as Figure 24 indicates, the measured data from such cavities is very sensitive to frequency. This suggests that imperfections in the dimensions of the model and its alignment in the compact range could significantly affect the accuracy of the measurement when compared with calculations based on a perfect geometry.

Perfectly conducting open-ended waveguide cavities made up of more than one waveguide section were discussed in [6], with emphasis placed on modal reflection from and transmission through the junctions between waveguide sections and the open end. A more detailed presentation of modal rays for some common uniform waveguide geometries is also found in [6], along with a derivation of the reciprocity relationship between $[S_{12}]$ and $[S_{21}]$. Figure 25 shows some typical RCS vs. aspect angle results and Figure 26 shows a typical RCS vs. frequency result, from [6] based on the hybrid modal method and compared with measurements obtained at OSU-

50

ESL. Figure 27 shows the inverse Fourier transform of the frequency data of Figure 26 which shows the scattering centers in the time domain. It is easy to distinguish between the scattering by the rim at the open end and the scattering by the planar termination using this technique.

Another interesting result which was discussed in [6] and [13] is the selective modal property of the coupling of the incident plane wave into waveguide modes. Simply stated, the modes most strongly excited by a plane wave incident on the open end of the guide are those whose mode angles are closest to the direction of the plane wave. Using this principle, many of the propagating modes can be neglected for a given incidence angle because they are too weakly excited. This can greatly improve the efficiency of the hybrid modal method, for cases where the selective modal property is applicable, especially for large waveguide cross-sections which would otherwise allow too many propagating modes to be tractable. Figure 2 in the introduction demonstrates this principle with a result from [6] where an RCS vs. aspect angle pattern calculated using all of the propagating modes is compared to one which uses only the three most strongly excited modes for each incidence angle. This particular waveguide cavity propagated over 100 modes at the frequency used in the calculation, implying a great savings in computation time.
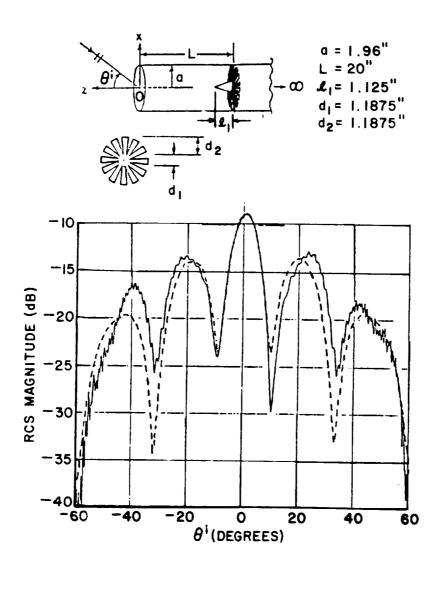
In [7], the scattering by a 2-D S-shaped waveguide cavity with a planar termination and slightly lossy inner walls was analyzed using the hybrid modal method. The S-shape was achieved by joining together parallel-plate and annular waveguide sections alternately. Because a junction between these two types of waveguides is smooth, it was found that the modal reflection from the junctions is very small and can be neglected, thus simplifying the analysis. The small loss of the waveguide walls was handled using a simple perturbation technique which required that

51

the equivalent surface impedance of the walls be small. The corresponding lossless waveguide modes are then used with a perturbation to their propagation constants which causes them to attenuate as they travel. Figure 28 shows a typical backscatter vs. angle result for a straight cavity and an S-shaped cavity, with and without loss. The loss was due to a thin absorbing layer covering perfectly conducting walls, which caused approximately 1 dB of loss to occur per reflection near normal incidence. The scattering by just the rim at the open end is also shown on the plots. As Figure 28 suggests, the effect of the S-shape is to flatten out and lower the overall pattern and to make the absorber coating have more effect, especially near axial incidence.

The scattering by a 3-D version of the S-shaped cavity was done in [9], but no loss was included. This was because there is no simple way to use the perturbation method for 3-D waveguides in which there exists a power coupling between modes. The exact modal fields could be found for a uniform 3-D waveguide with impedance walls, but (a) this requires complicated numerical solutions to the eigenvalue equations, (b) there is power coupling between modes (i.e., the modes do not carry power independently of all other modes) which does not occur for the lossless case, and (c) the modal rays would become complex and not lend themselves easily to the hybrid asymptotic modal method. Figure 29 shows a typical backscatter vs. angle result from [9] for a straight rectangular cavity and Figure 30 shows one for a 3-D S-shaped cavity.

In [8], the scattering by single section, perfectly conducting, 2-D linearly tapered and parallel-plate waveguide cavities with plane and plug terminations was found using the hybrid modal method. The modal termination reflection matrix $[S_\Gamma]$ was found using the method of moments, providing a highly accurate result. Figure 31 shows a typical backscatter vs. aspect angle result from [8] where the

effect of a wedge-shaped plug termination is compared with a planar termination. As expected, the plug redistributes the scattered energy such that the return is reduced near axial incidence, as opposed to the planar termination which gives a maximal return in that region.

Figure 23: Comparison of calculated and measured RCS patterns of an open-ended circular waveguide cavity with a hub and blade termination at 10 GHz, perpendicular polarization.
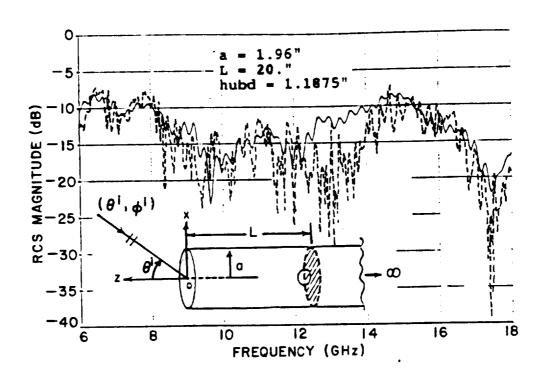
Figure 24: Comparison of calculated and measured RCS vs. frequency of an open-ended circular waveguide cavity with a disk and hemispherical hub termination, parallel polarization, $\theta^i = 15°$, $\phi^i = 0°$.

55

(a) $\vec{E}^i = \hat{\phi}$, $\phi = 0°$ plane
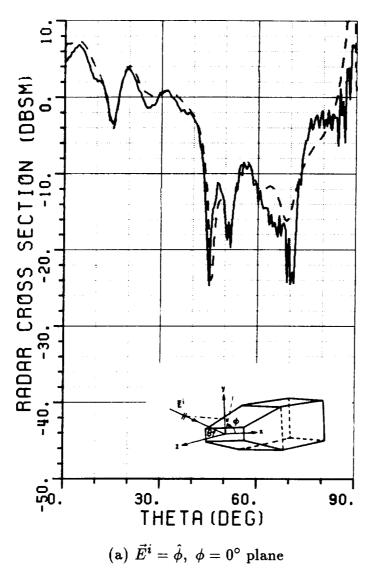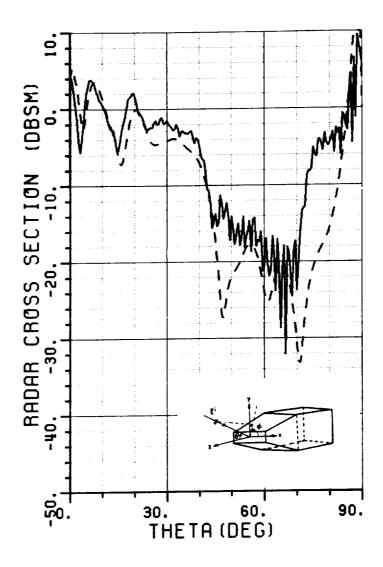
Figure 25: Comparison of calculated and measured RCS patterns of an open-ended waveguide cavity with a planar termination, made up of a linearly tapered and a rectangular waveguide section, at 10 GHz.
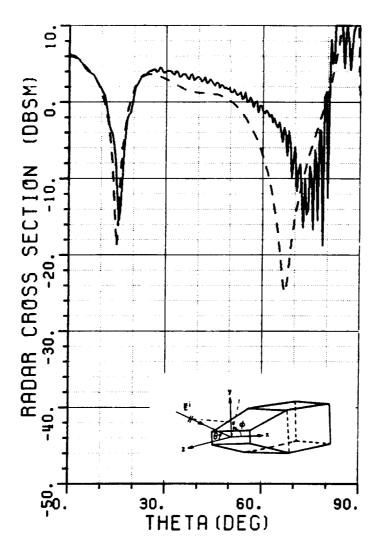
— measured, - - calculated

(b) $\vec{E}^i = \hat{\theta}$, $\phi = 0°$ plane

Figure 25: (continued)
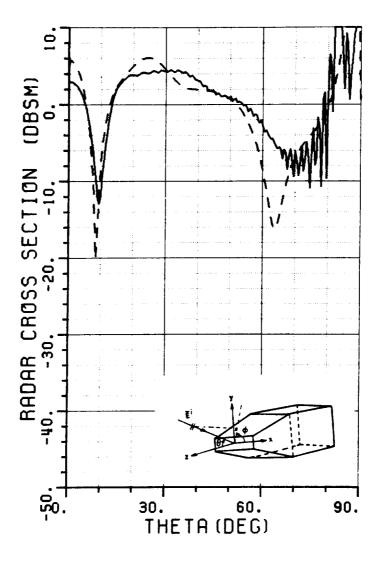
— measured, - - calculated

(c) $\vec{E}^i = \hat{\theta}$, $\phi = 90°$ plane

Figure 25: (continued)

— measured, - - calculated

58

(d) $\vec{E}^i = \hat{\phi}$, $\phi = 90°$ plane

Figure 25: (continued)

— measured, - - calculated
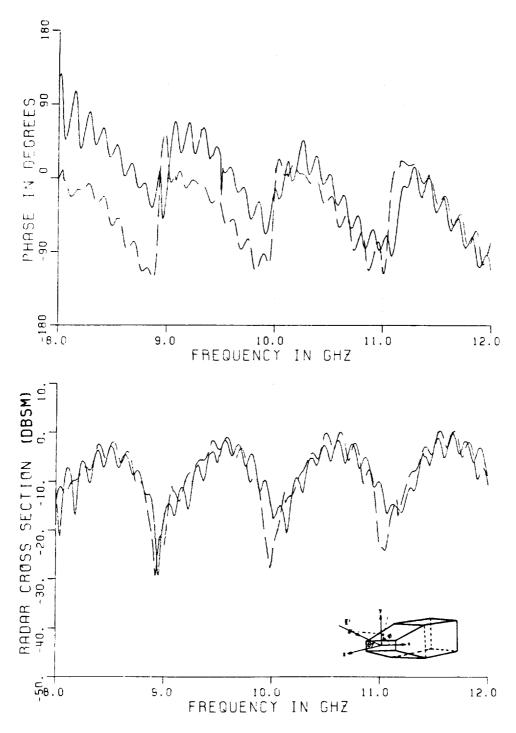
Figure 26: Comparison of calculated and measured RCS variation with frequency of the cavity of Figure 25, $\vec{E}^i = \hat{\phi}$, $\phi = 0°$, $\theta = 45°$.

———— measured, — — calculated

60
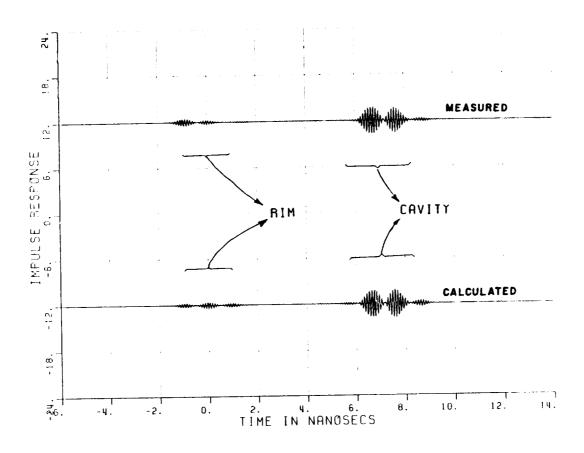
Figure 27: Inverse Fourier transforms of the results in Figure 26, i.e., time domain plots isolating the scattering centers.
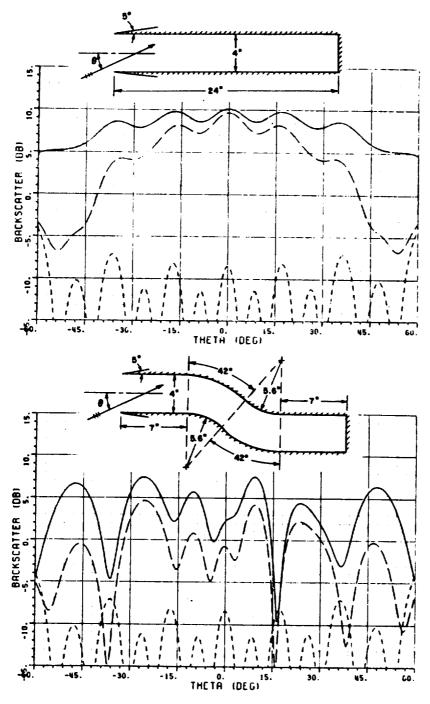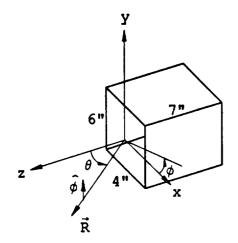
Figure 28: Backscatter from a 2-D straight and S-shaped cavity with a short circuit termination, perpendicular polarization at 10 GHz.
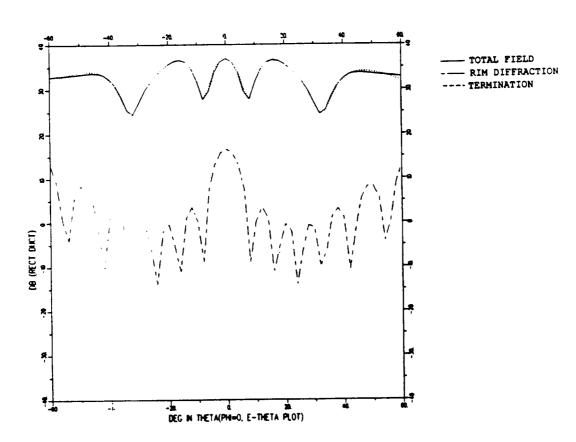
—— no loss, — — 1 dB loss/reflection, - - - - rim diffracted

62

Rectangular Duct
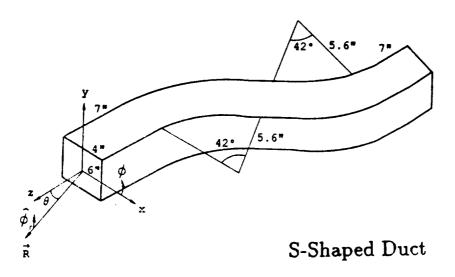
Width= 4 inches, Height= 6 inches

With 99 propagating Modes at 10 Ghz

TOTAL FIELD
RIM DIFFRACTION
TERMINATION

DB (RECT DUCT)

DEG IN THETA(PHI=0, E-THETA PLOT)
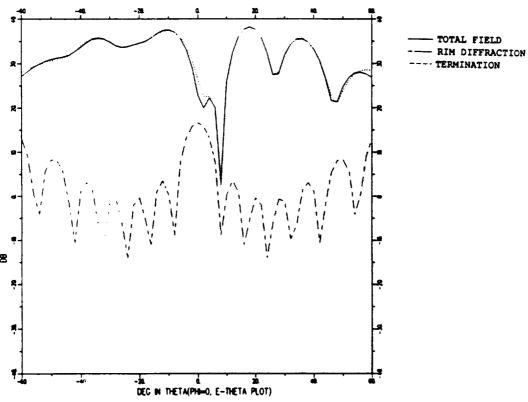
Backscattered E-Theta Plot

Figure 29: Backscatter pattern of a lossless straight rectangular cavity with a planar termination, perpendicular polarization.

63

S-Shaped Duct

99 rect modes. 105 annular modes at 10 Ghz

Backscattered E-Theta Plot

Figure 30: Backscatter pattern of a lossless 3-D S-shaped cavity with a planar termination, perpendicular polarization.

64
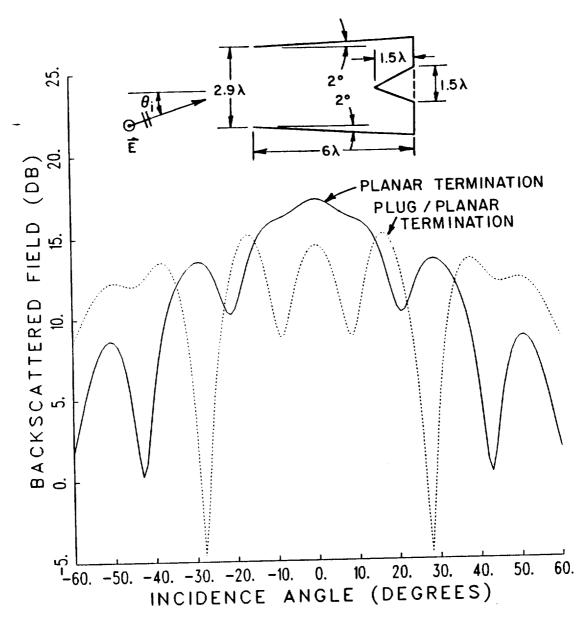
Figure 31: Backscatter patterns of a 2-D linearly tapered waveguide cavity with a planar termination and a plug termination, perpendicular polarization.

CHAPTER III

THE GEOMETRICAL OPTICS RAY SHOOTING METHOD

The geometrical optics (GO) ray shooting method has been used to analyze much more general open-ended cavity geometries than the hybrid modal method could handle [7], [14]-[19]. In the hybrid modal method of Chapter II, the cavity geometries were limited to ones which could be made up of finite sections of uniform waveguides for which the modal fields could be written in closed form as an eigenfunction expansion. In addition, these waveguide sections would have to be perfectly conducting, or nearly perfectly conducting as in the modal perturbation technique used in [7]; otherwise, a great deal of complexity and numerical analysis gets added to the modal method. Examples of the modal analysis of non-perfectly conducting waveguide cavities appear in [15] for a parallel plate waveguide and in [16] for a circular waveguide. Finally, the number of propagating modes involved in the hybrid modal analysis increases exponentially with frequency. Therefore, while the hybrid modal method is highly accurate, it also becomes more difficult to use for many realistic cavity geometries of interest. However, the usefulness of the hybrid modal method becomes evident when it is used to validate more general and approximate methods, such as the ones described in this and the next two chapters.

In the GO ray tracing method, also referred to as "shooting and bouncing rays" (SBR) [17], the incident plane wave field which enters the cavity is broken

up into a dense grid of parallel ray-tubes. The central ray of each ray-tube is then traced via the laws of GO inside the cavity and the field in any transverse cross-section of the ray-tube is assumed to be that of the central ray. Also it is often assumed that the exact shape of the ray-tube is relatively arbitrary as long as the cross-sectional area is known. These two assumptions are reasonable if the cross-sectional area of each ray-tube is kept to less than $\left(\frac{1}{2}\lambda\right)^2$ where λ is the free space wavelength [18].

It is possible to trace the boundary rays of the ray-tubes in order to know the exact shape of the cross-section and thus allow larger ray-tubes [17,18], but this may not be desirable because larger ray-tubes sample a larger portion of the cavity walls which they reflect from, and therefore may lose some information on the geometry. Also, since the ray tubes are eventually integrated in some way, such as in an aperture radiation integration (Appendix B) or the termination reciprocity integral (Appendix C), it may be difficult to integrate ray-tubes of irregular shapes [17,18]. It is very convenient to be able to pick an arbitrary ray-tube shape which allows for a simple integration.

The advantage of the GO ray tracing method (SBR) is that it can handle very general cavity geometries with many possible surface characteristics, as long as the reflections of the rays by the interior cavity walls dominate the interior scattering effects. Also, the ray tracing part of the method is relatively frequency independent so that it is feasible to extract a fairly broad band of frequency data from a single set of traced rays. However, the GO method neglects all higher order effects such as diffraction. Probably the most important of these higher order effects which are not included is the part of the incident field which enters the cavity via diffraction by the edge at the open end. Of course these effects diminish as the frequency increases because the GO field is the only term left in the high

frequency asymptotic series of the EM field as the frequency approaches infinity. Other disadvantages of the GO method are that a new grid of rays must be traced for each new incidence angle, and the incident field must always be ray-optical.

In this chapter, the theory behind the launching and tracking of the ray-tubes and their subsequent integration will be discussed and some numerical results will follow. The actual tracking of the GO field will be referred to as the GO ray shooting method. When this is combined with an aperture integration (AI) it will be referred to as the GO/AI method, and when it is combined with the reciprocity integral (RI) it will be referred to as the GO/RI method.

3.1 Formulation of the Geometrical Optics Ray Tracing Method

3.1.1 Launching the ray-tubes.

In the GO ray tracing method, the incident plane wave field which passes through the open end of the cavity is divided up into a dense grid of parallel ray-tubes which normally have a square cross-section. This is illustrated in Figure 32 for a 2-D geometry. The fields of each ray-tube are then tracked using the laws of GO through the cavity to some required location, such as to the termination as in the GO/RI method, or down and back to the open end as in the GO/AI method. Figure 33 shows one such ray-tube.

As the ray-tube undergoes reflections from curved surfaces, it experiences changes in its divergence (curvature or spreading factor) and the shape of the ray-tube distorts. It is therefore necessary to have a way of keeping track of this divergence and shape change (in addition to phase propagation, polarization and reflection coefficients) in order to know the fields inside the ray-tube. There are several ways of doing this. One way is to ray trace the central ray of the ray-tube using the laws of GO to give the field in the center of the ray-tube, and then trace
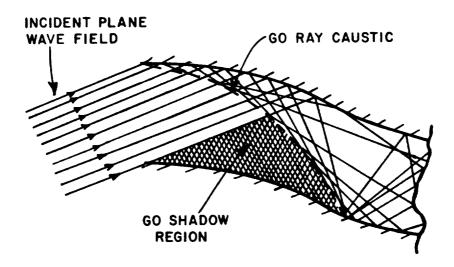
Figure 32: Grid of ray-tubes entering a 2-D open-ended cavity in the GO ray tracing method.
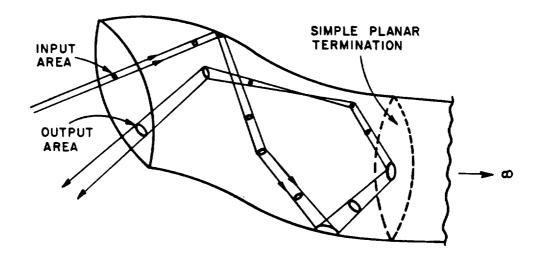
Figure 33: A single ray-tube tracked through a cavity until it exits via the open end.

the four corner rays geometrically, without keeping track of divergence, to give the shape of the ray-tube. It is then assumed that the fields anywhere in a cross-section of the ray-tube are the same as the field of the central ray. Another more approximate method ray traces the four corner rays without divergence to give the shape of the ray-tube (and therefore, the cross-sectional area), and the magnitude of the divergence is found by conserving the total power in the ray-tube (neglecting any loss associated with non-perfectly conducting walls). The magnitude of the field at a point P inside the ray-tube (without loss) is then given by

$$\left|\vec{E}(P)^{ll}\right| = \sqrt{\frac{A_{in}}{A(P)}} \left|\vec{E}_{in}\right| \tag{3.1}$$

where

$$\vec{E}(P)^{ll} = \text{electric field at } P \text{ assuming lossless walls,}$$

$$\vec{E}_{in} = \text{electric field at the input,}$$

$$A_{in} = \text{input cross-sectional area of ray-tube,}$$

$$A(P) = \text{cross-sectional area of ray-tube at } P.$$

This method reduces the complexity of GO by not requiring calculations involving the principle radii of curvature of the ray-tube and the curvature of surfaces the ray-tube reflects from. However, all information on the phase shifts associated with propagation through caustics is lost. It is noted that this method of tracking a ray-tube does not require that the ray-tube be less than $\left(\frac{1}{2}\lambda\right)^2$ in cross-sectional area as mentioned earlier.

Probably the easiest method which keeps information on caustics and divergence is to track the central ray of the ray-tube using GO and assume that the field in any transverse cross-section of the ray-tube is that of the central ray. The cross-sectional area of the ray-tube is known by conserving power as in (3.1). At

a point P in the ray-tube, the cross-sectional area is then given by

$$A(P) = \frac{\left|\vec{E}_{in}\right|^2}{\left|\vec{E}(P)^{ll}\right|^2} A_{in}.$$ (3.2)

In this ray-tube tracking method, the cross-sectional area is found from (3.2), but the exact shape of the ray-tube is unknown. However, if the area of the ray-tube is kept small enough, i.e., less than $\left(\frac{1}{2}\lambda\right)^2$, then the exact shape of the cross-section is relatively arbitrary and can be made into any convenient shape. This is demonstrated for a sample case in the aperture integration method in Appendix B. For example, the shape could be chosen to coincide nicely with the coordinate system in which the integral is evaluated. Of course the problem with this method is that a larger number of rays may have to be traced in order to keep the ray-tubes small enough.

3.1.2 GO ray tracing using curvature matrices.

An efficient means of tracing a given ray via the laws of geometrical optics is available through the use of curvature matrices which describe the curvatures of reflecting surfaces and the GO wavefront of a ray as it propagates and reflects [17]. The derivation of this method is found in [20,21,22] and the pertinent resulting equations are presented here. Consider the GO ray-tube shown in Figure 34 which propagates from point O to point P. According to GO, the field at P is related to the field at O by

$$\vec{E}(P) = (DF)\vec{E}(O)e^{-jks}$$ (3.3)

where (DF) is the divergence factor given by

$$(DF) = \frac{1}{\sqrt{1 + s/R_1}} \cdot \frac{1}{\sqrt{1 + s/R_2}}$$ (3.4)

71
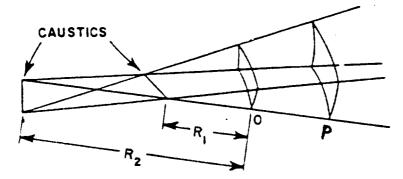
Figure 34: GO ray-tube propagating in free space and its caustics.

and

$$R_1, R_2 \quad = \quad \text{principal radii of curvature of the wavefront at } P \text{ (i.e., caustic}$$

distances),

$$s \quad = \quad \text{propagation distance from } O \text{ to } P.$$

The sign convention for the square roots in (3.4) is as follows:

$$\frac{1}{\sqrt{1 + s/R_{1,2}}} = \begin{cases} \left| \frac{1}{\sqrt{1+s/R_{1,2}}} \right| & : \text{ for } 1 + \frac{s}{R_{1,2}} > 0 \\ \\ \left| \frac{1}{\sqrt{1+s/R_{1,2}}} \right| e^{j\frac{\pi}{2}} & : \text{ for } 1 + \frac{s}{R_{1,2}} < 0 \end{cases} \qquad . \qquad (3.5)$$

The caustics shown in Figure 34 are points where the GO field becomes singular, as is evident from (3.3) and (3.4) if $s = -R_1$ or $s = -R_2$. However, in the application of GO to treat realistic open-ended cavities this has not been seen to be a serious problem, mainly because it is highly unlikely numerically that a caustic of a given ray-tube will occur exactly in the plane of integration, and if it is nearby it will tend to integrate to a finite value, as in a Cauchy principal value integral.

The principal radii of curvature R_1 and R_2 of a surface can be found from the curvature matrix $\overline{\overline{Q}}(P)$ at point P on the surface using

$$\frac{1}{R_{1,2}} = \frac{1}{2}\text{Tr}\overline{\overline{Q}}(P) \pm \frac{1}{2}\sqrt{\left[\text{Tr}\overline{\overline{Q}}(P)\right]^2 - 4\text{Det}\overline{\overline{Q}}(P)} \qquad (3.6)$$

where

$$\overline{\overline{Q}}(P) = 2 \times 2 \text{ curvature matrix at } P,$$

$$\text{Tr}\overline{\overline{Q}} = \text{trace of matrix } \overline{\overline{Q}},$$

$$\text{Det}\overline{\overline{Q}} = \text{determinant of matrix } \overline{\overline{Q}}.$$

Now the question arises, what exactly is $\overline{\overline{Q}}$ and how is it defined? Let an arbitrary parametric surface be defined by $\vec{r}(u,v)$, a vector from the origin to a loci of points, where (u,v) are the parametric coordinates on the surface, and let $\hat{N}(u,v)$ be the unit normal vector of the surface. The curvature matrix $\overline{\overline{Q}}$ is then defined by

$$-\begin{bmatrix} \hat{N}_u \\ \hat{N}_v \end{bmatrix} = \overline{\overline{Q}} \begin{bmatrix} \vec{r}_u \\ \vec{r}_v \end{bmatrix} \qquad (3.7)$$

where the subscript u or v denotes differentiation with respect to u or v. It is noted that $\vec{r}_u$, $\vec{r}_v$, $\hat{N}_u$ and $\hat{N}_v$ are tangent to the surface, but not necessarily orthogonal.

As examples, if $\vec{r}_u$ and $\vec{r}_v$ are the principle directions of the radii of curvature (and therefore orthogonal), then

$$\overline{\overline{Q}} = \begin{bmatrix} \frac{1}{R_1} & 0 \\ 0 & \frac{1}{R_2} \end{bmatrix}, \qquad (3.8)$$

or if the surface is planar then

$$\overline{\overline{Q}} = \begin{bmatrix} 0 & 0 \\ 0 & 0 \end{bmatrix}, \qquad (3.9)$$
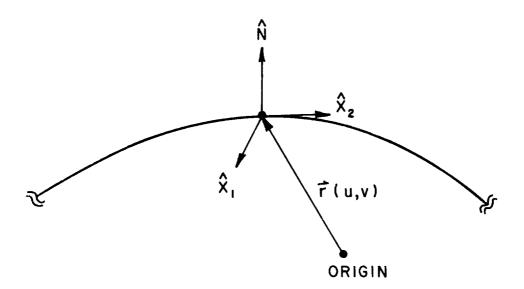
Figure 35: Parameterized surface with tangent vectors $\hat{x}_1$ and $\hat{x}_2$ and normal vector $\hat{N}$ on the surface.

but in general, the principal radii of curvature are related to $\overline{\overline{Q}}$ through (3.6).

To find the curvature matrix for a given surface defined by the parameterized vector $\vec{r}(u,v)$, refer to Figure 34 where $\hat{x}_1$ and $\hat{x}_2$ are arbitrary orthogonal unit vectors tangent to the surface. The curvature matrix for this surface is then given by

$$\overline{\overline{Q}} = \overline{\overline{V}}^{-1} \begin{bmatrix} \tilde{Q}_{11} & \tilde{Q}_{12} \\ \tilde{Q}_{21} & \tilde{Q}_{22} \end{bmatrix} \overline{\overline{V}} \tag{3.10}$$

where

$$\overline{\overline{V}} = \begin{bmatrix} \vec{r}_u \cdot \hat{x}_1 & \vec{r}_u \cdot \hat{x}_2 \\ \vec{r}_v \cdot \hat{x}_1 & \vec{r}_v \cdot \hat{x}_2 \end{bmatrix} \tag{3.11}$$

$$\tilde{Q}_{11} = \frac{eG - fF}{EG - F^2}, \quad \tilde{Q}_{12} = \frac{fE - eF}{EG - F^2}$$

$$\tilde{Q}_{21} = \frac{fG - gF}{EG - F^2}, \quad \tilde{Q}_{22} = \frac{gE - fF}{EG - F^2} \tag{3.12}$$

$$E = \vec{r}_u \cdot \vec{r}_u, \quad F = \vec{r}_u \cdot \vec{r}_v, \quad G = \vec{r}_v \cdot \vec{r}_v$$

74
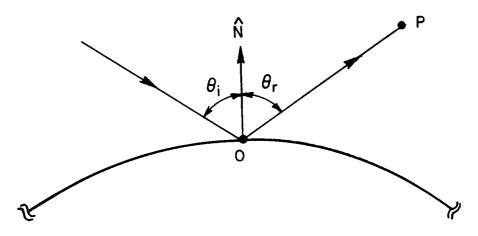
Figure 36: GO reflection of a ray from a curved surface.

$$e = \vec{r}_{uu} \cdot \hat{N}, \quad f = \hat{r}_{uv} \cdot \hat{N}, \quad g = \vec{r}_{vv} \cdot \hat{N}. \qquad (3.13)$$

The double subscripts uu, uv and vv denote second derivatives.

It remains to be seen how the curvature matrix of a ray-tube changes as it propagates and as it reflects off curved surfaces. Again referring to Figure 34, the curvature matrix at P is related to the curvature matrix at O according to the propagation relation

$$\overline{\overline{Q}}(P) = \left\{ \left[\overline{\overline{Q}}(O) \right]^{-1} + s\overline{\overline{I}} \right\}^{-1} \qquad (3.14)$$

where

$$\overline{\overline{I}} = \begin{bmatrix} 1 & 0 \\ 0 & 1 \end{bmatrix} \qquad (3.15)$$

and once again s is the propagation distance from O to P. The divergence factor (DF) of (3.3) can now be found using (3.4) thru (3.6).

To find the curvature matrices associated with reflection from a curved surface, refer to Figure 36. $\hat{N}$ is the unit surface normal and the reflected ray obeys Snell's law of reflection, i.e., $\theta_i = \theta_r$ and the incident and reflected rays lie in the same

75

plane. The electric field at a point P can be written similarly to (3.3) as

$$\vec{E}(P) = (DF) \cdot \overline{\overline{\Gamma}} \cdot \vec{E}(O^-)e^{-jks} \qquad (3.16)$$

where

$$\vec{E}(O^-) = \text{electric field immediately before reflection,}$$

$$\overline{\overline{\Gamma}} = \text{dyadic plane wave reflection coefficient.}$$

The divergence factor (DF) is again given by (3.4) and (3.5) with the principal radii of curvature R_1 and R_2 given by (3.6). The dyadic plane wave reflection coefficient $\overline{\overline{\Gamma}}$ relates the polarization components of the incident and reflected electric fields. Because of the localized nature of high frequency fields, it is assumed that this dyadic reflection coefficient is the same as for the case of a plane wave incident on a planar interface of the same material.

Using (3.14), the curvature matrix at P is given in terms of the matrix at O^+ by

$$\overline{\overline{Q}}(P) = \left\{ \left[\overline{\overline{Q}}(O^+) \right]^{-1} + s\overline{\overline{I}} \right\}^{-1} \qquad (3.17)$$

where

$$\overline{\overline{Q}}(O^+) = \text{curvature matrix just after reflection.}$$

Referring to Figure 37, the reflected curvature matrix $\overline{\overline{Q}}(O^+)$ is related to the incident curvature matrix $\overline{\overline{Q}}(O^-)$ by the relation

$$\left(\overline{\overline{P}}_i \right)^T \overline{\overline{Q}}(O^-)\overline{\overline{P}}_i + 2p_{33}\overline{\overline{Q}}_S = \left(\overline{\overline{P}}_r \right)^T \overline{\overline{Q}}(O^+)\overline{\overline{P}}_r \qquad (3.18)$$

where

$$\overline{\overline{P}}_{i,r} = \begin{bmatrix} \hat{x}_1^{i,r} \cdot \hat{x}_1 & \hat{x}_1^{i,r} \cdot \hat{x}_2 \\ \hat{x}_2^{i,r} \cdot \hat{x}_1 & \hat{x}_2^{i,r} \cdot \hat{x}_2 \end{bmatrix} \qquad (3.19)$$

76
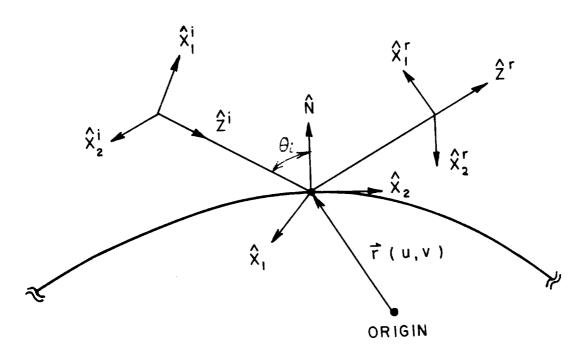
Figure 37: Coordinate systems of the surface and the incident and reflected rays.

$$p_{33} = \hat{z}^i \cdot \hat{N} \qquad (3.20)$$

$$\left(\overline{\overline{P}}_{i,r}\right)^T = \text{transpose of } \overline{\overline{P}}_{i,r},$$

$$\overline{\overline{Q}}_S = \text{curvature matrix of the reflecting surface at } O.$$

$\overline{\overline{Q}}_S$ is found using (3.10) thru (3.13) and the coordinate vectors of the incident and reflected rays and the surface are shown in Figure 37. For the purpose of tracing a ray through multiple reflections inside a cavity, the following choices for the reflected wavefront and surface orthogonal coordinates are often used for convenience [17]:

Curved surface: $\begin{cases} \hat{x}_1 = \hat{r}_u \\ \hat{x}_2 = \hat{N} \times \hat{x}_1 = \hat{r}_v \end{cases}$ $\qquad (3.21)$

Reflected wavefront: $\begin{cases} \hat{x}_1^r = \hat{N} \times \hat{z}^r / \sin\theta_i \\ \hat{x}_2^r = \hat{z}^r \times \hat{x}_1^r \end{cases}$ $\qquad (3.22)$

77

where

$$\hat{r}_u \;\; = \;\; \text{unit vector in the direction of } \partial\vec{r}/\partial u,$$

$$\hat{r}_v \;\; = \;\; \text{unit vector in the direction of } \partial\vec{r}/\partial v.$$

In other words, the surface coordinate vectors $\hat{x}_1$ and $\hat{x}_2$ are derived from $\vec{r}_u$, and the reflected wavefront coordinate vectors $\hat{x}_1^r$ and $\hat{x}_2^r$ are perpendicular and parallel to the plane of incidence, respectively. The incident coordinate vectors $\hat{x}_1^i$, $\hat{x}_2^i$ and $\hat{z}^i$ are known a priori and $\hat{z}^r$ is found from $\hat{z}^i$ using Snell's law. The reflected coordinate vectors will become the new incident coordinate vectors for the next reflection, and so on.

For the very first reflection, i.e., when a ray-tube of the incident plane wave field first strikes a cavity wall, the incident wavefront curvature matrix is a zero matrix, as in (3.9), representing a planar wavefront. A convenient choice of incident coordinate vectors for this first reflection is (referring again to Figure 37)

$$\text{Incident wavefront, first reflection:} \quad \begin{cases} \hat{x}_1^i \;\; = \;\; \hat{x}_1^r \\[2mm] \hat{x}_2^i \;\; = \;\; \hat{z}^i \times \hat{x}_1^i \end{cases} \tag{3.23}$$

where $\hat{x}_1^r$ is given in (3.22).

3.2 Exterior Field Scattered by the Interior Termination Using GO Based Equivalent Sources

As mentioned earlier, to obtain the fields scattered by the interior cavity termination using the GO method, one of two integral methods are used. The first of these is an integration over the aperture at the open end and it is referred to as GO/AI; the second is based on the use of a generalized reciprocity integral over an aperture surface defined conveniently in the vicinity of the termination and it is referred to as GO/RI. Thus, the main difference between the two is that in the

78

GO/AI method, the ray-tubes are traced from the open end to the termination and back to the aperture at the open end where they are integrated, while in the GO/RI method they are traced only from the open end to some waveguide cavity cross-section before but near the termination of the cavity where they are "reacted" (in the form of a generalized reciprocity integral) with all the other ray-tubes and integrated. However, in general, the GO/RI method also requires the use of an aperture integration because some ray-tubes may never reach the termination but will exit through the open end. The main advantage of the GO/RI over the GO/AI method is that complex terminations can be included which GO alone could not handle, provided there is some other means of characterizing the EM reflections from the termination.

3.2.1 GO combined with an aperture integration (GO/AI).

Once again, as in the hybrid modal method of Chapter II, the scattering from an open-ended waveguide cavity will be restricted to the scattering by the rim at the open end and the scattering by the interior termination. No other external scattering mechanisms are included. The total scattered field with this restriction can then be written as

$$\vec{E}^s \;=\; \vec{E}^{sr} + \vec{E}^{sc} \tag{3.24}$$

.

where

$\vec{E}^{sr}$ = field scattered by the rim alone,

$\vec{E}^{sc}$ = field scattered by the interior of the cavity.

In Chapter II, the incident plane wave field $\vec{E}^i$ is given by (2.1) and the rim scattered field $\vec{E}^{sr}$ is given by (2.21) thru (2.24) and will not be repeated here.

79
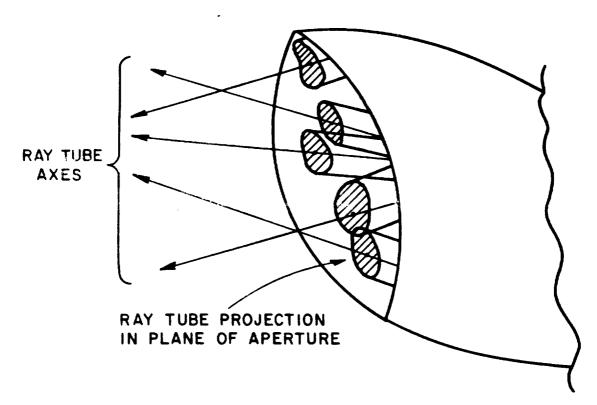
Figure 38: Projections of ray-tubes in the open end as they exit the cavity.

The cavity scattered field $\vec{E}^{sc}$ is due to ray-tubes incident at the open end which have been traced inside the cavity via interior wall reflections and the termination until they exit through the open end. This method requires that one know how the ray tubes reflect from the termination; clearly the GO/AI (or SBR) method can accomodate only simple terminations, e.g., a planar reflecting surface. When the ray-tubes exit through the open end after reflecting from the termination, their cross-sectional shapes and areas have changed and their projections in the plane of the aperture at the open end form discrete patches or footprints where their fields exist, as shown in Figure 38. Hence, an aperture integration over these patches is necessary to obtain a continuous scattered field from a discontinuous, rapidly varying aperture field distribution obtained via GO ray tracing.

The cavity scattered field can be written as a sum of contributions from all
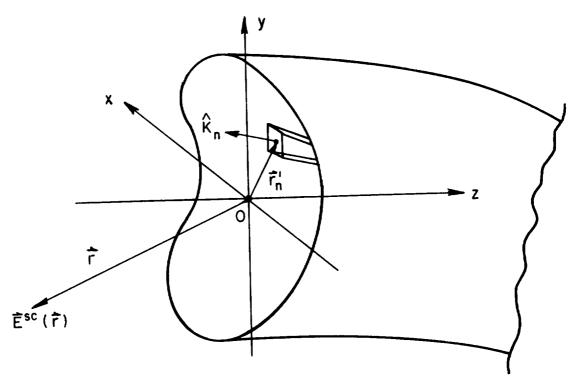
Figure 39: n^{th} ray-tube exiting through the open end of a cavity.

the ray-tubes which exit through the open end as

$$\vec{E}^{sc} = \sum_{n=1}^{N} \vec{E}_n^{sc} \qquad (3.25)$$

where

$\vec{E}_n^{sc}$ = field "radiated" by the equivalent (Kirchhoff or PO based)

sources corresponding to the fields of the nth GO ray-tube in the

aperture at the open end.

Figure 39 shows the nth ray-tube and its projection in the open end. As shown in Appendix B Equation (B.11), the far field radiated by the equivalent sources in the Kirchhoff approximation for the aperture radiation integral is given by

$$\vec{E}_n^{sc} = -[\hat{r} \times \hat{p}_{hn} + \hat{r} \times (\hat{r} \times \hat{p}_{en})] \frac{jk}{4\pi} \frac{e^{-jkr}}{r} E_{no} e^{jk\vec{r}_n'\cdot\hat{r}} A_n S_n(\hat{r})$$

where

$\vec{r}$ $=$ vector from the origin to the receiver point,

$\hat{p}_{en}$ $=$ unit polarization vector of the electric field of the nth ray-tube in the open end,

$\hat{p}_{hn}$ $=$ unit polarization vector of the magnetic field of the nth ray-tube in the open end,

$=$ $\hat{k}_n \times \hat{p}_{en}$

$\hat{k}_n$ $=$ unit vector in the direction of propagation of the nth ray-tube,

$=$ $\hat{z}_n$

E_{no} $=$ scalar portion of the electric field of the nth ray-tube in the open end,

A_n $=$ cross-sectional area of the nth ray-tube in the open end,

$\vec{r}_n'$ $=$ vector from the origin to the intersection of the central ray of the nth ray-tube with the open end.

The form of (3.26) is that of a spherical wave, originating at the point where the central ray of the ray-tube intersects the open end, whose pattern is determined by the normalized shape function $S_n(\hat{r})$ [17,18] which is given by

$$S_n(\hat{r}) \;=\; \frac{1}{A_n} \int\!\!\int_{A_n} e^{jk\vec{r}\,'\cdot\hat{r}} dS' \qquad (3.27)$$

with the relative geometry of the nth ray-tube in the open end shown in Figure 40, and

$\vec{r}\,'$ $=$ vector from origin to a source point in the coordinate system of
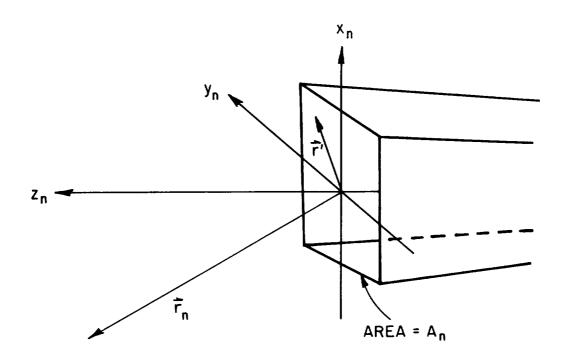
Figure 40: Relative coordinate system and geometry of the nth ray-tube in the open end.

the nth ray-tube,

$\hat{r}$ = unit vector in direction of observer.

The integration is over $\vec{r}\,'$ in the x_n-y_n plane within the cross-section of the nth ray-tube where it intersects the open end. Integrating over the cross-section of the ray-tube is easier to perform than integrating over the oblique projection of the ray-tube in the open end.

The shape function of (3.27) is actually a two-dimensional Fourier transform of the shape of the cross-section of the nth ray-tube, and can thus be found for an arbitrary polygonal shape [17]. For example, if the cross-section is a square with its sides parallel to the x_n and y_n axes, the shape function is given by

$$S_n(\hat{r}) = \text{sinc}\left(\frac{1}{2}k\sqrt{A_n}\cos\phi_n\sin\theta_n\right)\text{sinc}\left(\frac{1}{2}k\sqrt{A_n}\sin\phi_n\sin\theta_n\right)$$

$$(3.28)$$

83

where

$$\text{sinc}(x) \;=\; \frac{\sin x}{x} \tag{3.29}$$

$\theta_n, \phi_n \;=\;$ angular coordinates of the observer in the coordinate system

of the nth ray-tube,

as shown in Appendix B. If the cross-section is circular, then [18]

$$S_n(\hat{r}) \;=\; \frac{2J_1(u)}{u} \tag{3.30}$$

where

$$
\begin{aligned}
u \;&=\; k\sqrt{\frac{A_n}{\pi}}\,\sin\theta_n \\
&=\; k\sqrt{\frac{A_n}{\pi}}\,\sin\left(\cos^{-1}\hat{r}\cdot\hat{k}_n\right)
\end{aligned} \tag{3.31}
$$

$J_1(u) \;=\;$ the first order Bessel function of the first kind.

However, as mentioned earlier in Section 3.1.1, if the cross-sectional area A_n of the ray-tube is less than $\left(\frac{1}{2}\lambda\right)^2$, the exact shape of the ray-tube can be assumed arbitrary in the calculation of the shape function, provided that the ray-tube is roughly symmetric about its central ray. The radiation pattern determined by the shape function for such cases will be symmetric about the z_n axis and depend only on the cross-sectional area and θ_n. This is demonstrated in Appendix B for the case of a cross-section which is approximately square. The shape function for this case becomes, from (B.19) and (B.26)

$$
\begin{aligned}
S_n(\hat{r}) \;&=\; \text{sinc}\left(\frac{1}{2}k\sqrt{A_n}\,\sin\theta_n\right) \\
&=\; \text{sinc}\left(\frac{1}{2}k\sqrt{A_n}\,\left|\hat{r}\times\hat{k}_n\right|\right)
\end{aligned} \tag{3.32}
$$

which is rotationally symmetric as desired. If the pattern of the ray-tube is shape independent, then the expressions of (3.30) and (3.32) should be very nearly the

same for $\sqrt{A_n} < \frac{1}{2}\lambda$. This is shown in Appendix B by comparing the quadratic portions of the Taylor series expansions of the two shape functions for small argument. Thus, (3.30) becomes

$$\frac{2J_1\left(k\sqrt{\frac{A_n}{\pi}}\sin\theta_n\right)}{k\sqrt{\frac{A_n}{\pi}}\sin\theta_n} \approx 1 - \frac{1}{8\pi}\left(k\sqrt{A_n}\sin\theta_n\right)^2 \tag{3.33}$$

and (3.32) becomes

$$\text{sinc}\left(\frac{1}{2}k\sqrt{A_n}\sin\theta_n\right) \approx 1 - \frac{1}{24}\left(k\sqrt{A_n}\sin\theta_n\right)^2 \tag{3.34}$$

which are nearly identical for practical purposes.

In summary, the recommended method of using GO/AI is to choose a dense enough grid of ray-tubes for the incident plane wave field which enters into the cavity at the open end, such that the ray-tubes exit the cavity with a cross-sectional area less than $\left(\frac{1}{2}\lambda\right)^2$. The central ray of each ray-tube is then traced via GO as described in Section 3.1.2 to obtain the field $\vec{E}_{no}$ in the cross-section of the ray-tube where it exits through the open end. The cavity scattered field is then given by (3.25) and (3.26) along with (3.30) or (3.32). Using (3.2) the cross-sectional area of the nth ray-tube in the open end is

$$A_n = \frac{\left|\vec{E}^i\right|^2}{\left|\vec{E}_{no}^{ll}\right|^2}A_{in} \tag{3.35}$$

where

$\vec{E}_{no}^{ll}$ = electric field of the nth ray-tube in the open end assuming no loss,

A_{in} = initial area of the ray-tube when it was launched.

Since it is not usually known a priori what the cross-sectional area of ray-tubes will be when they exit, it is difficult to know just how dense to make the initial

grid of ray-tubes upon entry. They should, of course be less than $\left(\frac{1}{2}\lambda\right)^2$ in cross-section, but because of divergence effects, this area tends to grow the farther the ray-tubes must travel and the more reflections from curved surfaces they undergo. One solution is to launch denser and denser grids of ray-tubes by trial and error until they are all sufficiently small when they exit. However, it is usually much more efficient to use an algorithm which sub-divides a ray-tube which is too large when it exits into smaller ray-tubes. These new ray-tubes are re-launched and the process is repeated. This procedure is more efficient than to make all the ray-tubes in the grid smaller just because one ray-tube came out too large.

3.2.2 GO combined with the termination reciprocity integral (GO/RI).

The termination reciprocity integral is formulated in Appendix C for the general case of an open-ended waveguide cavity illuminated by two electric current point sources of strengths $\vec{p}$ and $\vec{p}\,'$, as shown in Figures 95 and 97. The source $\vec{p}$ is located at a point P and $\vec{p}\,'$ is located at P'. The termination reciprocity integral given by (C.15) is formulated for this general case as

$$\vec{E}'_s(P) \cdot \vec{p} \;=\; -\int\int_{S_t} \left(\vec{E}_i \times \vec{H}'_s - \vec{E}'_s \times \vec{H}_i\right) \cdot \hat{n}\,dS \qquad (3.36)$$

where

$\vec{E}'_s(P)$ = electric field at P scattered by the termination of the cavity

when it is excited by an electric current point source

of strength $\vec{p}\,'$ at P',

$\vec{E}_i, \vec{H}_i$ = fields due to $\vec{p}$ in the absence of the termination but in the

presence of the semi-infinite waveguide cavity,

$\vec{E}'_s, \vec{H}'_s$ = fields due to $\vec{p}\,'$ scattered by the termination in the presence

of the semi-infinite waveguide,

$$S_t \;=\; \text{a cross-sectional surface chosen conveniently in front of the}$$
$$\text{termination,}$$

$$\hat{n} \;=\; \text{unit surface normal of } S_t \text{ pointing away from the termination.}$$

Throughout this section, a primed quantity means that it is associated with the source at P' and a corresponding unprimed quantity means that is associated with the source at P. By an appropriate choice of $\vec{p}$, any component of the scattered field can be extracted using (3.36). For example,

$$
\begin{aligned}
E'_{sx}(P) \;&=\; \hat{x} \text{ component of } \vec{E}'_s(P) \\
&=\; \vec{E}'_s(P) \cdot \hat{x} \\
&=\; \vec{E}'_s(P) \cdot \vec{p} \,\big|_{\vec{p}=\hat{x}} .
\end{aligned}
\tag{3.37}
$$

What (3.36) and (3.37) imply is that the field at P which was scattered by the termination due to fields from the current element at P' can be found by tracking the fields from both $\vec{p}$ and $\vec{p}\,'$ inside the cavity to the cross-section S_t and integrating as in (3.36). Therefore, the fields do not have to be tracked back out of the cavity as is necessary in the GO/AI approach. The fields from $\vec{p}$ at S_t are in the absence of the termination and the fields from $\vec{p}\,'$ are in the presence of the termination. It is noted that (3.36) includes all multiple wave interactions between the termination, the open end and any other scattering centers; however, these effects are generally not significant if the interior reflection by the termination is substantially bigger than the interior reflection of waves from the open end and can therefore be neglected. The latter situation which is of interest here is also true if the cavity walls are coated with a layer of absorbing material. It is assumed that the above conditions are met in the present study; hence, these multiple wave

interaction contributions to $\vec{E}'_s, \vec{H}'_s$ can be ignored here. Since the fields in (3.36) are computed approximately by GO ray tracing, the result in (3.36) is approximate even to first order. It is important to note that the exact form of (3.36) does not include the effects of waves which experience reflections from the interior cavity region without reaching the termination plane S_t; however, this contribution can be significant when it exists (as in tapered waveguides for example) and it must be added separately. The latter contribution when it exists can be found easily within the GO approximation by using the aperture integration method of Section 3.2.1, applied only to those ray-tubes which exit from the open end without reaching the termination. Also, (3.36) does not include any external scattering such as that due to the rim at the open end, but this can be added separately as was done for the rim in Section 3.2.1.

To use the termination reciprocity integral of (3.36) with the GO method, the point sources at P and P' must be moved to infinity so that their fields incident on the cavity are plane waves. As noted in Appendix C, the plane wave fields of an electric point source $\vec{p}$ are given by

$$\vec{E}_{\vec{p}}(\vec{R}) = \vec{E}_o e^{-jkR} \tag{3.38}$$

$$\vec{H}_{\vec{p}}(\vec{R}) = \frac{1}{Z_o} \hat{R} \times \vec{E}_o e^{-jkR} \tag{3.39}$$

where

$$\vec{E}_o = \lim_{R \to \infty} -\hat{R} \times \hat{R} \times \vec{p} \frac{jkZ_o}{4\pi R} \tag{3.40}$$

$$\vec{R} = \text{vector from current element to receiver.}$$

Also as noted in Appendix C, the bistatic radar cross-section (RCS), or the "echo area", for the co-polarized and cross-polarized fields, respectively, are most often

88

the figures of interest. In terms of $\hat{\theta}$ and $\hat{\phi}$ polarizations, the two co-polarized echo widths are $\sigma_{\theta\theta}$ and $\sigma_{\phi\phi}$ and the two cross-polarized echo widths are $\sigma_{\theta\phi}$ and $\sigma_{\phi\theta}$. The first subscript denotes the polarization of the receiver at P and the second subscript denotes the polarization of the source at P'. For example, $\sigma_{\theta\phi}$ is defined as in (C.31) by

$$\sigma_{\theta\phi} = \lim_{r \to \infty} 4\pi r^2 \frac{\left|E'_{s\theta}(P)\right|^2}{\left|E'_{o\phi}\right|^2} \tag{3.41}$$

where

$$E'_{s\theta}(P) = \left. \vec{E}'_s(P) \cdot \vec{p} \right|_{\vec{p}=\hat{\theta}} \tag{3.42}$$

$\quad E'_{o\phi} = \hat{\phi}$ component of the plane wave field incident on the cavity

$\qquad$ from the direction of P',

$\quad r = $ distance from the open end of the cavity to P and P'.

As shown in Appendix C, (3.41) can be written as

$$\sigma_{\theta\phi} = \frac{(kZ_o)^2}{4\pi} \frac{\left|E'_{s\theta}(P)\right|^2}{|E_{o\theta}|^2 \left|E'_{o\phi}\right|^2} \tag{3.43}$$

where

$\quad E_{o\theta} = \hat{\theta}$ component of the plane wave field incident on the cavity from

$\qquad$ the direction of P,

which is a much easier form to use computationally. The other three bistatic RCS components are found using this same equation with the appropriate interchanges of θ and ϕ.

It remains to compute (3.36) using the fields at S_t which have been found using the GO ray tracing method of this chapter. Because it is not a simple matter to do

89

the integral using the ray-tube fields themselves and because it is not easy to find $\vec{E}'_s$ and $\vec{H}'_s$ of (3.36) for complex terminations, it is usually necessary to transform the GO fields incident on S_t into some regular expansion such as a modal or plane wave expansion. Other transformations have been suggested such as a Gaussian beam expansion or a simple point matching scheme, but so far only the modal expansion has been investigated in any depth and so only it will be described here. Whatever the transformation, it is assumed that the fields reflected from the termination can be found in terms of the new expansion. In the case of the modal expansion, the modal reflection matrix $[S_\Gamma]$ described in Chapter II must be known.

To use the modal form of the termination reciprocity integral, it is necessary that the region near the termination be a separable waveguide section for which the waveguide modal fields are known. For example, the region near the termination in Figure 95 is a circular waveguide. Then the fields in this circular waveguide region can be expanded as a sum of waveguide modes as in Chapter II and appendix Section C.2. As shown in Appendix C, the modal form of (3.36) is given by

$$\vec{E}'_s(P) \cdot \vec{p} = -2 \sum_{m=1}^{M} A_m^+ A_m^{-\prime} \tag{3.44}$$

where

$$A_m^+ = \int\!\!\int_{S_t} \left(\hat{e}_{mt} \times \vec{H}_i \right) \cdot \hat{\eta} dS \tag{3.45}$$

$$A_m^{+\prime} = \int\!\!\int_{S_t} \left(\hat{e}_{mt} \times \vec{H}'_i \right) \cdot \hat{\eta} dS \tag{3.46}$$

$$[A^{-\prime}] = [S_\Gamma][A^{+\prime}] \tag{3.47}$$

and

$$\vec{H}_i, \vec{H}'_i = \text{magnetic fields incident on } S_t \text{ from } P \text{ and } P', \text{ respectively,}$$

90

$$\hat{e}_{mt} = \text{transverse component of the electric field of the } m^{th} \text{ waveguide}$$

mode,

M = number of included waveguide modes,

$\hat{\eta}$ = waveguide axial coordinate unit vector pointing towards the interior termination.

It is assumed that $\eta = 0$ is chosen to coincide with S_t. $[A^{-\prime}]$ and $[A^{+\prime}]$ are column matrices containing the M modal coefficients $A_m^{+\prime}$ and $A_m^{-\prime}$, respectively, and $[S_\Gamma]$ is the termination modal reflection matrix of order $M \times M$ which relates the incident modal coefficients to the reflected coefficients, referenced at the cross-section S_t (i.e, at $\eta = 0$). Equation (3.44) can now be used to evaluate the scattered field component as in (3.37) or (3.42).

The modal coefficients of (3.45) and (3.46) can be found in terms of the ray-tubes which are incident on S_t. These can now be written as a sum of integrals over the ray-tubes at S_t:

$$A_m^+ = \sum_{q=1}^{Q} \int\int_{S_q} \left(\hat{e}_{mt} \times \vec{H}_{iq} \right) \cdot \hat{\eta} dS \tag{3.48}$$

$$A_m^{+\prime} = \sum_{q'=1}^{Q'} \int\int_{S_{q'}} \left(\hat{e}_{mt} \times \vec{H}'_{iq'} \right) \cdot \hat{\eta} dS \tag{3.49}$$

where

$S_q, S_{q'}$ = projection of the qth or $q'^{\ th}$ ray-tube on S_t,

$\vec{H}_{iq}, \vec{H}'_{iq'}$ = magnetic field of the qth or $q'^{\ th}$ ray-tube incident on S_t,

Q, Q' = number of ray-tubes which reach the cross-section S_t

from P or P'.

Once again, the primed quantities are associated with the point source at P' and the corresponding unprimed quantities are associated with the point source at P.

91

The area of the projections of the ray-tubes on S_t are related to the cross-sectional areas of the ray-tubes by

$$S_q = \frac{A_q}{\left| \hat{k}_q \cdot \hat{\eta} \right|} \qquad (3.50)$$

where

A_q = cross-sectional area of the qth ray-tube,

$\hat{k}_q$ = unit vector in the direction of propagation of the central ray of the qth ray-tube,

and similarly for $S_{q'}$ and $A_{q'}$. The fields $\vec{H}_{iq}$ and $\vec{H}'_{iq'}$ can be found easily from the field of the central ray of a ray-tube because the field inside a ray-tube is assumed to be constant at any given cross-section. The field of a central ray is found by launching a ray-tube as described in Section 3.1.1 and by ray tracing it as described in Section 3.1.2.

As mentioned before, it is expected that if the cross-sectional area of a ray-tube is less than $\left(\frac{1}{2}\lambda \right)^2$, then the exact shape of the ray-tube about its axis is not important in the integral so that any convenient shape may chosen, as long as the area stays the same. For example, if the integration is in the x-y plane then the projection would be chosen to be a square with sides of length $\sqrt{S_q}$ parallel to the x and y axes. This makes the integrals in (3.48) and (3.49) much easier to evaluate numerically.

3.3 Numerical Results and Discussion of the Geometrical Optics Methods
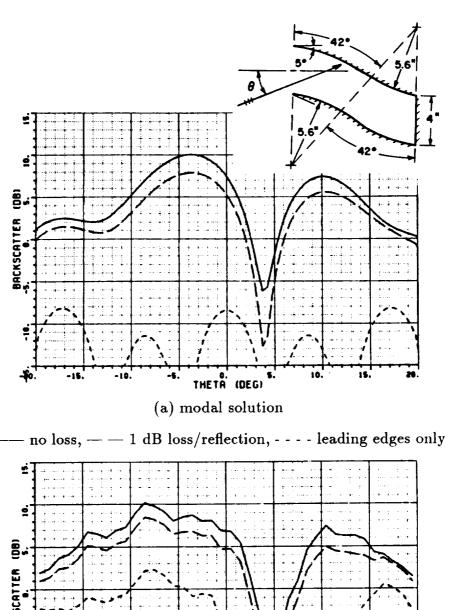
In this section numerical results obtained using the GO method will be presented and in most cases will be compared with more accurate modal reference

solutions. All of the plots of this section are taken from sources listed in the references and these sources will be cited as the results are presented.
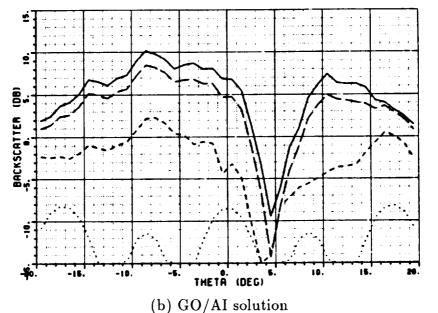
In [7], the scattering from 2-D straight and S-shaped cavities with planar short circuit terminations and absorber coatings on the inner walls was analyzed using the hybrid modal method of Chapter II and the GO/AI method of this chapter. It was found that the GO/AI method could predict the general trends of the backscatter pattern when compared with the modal reference solution, but often failed to depict accurately the details of the lobe structure such as locations of peaks and nulls. This has often been seen in other work which used the GO method, such as in [14], [16] and [17]. However, the GO method is useful in many practical applications which do not require as much accuracy in the pattern details and in applications where other methods, such as the hybrid modal method, can not be used due to non-uniform geometries and arbitrary absorber treatments. Figure 41 shows a typical backscatter vs. aspect angle result from [7], comparing results obtained using the hybrid modal perturbation method and the GO/AI method applied to a shallow S-shaped cavity. The modal result shows plots for the lossless case and for the 1 dB loss/reflection absorber coated case, while the GO/AI result shows these two plots plus one for the 5 dB loss/reflection case. Both show the scattering by just the leading edges of the cavity. It is noted that the modal perturbation technique could not handle the higher loss case. As the figure shows, the GO/AI solution agrees fairly well for this shallow cavity, which is generally the case. However, as the length of the cavity increases, the GO/AI result gets worse because the actual fields in the cavity diverge more due to diffraction effects, which the GO field does not include. Also, because of ray divergence effects, the longer the cavity is the more rays need to be traced, thus decreasing the efficiency of the method.

93

In [16], the GO/AI method, there referred to as the shooting and bouncing rays (SBR) method, was applied to open-ended waveguide cavities with planar terminations which were modelled mathematically using transitions between geometric shapes along with axis-shifting lofting functions. An example of such a cavity would be one which starts out with a square cross-section at the open end that slowly becomes circular by the region near the termination, and a lofting function is used to bend the axis of the cavity into an S-shape. Figure 42 shows a typical RCS vs. aspect angle result from [16] for an open-ended circular cylinder with a planar termination, found using SBR and compared with a modal result. The agreement is good in terms of the general trends of the pattern, but not as good in terms of detailed lobe structure, as was discussed above.

Figure 43 and 44 show typical bistatic scattering (BCS) vs. observation angle results from [16] for two geometric transition/lofted S-shaped cavities. Since there is no modal reference solution available for such general configurations, the plots show only the SBR result and illustrate the convergence of the solution in terms of ray density. In general it was found in [16] that the ray density needed to be approximately 15 to 20 rays per wavelength for convergence of the solutions for the geometries considered.
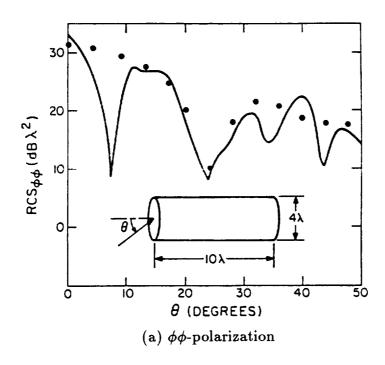
Figure 45 shows an RCS vs. aspect angle result from [16] for a triangle-to-circle cavity, with and without offset and with and without absorber coating. As the figure shows, the offsetting the termination reduces the RCS somewhat compared to the non-offset case, and the absorber combined with the offset reduces the RCS quite significantly.

94

(a) modal solution

—— no loss, — — 1 dB loss/reflection, - - - - leading edges only

(b) GO/AI solution

—— no loss, — — 1 dB loss/reflection, - - - - 5 dB loss/reflection,

· · · · · · leading edges only

Figure 41: Backscatter from a 2-D S-shaped cavity with a short circuit termination and absorber coated walls, ⊥ polarization and 10 GHz.

(a) $\phi\phi$-polarization

(b) $\theta\theta$-polarization
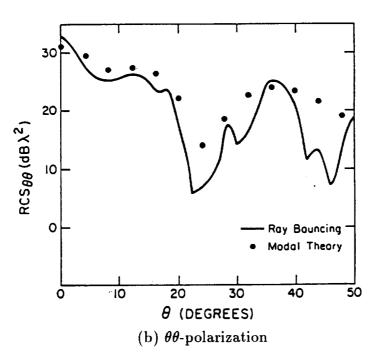
Figure 42: Backscatter patterns of a circular cylinder (tin can), comparing the SBR solution with a modal reference solution.

(a) $\phi\phi$-polarization

(b) $\theta\theta$-polarization
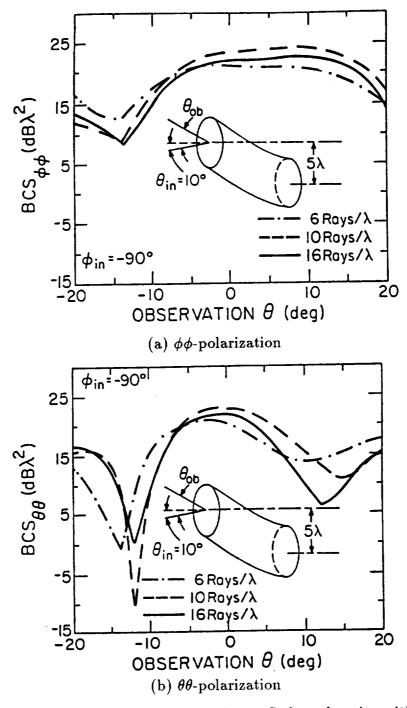
Figure 43: Bistatic scattering patterns for an S-shaped cavity with a circular cross-section showing convergence in ray density. Diameter= 5λ, depth= 10λ. Direction of incidence: $(\theta_{in}, \phi_{in}) = (10°, -90°)$

(a) $\phi\phi$-polarization

(b) $\theta\theta$-polarization
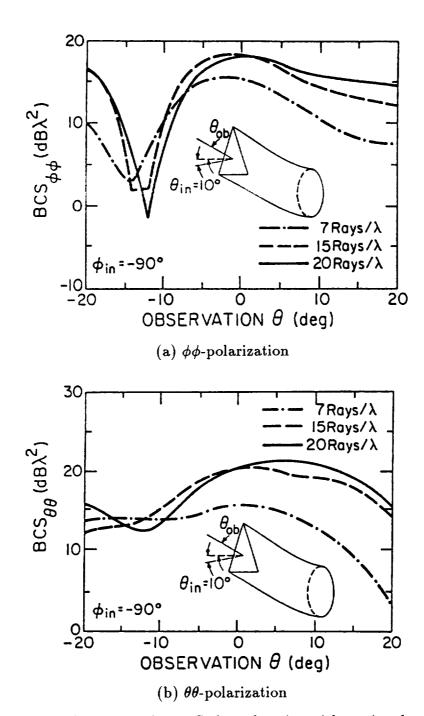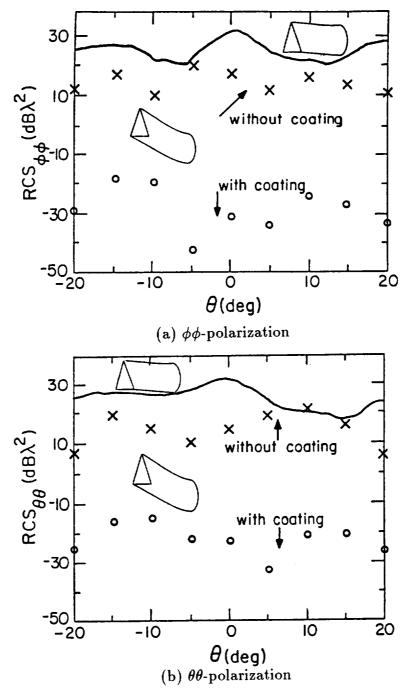
Figure 44: BSC patterns for an S-shaped cavity with a triangle-to-circle cross-section transition, showing convergence in ray density. Triangle is 5.4λ on a side, diameter of end circle is 4.5λ, depth is 6.75λ and the offset is 4.05λ. Direction of incidence: $(\theta_{in}, \phi_{in}) = (10°, -90°)$

(a) $\phi\phi$-polarization

(b) $\theta\theta$-polarization

— no offset, no coating, × with offset, no coating, ○ with offset, with coating

Figure 45: RCS patterns for a cavity with a triangle-to-circle cross-section transition, with and without offset and with and without absorber coating. Dimensions are the same as in Figure 44. Coating: thickness=0.1λ, $\epsilon_r = 2.5 - j1.25$, $\mu_r = 1.6 - j0.8$.

CHAPTER IV

THE GAUSSIAN BEAM SHOOTING METHOD

In this chapter, the scattering from the interior of relatively arbitrary open-ended waveguide cavities with smoothly curved interior walls is analyzed using a Gaussian Beam (GB) expansion of the incident plane wave fields at the open end. The cavities under consideration may contain perfectly-conducting interior cavity walls with or without a thin layer of material coating, or the walls may be characterized by an impedance boundary condition. As before, the scattering by external features of the cavity, such as by the rim at the open end, must be added separately to the scattering from the interior of the cavity; again only the rim scattering will be included here. The termination of the cavity may be arbitrarily complex as long the scattering properties are known in some manner, such as via a modal reflection matrix or a plane wave spectral expansion.

In the GB shooting method, the incident field in the open end of the cavity is expanded in terms of an array of shifted and rotated Gaussian beams. At optical wavelengths, an example of a well known type of Gaussian beam is a laser beam. At microwave frequencies, GB's are typically much wider and diverge faster than laser beams, but their basic functional form is the same. These GB's are allowed to propagate inside the cavity, reflecting off the cavity walls. If the GB's are well focussed, it is assumed then that they can be tracked within the interior waveguide cavity region only along the axis of the beam in a manner similar to geometrical

optics (GO) ray tracing. The reflection of a GB from a curved wall is subsequently found in this axial beam tracking approximation by assuming that an incident GB gives rise to a reflected GB with parameters related to the incident beam and the radius of curvature of the wall. It is found that this approximation breaks down for GB's which come close to grazing a convex surface and when the width of the incident beam is comparable to the radius of curvature of the surface. An important and useful feature of this GB approach is that the expansion of the fields in the open end depend on the incidence angle only through the expansion coefficients, so the GB's need to be tracked through the waveguide cavity only once for a wide range of incidence angles. Furthermore, the GB's are tracked only to the vicinity of the interior termination from the open end where they are launched as they propagate via reflections off the interior cavity walls. It is not necessary to track another set of beams from the termination back to the open end to find the fields scattered into the exterior by the termination because the use of a generalized reciprocity theorem allows one to do so with the information available from tracking the fields only one way (from the open end to the termination). At the termination, the sum of all the GB's are integrated using the termination reciprocity integral described in Appendix C to give the fields scattered from the interior of the cavity.

Results are compared with solutions based on the hybrid asymptotic modal method. The agreement is found to be very good for cavities made up of planar surfaces, and for cavities which are not too long with respect to their width with curved surfaces. General rules of thumb for choosing the proper GB expansion parameters and length to width ratios of cavities for which the method should be accurate are presented. It is noted once again that the scattering from external features of the cavity (other than the open end) are not of interest here and are

101

thus ignored, as was done in Chapters I and II. While the development is presented here for the 2-D case, it can be directly extended to treat the 3-D case in a straightforward manner.

The analysis in this chapter is for the two dimensional (2-D) plane wave bistatic scattering case. Therefore, the two possible polarizations are perpendicular ($\perp$) polarization in which the electric (E) field is normal to the plane of the geometry, and parallel ($\parallel$) polarization in which the magnetic (H) field is normal to the plane of the geometry. Throughout, the letter U will be used to represent either the E-field or the H-field, depending on polarization, perpendicular or parallel, respectively. Also, U represents the scalar portion of $\vec{U}$.

Section 4.1 will formulate the problem in terms of scattering by the open end, found using GTD, and scattering by the termination, found using the termination reciprocity integral of Appendix C. Section 4.2 will derive the Gaussian beam basis function and discuss some of its properties. Section 4.3 will describe the GB expansion of the fields in the open end of the cavity by treating the transmission through an aperture in free space, and Section 4.4 will discuss how the GB's are tracked inside the cavity to the termination. Numerical results will then be presented in Section 4.5.

4.1 Formulation of the Gaussian Beam Shooting Method

The contributions to the scattering from an open-ended waveguide cavity which are of primary interest in this work consist of the following components: the external scattering by the edges at the open end, and the internal scattering due to incident energy which is coupled to the interior of the cavity, then reflected by the termination and re-radiated back into the exterior via the open end. All other external scattering effects from the structure in which the cavity is enclosed

102
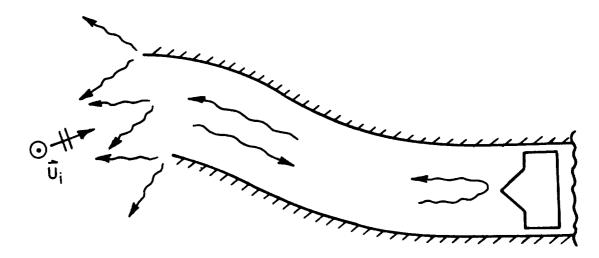
Figure 46: Scattering mechanisms of a 2-D open-ended waveguide cavity.

are not of interest here and are therefore not included in this analysis. Figure 46 shows a general two dimensional (2-D) cavity geometry which illustrates the scattering mechanisms of interest. The scattered field can then be written as a sum of these two scattering components as

$$\vec{U}^s = \vec{U}^{sr} + \vec{U}^{sc} \qquad (4.1)$$

where

$$\vec{U}^{sr} = \text{rim scattering component},$$

$$\vec{U}^{sc} = \text{interior cavity scattering component}.$$

The plane wave field scattered by the edge at the open end of the cavity can be found easily using the geometrical theory of diffraction (GTD) [1]. The scattered field for this case is given to first order as (see [7])

$$\vec{U}^{sr} = \hat{z} U_i \frac{e^{-jk\rho}}{\sqrt{\rho}} \left[D_{s,h}(\pi + \theta_s, \pi + \theta_i) e^{j\frac{1}{2}kd(\sin\theta_s + \sin\theta_i)} \right.$$
$$\left. + D_{s,h}(\pi - \theta_s, \pi - \theta_i) e^{-j\frac{1}{2}kd(\sin\theta_s + \sin\theta_i)} \right] \qquad (4.2)$$
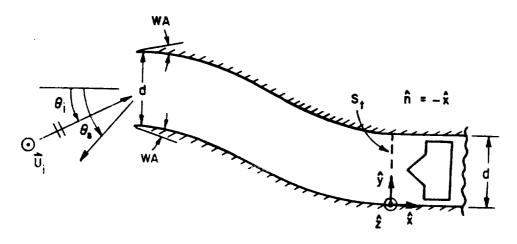
Figure 47: Geometry of a 2-D open-ended waveguide cavity.

where

U_i = magnitude of the incident plane wave,

θ_i = incidence angle,

θ_s = observation angle,

ρ = distance to the receiver from the center of the open end,

d = width of the open end.

The geometry is shown in Figure 47, with $\hat{z}$ normal to the page. (4.2) is phased referenced to the center of the open end. $D_{s,h}$ is the appropriate soft or hard diffraction coefficient (Keller's form [1]) given by

$$D_{s,h}(\phi, \phi') = \frac{\sin\left(\frac{\pi}{n}\right)}{n\sqrt{j2\pi k}}\left[\frac{1}{\cos\frac{\pi}{n} - \cos\left(\frac{\phi-\phi'}{n}\right)} \mp \frac{1}{\cos\frac{\pi}{n} - \cos\left(\frac{\phi+\phi'}{n}\right)}\right]$$

(4.3)

where

$$n = 2 - \frac{WA}{\pi}$$

(4.4)

104

WA = wedge angle of the rim, as shown in Figure 47.

"Soft" and "hard" refer to the polarization and correspond to perpendicular and parallel, respectively. The edge scattered field given by (4.2-4.4) includes only first order non-uniform diffraction. This first order result in (4.42) is quite adequate for large guide widths d and for incidence and scattering angles which are not too steep ($|\theta_i, \theta_s| < 60°$) because the higher order diffraction effects will in such cases be negligible and the transition regions associated with shadow boundaries will not be in the directions of interest.

In general, the total field scattered by a large open-ended waveguide cavity is dominated by the interior scattering, whereas, the edge scattering is almost negligible by comparison. However, if the cavity contains a large amount of loss, such as that due to interior absorber wall coatings, the edge scattering may become much more noticeable. Therefore, it is important to include this scattering mechanism in calculations, especially if there is loss present.

The contribution to the scattering from the interior of an open-ended waveguide cavity is found by coupling the plane wave field incident on the open end into the cavity and then tracking the fields via a GB expansion through the cavity to the termination. The fields at the termination are then integrated using the reciprocity integral described in Appendix C and derived in [30]. From (C.15), the termination reciprocity integral is given as before for the general 3-D bistatic case by

$$\vec{E}_s'(P) \cdot \vec{p} = - \int\int_{S_t} \left(\vec{E}_i \times \vec{H}_s' - \vec{E}_s' \times \vec{H}_i \right) \cdot \hat{n} dS. \tag{4.5}$$

See Appendix C for definitions of the quantities and geometry used for this 3-D case (they will be defined later for the 2-D case). In general, the primed quantities are associated as before with a point source located at P' and the corresponding

unprimed quantities are associated with a point source located at P. For the 2-D case of perpendicular polarization, the E-fields are in the $\hat{z}$ direction (out of the page), the H-fields are in the plane of the page and $\vec{p}$ is replaced by the strength I of a $\hat{z}$ directed electric line source. Also, P' in is the direction of θ_i and P is in the direction of θ_s of Figure 47. The left side of (4.5) becomes

$$
\begin{aligned}
\vec{E}'_s(P) \cdot \vec{p} &= \hat{z} E'_s(\theta_s) \cdot (\hat{z} I) \\
&= E'_s(\theta_s) I
\end{aligned}
\tag{4.6}
$$

where

$$
\begin{aligned}
E'_s(\theta_s) &= \text{electric field in the direction of } \theta_s \text{ scattered by the termination,} \\
&\quad \text{due to a plane wave incident from the direction of } \theta_i, \\
I &= \hat{z} \text{ directed electric current source located at the point where} \\
&\quad E'_s(\theta_s) \text{ is to be evaluated.}
\end{aligned}
$$

The H-field can be derived from the $\hat{z}$ directed E-field for this case using one of Maxwell's equations:

$$
\begin{aligned}
\vec{H} &= -\frac{1}{jkZ_o} \nabla \times \vec{E} \\
&= -\frac{1}{jkZ_o} \left(\hat{x}\frac{\partial}{\partial x} + \hat{y}\frac{\partial}{\partial y} \right) \times (\hat{z} E) \\
&= -\frac{1}{jkZ_o} \left(\hat{x}\frac{\partial E}{\partial y} - \hat{y}\frac{\partial E}{\partial x} \right).
\end{aligned}
\tag{4.7}
$$

The integral of (4.5) can now be reduced as follows:

$$
\begin{aligned}
-\int\int_{S_t} \left(\vec{E}_i \times \vec{H}'_s - \vec{E}'_s \times \vec{H}_i \right) \cdot \hat{n} dS &= -\int_0^d \left[(\hat{z} E_i) \times \frac{-1}{jkZ_o} \left(\hat{x}\frac{\partial E'_s}{\partial y} - \hat{y}\frac{\partial E'_s}{\partial x} \right) \right. \\
&\quad \left. - (\hat{z} E'_s) \times \frac{-1}{jkZ_o} \left(\hat{x}\frac{\partial E_i}{\partial y} - \hat{y}\frac{\partial E_i}{\partial x} \right) \right] \cdot (-\hat{x}) dy \\
&= \frac{-1}{jkZ_o} \int_0^d \left(E_i \frac{\partial E'_s}{\partial x} - E'_s \frac{\partial E_i}{\partial x} \right) dy
\end{aligned}
\tag{4.8}
$$

106

where $\hat{n}$ has been replaced by $-\hat{x}$ and the integral is over y from 0 to d, as Figure 47 illustrates.

The field incident on the open end of the cavity due to the line source at P, i.e., from the direction of θ_s, is given by

$$E_{io} = -Z_o I \sqrt{\frac{jk}{8\pi}} \frac{e^{-jk\rho}}{\sqrt{\rho}} \tag{4.9}$$

where

ρ = distance from the center of the open end to P (from θ_s direction).

As ρ approaches infinity, this field looks like a plane wave incident on the cavity with magnitude E_{io} incident from the direction of θ_s. Using this result along with (4.6) and (4.9), after some rearranging gives

$$E'_s(\theta_s) = \frac{1}{E_{io}\sqrt{j8\pi k}} \frac{e^{-jk\rho}}{\sqrt{\rho}} \int_0^d \left(E_i \frac{\partial E'_s}{\partial x} - E'_s \frac{\partial E_i}{\partial x} \right) dy. \tag{4.10}$$

Using the equivalence theorem [32], $H'_s(\theta_s)$ for the parallel polarization case is obtained by replacing E with H in (4.10), and in general

$$U'_s(\theta_s) = \frac{1}{U_{io}\sqrt{j8\pi k}} \frac{e^{-jk\rho}}{\sqrt{\rho}} \int_0^d \left(U_i \frac{\partial U'_s}{\partial x} - U'_s \frac{\partial U_i}{\partial x} \right) dy \tag{4.11}$$

where

U = $\hat{z}$ directed E-field for $\perp$ polarization or $\hat{z}$ directed H-field for $\parallel$ polarization,

$U'_s(\theta_s)$ = scattered field in the direction of θ_s (towards P) due to a plane wave incident from the direction of θ_i (from P'),

U_i = fields from the source at P in the absence of the termination,

U'_s = fields from the source at P' in the presence of the termination,

U_{io} = magnitude of the plane wave incident on the open end of the cavity from the direction of θ_s (from P).

and the integral is over a cross-section in the cavity conveniently chosen near the termination.

Equation (4.11) can also be expressed in terms of the modes of the waveguide cavity region near the termination, if it is assumed that the region is separable so that the modes can be found analytically, following a procedure similar to that used in deriving (4.11), but starting with Equation (C.27) and using (C.22), (C.29) and (C.30). The scattered field in the direction of θ_s (at P) is then given by

$$U_s'(\theta_s) = \frac{+2}{U_{io}\sqrt{j8\pi k}} \frac{e^{-jk\rho}}{\sqrt{\rho}} \sum_{n=1}^{N} A_n^+ A_n^{-\prime} \tag{4.12}$$

where

$$[A^{-\prime}] = [S_\Gamma][A^{+\prime}] \tag{4.13}$$

$$A_n^+ = \int_0^d u_{nz} \frac{\partial U_i}{\partial x} dy \tag{4.14}$$

$$A_n^{+\prime} = \int_0^d u_{nz} \frac{\partial U_i'}{\partial x} dy \tag{4.15}$$

and

u_{nz} = $\hat{z}$ component of the nth waveguide modal field (e_{nz} or h_{nz}, for $\perp$ or $\parallel$ polarization, respectively),

N = number of included waveguide modes,

$[A^{-\prime}], [A^{+\prime}]$ = column matrices of order N containing the modal coefficients $A_n^{-\prime}$ and $A_n^{+\prime}$, respectively,

$[S_\Gamma]$ = modal termination reflection matrix of order $N \times N$,

U_i, U_i' = fields from the sources at P and P' in the absence of the termination, respectively.

It is assumed that the waveguide cavity region near the termination in this 2-D case is a parallel plate region; thus the waveguide modal fields for this 2-D case are the parallel plate waveguide modes and are found in Appendix A. $[S_\Gamma]$, the modal termination reflection matrix is discussed in Section 2.3.4, and determines the coefficients of the modal field reflected by the termination to the coefficients of the incident modal field. The incident modal coefficients are found from the fields incident from P and P' and are given by (4.14) and (4.15), respectively.

The fields inside the cavity are found by first expanding the incident fields in the open end in terms of shifted and rotated Gaussian beams (GB's). Each GB of the expansion of the fields at the open end is then tracked like a ray along the beam axis to the termination within the waveguide cavity. In order to track beams axially like rays and maintain sufficient resolution even after successive reflections off the interior walls it is necessary to have well focussed or spectrally narrow GB's. However, such spectrally narrow GB's have wide waists. It is thus important to be able to have spectrally narrow GB's whose waists can fit easily within the waveguide cavity. Typically, the initial waists of the GB's at the aperture plane should be about half the width of the original aperture. The latter can be accomplished by dividing the aperture at the open end into equally sized sub-apertures, and then expanding the fields of each sub-aperture into a superposition of rotated GB's with equal angular spacing between each rotated beam. Figure 6 illustrates this sub-aperture expansion and shows one GB being launched and tracked inside the cavity.

The fields at a point P_c inside the cavity (such as at the termination plane) can then be written as a sum of GB's as

$$U_i(P_c) \; = \; \sum_{m=-M}^{M} \sum_{n=-N}^{N} A_m(\theta_s, \theta_n) B_{mn}(P_c) \qquad (4.16)$$

109

$$U_i^I(P_c) \; = \; \sum_{m=-M}^{M} \sum_{n=-N}^{N} A_m(\theta_i, \theta_n) B_{mn}(P_c) \qquad (4.17)$$

where

$B_{mn}(P_c)$ = field at P_c due to the Gaussian beam launched

from sub-aperture m at an angle θ_n, which has

been traced inside the cavity,

$2M + 1$ = number of sub-apertures,

$2N + 1$ = number of GB's per sub-aperture,

$A_m(\theta_{i,s}, \theta_n)$ = expansion coefficients for the mn^{th} GB which

depend on the incidence angle θ_i or the

scattering angle θ_s, respectively.

Note that only the GB coefficients $A_m(\theta_i, \theta_n)$ and $A_m(\theta_s, \theta_n)$ change with the angles of incidence while the directions of the beams do not so that the beams need to be tracked only once and not each time the incident angle changes.

Section 4.2 will derive the GB basis function used in the expansion of (4.16) and (4.17) and Section 4.3 will derive the expansion coefficients $A_m(\theta_{i,s}, \theta_n)$. Section 4.4 will then discuss how the GB's are traced axially like rays from the open end of the cavity to some point P_c inside the cavity, such as to the termination plane.

4.2 Gaussian Beams as Field Basis Functions

The present Gaussian beam (GB) method uses well focused GB's to axially track the fields inside a waveguide cavity. This method is useful because the GB's are exact solutions to the wave equation (in paraxial regions) and therefore are well-behaved everywhere (even at caustics), and their propagation and scattering

110

characteristics can be found using conventional techniques. Also, it has been shown by Gabor that a set of Gaussian distributions with appropriate linear phases can be used as a complete expansion for aperture fields [28,29]. In fact, this type of Gabor expansion has been used in similar problems involving aperture radiation in the presence of complex environments, such as in a radome [27], because it gives a rigorous method of launching Gaussian beams. However, the Gabor expansion is not used here for the cavity scattering problem because it gives rise to GB's which have parameters that vary depending on the amount of their rotation. In other words, all of the beams arising from the Gabor expansion are not identical, which hampers the effectiveness of the method when applied to arbitrarily shaped geometries. The Gabor expansion was useful in [27] because the beam tracking was done using complex ray tracing. This technique gives more reliable results than the axial beam tracking method used here, but it is not practical for complicated geometries where there are multiple reflections, such as in an arbitrarily shaped cavity.

The results in this section are restricted to two dimensions, however, the GB method can be extended to 3-D in a straightforward manner. In this section the GB basis function which will be used in the sub-aperture expansion will be derived from a 2-D Green's function with a complex source location [33], and some of the important properties of the GB basis function will be discussed.

4.2.1 A Gaussian beam as the paraxial field of a point source located in complex space.

A GB can be derived as the paraxial form of the 2-D Green's function when the source point is located in complex space [33]. The 2-D free space Green's

function is given by

$$G_o(r) = -\frac{j}{4}H_o^{(2)}(kr) \tag{4.18}$$

$$\approx -\frac{1}{\sqrt{j8\pi k}}\frac{e^{-jkr}}{\sqrt{r}}, \text{ for } kr \gg 1 \tag{4.19}$$

where

$$r = \sqrt{(x - x')^2 + (z - z')^2} \tag{4.20}$$

$H_o^{(2)}(kr) = $ Hankel function of the second kind of order zero and

argument kr,

$(x, z) = $ coordinates of the receiver,

$(x', z') = $ coordinates of the source point.

The paraxial form of r is

$$r \approx z - z' + \frac{(x - x')^2}{2(z - z')}, \text{ for } |z - z'|^2 \gg |x - x'|^2. \tag{4.21}$$

To obtain the desired Gaussian amplitude characteristic, the source location is placed in complex space at $(x', z') = (0, -jb)$ where b is a positive real constant referred to as the "beam parameter". (4.21) becomes

$$r \approx z + jb + \frac{x^2}{2(z + jb)}, \text{ for } |z + jb|^2 \gg |x|^2$$

$$\approx z + jb + \frac{1}{2}z\frac{x^2}{z^2 + b^2} - j\frac{1}{2}b\frac{x^2}{z^2 + b^2}. \tag{4.22}$$

Substituting this result into (4.19) gives the paraxial free space Green's function for a complex source location as

$$G_o(x, z) = -\frac{e^{kb}}{\sqrt{j8\pi k}}\frac{1}{\sqrt{z + jb}}e^{-jkz\left(1 + \frac{1}{2}\frac{x^2}{z^2 + b^2}\right)}e^{-\frac{1}{2}kb\frac{x^2}{z^2 + b^2}}$$

$$\text{for } |z + jb|^2 \gg |x|^2 \tag{4.23}$$

112

which has a quadratic phase front paraxial with respect to the z-axis, along with a Gaussian amplitude distribution transverse to the direction of propagation. In other words, for a constant z, the amplitude of the beam in the transverse x direction is a Gaussian function centered on the z-axis. Notice also that (4.23) is not singular at $z = 0$. This functional form appears often in the field of laser optics because it is the dominant lowest order mode of a laser beam.

4.2.2 The Gaussian beam basis function and its properties.

The GB basis function used in this chapter has the form of (4.23) with a more convenient constant in front,

$$B(x,z) = \sqrt{\frac{jb}{z+jb}}e^{-jkz\left(1+\frac{1}{2}\frac{x^2}{z^2+b^2}\right)}e^{-\frac{1}{2}kb\frac{x^2}{z^2+b^2}},$$

$$\text{for } |z+jb|^2 \gg |x|^2 \tag{4.24}$$

chosen so that $B(0,0) = 1$. Note that if b is made large enough, the GB will have significant magnitude only in the paraxial region because it will die out quickly away from the beam axis. This is the case for the well focussed GB's which are useful in the cavity scattering problem. Therefore, it is usually not necessary to keep track of where the paraxial approximation is valid because it is essentially automatically taken into consideration by the Gaussian amplitude taper.

Two important parameters of the GB are the phasefront radius of curvature $R(z)$ and the $1/e$ beam half-width $w(z)$ which are given by

$$R(z) = \frac{1}{z}(z^2 + b^2) \tag{4.25}$$

$$w(z) = \sqrt{\frac{2}{kb}(z^2 + b^2)}. \tag{4.26}$$

Of these two parameters, $w(z)$ is the most often referred to because it describes the effective boundary of the beam, outside of which the amplitude of the beam

is less than $1/e$ of its on-axis value (8.7 dB down) for $|x| > w(z)$. As z becomes much larger than b, (4.26) indicates that the beam half-width approaches a linear asymptote given by

$$w(z) = \sqrt{\frac{2}{kb}}z, \text{ for } z^2 \gg b^2. \tag{4.27}$$

Figure 48 shows a typical GB designated by shading within its $1/e$ half-width boundaries, and Figure 49 shows the beam half-width $w(z)$ plotted for different values of b, along with the asymptotes. These two figures show only the region $z > 0$ because the GB's are symmetric about the x axis as well as the beam (z) axis.

The beam waist, w_o is defined as twice the minimum of the $1/e$ half-width:

$$\begin{aligned} w_o &= 2w(0) \\ &= 2\sqrt{\frac{2b}{k}}. \end{aligned} \tag{4.28}$$

This is a measure of the width of the beam at its narrowest point, i.e., at its waist. As Figure 49 shows, GB's with smaller beam waists diverge faster than GB's with larger waists, as expected from a Maxwellian field function. However, beams with large waists may not fit inside a waveguide cavity. This is the trade-off limitation of using GB's to track the fields inside waveguides. Beams which start out small may diverge too fast and become too large to fit the waveguide after propagating a short distance. On the other hand, beams which start out with a large waist diverge slower, but they may already be too large. Therefore, this method which tracks beams axially like rays, is expected to work well only for waveguide cavities which are wide in terms of wavelength and not very long. The allowable length to width ratio will increase with frequency because it is easier to fit well focussed GB's inside for electrically large geometries.

114
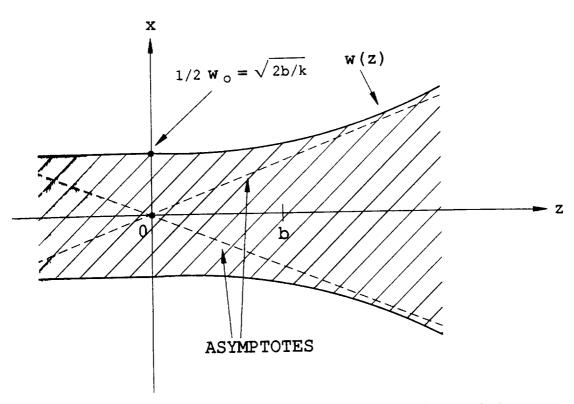
Figure 48: A Gaussian beam, shaded within its $1/e$ boundaries.
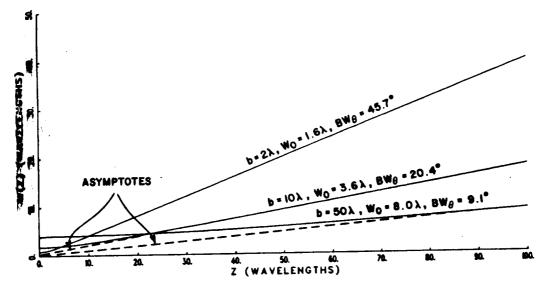
Figure 49: Gaussian beam half-width $w(z)$ plotted for 3 values of the beam parameter b.

115

The far field form of the beam basis function (4.24) is also of interest mainly so that GB's can be matched to the far field pattern of an aperture using point matching. Changing to the (ρ, θ) coordinate system,

$$
\begin{aligned}
x &= \rho \sin \theta \\
z &= \rho \cos \theta
\end{aligned}
\tag{4.29}
$$

where

$$
\begin{aligned}
\rho &= \text{distance to the observer from the origin,} \\
\theta &= \text{angular displacement from the } z\text{-axis.}
\end{aligned}
$$

Substituting these into (4.24) and letting ρ extend to infinity yields the far field GB basis function as

$$
B(\rho, \theta) = \sqrt{\frac{jb}{\rho}} e^{-jk\rho} e^{-\frac{1}{2}kb\theta^2}, \quad \text{for } |\theta| \ll \pi.
\tag{4.30}
$$

This shows that the GB basis function is also Gaussian in angle in the far field. The angular beam width, BW_θ, is defined as the $1/e$ angular width of the beam in the far field and is given by

$$
BW_\theta = 2\sqrt{\frac{2}{kb}}.
\tag{4.31}
$$

Comparing (4.28) and (4.31) shows that the beam waist varies as $\sqrt{b}$ while the angular beam width varies as $1/\sqrt{b}$. It follows that for a small angular beam width the beam parameter b is large, giving a large beam waist. This was discussed earlier in terms of the beam half-width $w(z)$ of (4.26) and (4.27) and is illustrated graphically in Figure 49, where the angles that the asymptotes make with the z-axis correspond to half the angular beam width BW_θ.

116
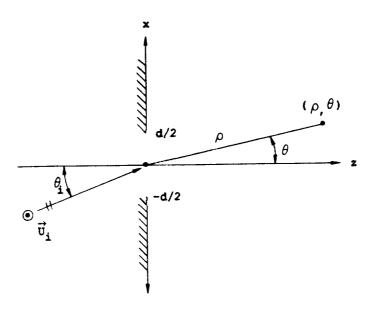
Figure 50: Plane wave incident on an aperture of width d.

4.3 Sub-Aperture Field Expansion Using Gaussian Beams

In this section, the fields radiating from an aperture illuminated by a plane wave will be expanded in terms of shifted and rotated Gaussian beam basis functions. Figure 50 shows the geometry. As mentioned before, the method presented here is similar in concept to the method of [26] and [27] which uses a complete Gabor expansion to establish an array of shifted and rotated Gaussian beams in the aperture. The difference is that in the sub-aperture expansion method of this chapter, the GB's used in the array are all identical (except for their orientation), in contrast to the Gabor method which gives rise to GB's that have differing beam waists depending on the amount of their rotation in the aperture. For the application of this report, i.e., cavity scattering, it is more desirable to use identical beams via the sub-aperture approximation which is conceptually simpler than the Gabor expansion. Also, the Gabor expansion gives rise to rotated GB's which are not equally spaced in angle, as the sub-aperture method does. However, this is not

117

necessarily a drawback of using the Gabor method for cavity scattering problems, just an added complication.

Some numerical results illustrating the technique of using GB's in a sub-aperture expansion of the fields radiating from an aperture will be presented at the end of this section.

4.3.1 Formulation of the sub-aperture expansion.

The sub-aperture expansion method described in Appendix D is used to write the fields in the $z > 0$ half-plane as a double summation of GB's:

$$U_{GB} = \sum_{m=-M}^{M} \sum_{n=-N}^{N} A_m(\theta_i, \theta_n) B(x_{mn}, z_{mn}) \tag{4.32}$$

which is a sum over the $2M + 1$ sub-apertures and the $2N + 1$ rotated GB's of each sub-aperture, and

$$B(x_{mn}, z_{mn}) = n^{th} \text{ rotated GB basis function of the } m^{th} \text{ sub-aperture,}$$

$$A_m(\theta_i, \theta_n) = \text{expansion coefficient of the } mn^{th} \text{ GB,}$$

$$(x_{mn}, z_{mn}) = \text{relative coordinate system of the } mn^{th} \text{ GB,}$$

$$\theta_n = \text{angle between the } n^{th} \text{ beam axis and the } z\text{-axis.}$$

The relative coordinate system of the mn^{th} GB is shown in Figure 51. The z_{mn}-axis is the beam axis of the mn^{th} GB which makes an angle of θ_n with the z-axis. x_{mn} and z_{mn} are given in terms of x, z, and θ_n by

$$x_{mn} = (x - m\Delta)\cos\theta_n - z\sin\theta_n \tag{4.33}$$

$$z_{mn} = (x - m\Delta)\sin\theta_n + z\cos\theta_n \tag{4.34}$$

where Δ is the sub-aperture size given by

$$\Delta = \frac{d}{2M+1}. \tag{4.35}$$

118
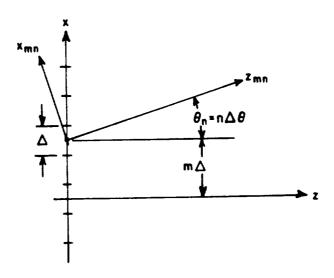
Figure 51: Coordinate system of the mn^{th} shifted, rotated Gaussian Beam.

The GB's are equally spaced in angle, i.e.,

$$\theta_n = n\Delta\theta \tag{4.36}$$

$\Delta\theta$ = angular separation between adjacent rotated beams.

The GB basis function $B(x, z)$ is defined by (4.24).

As discussed earlier, it is noted that the expansion of (4.32) is slightly different than the Gabor based expansion used in [29,26] and [27]. Gabor's expansion consists of a double summation over shifted Gaussian functions with linear phases [28]. It happens that in the paraxial region, a rotated Gaussian beam has a linear phase through its waist. Therefore, the fields of an aperture which are written as a Gabor expansion can be continued or propagated as GB's beyond the aperture by noting that the linearly phased Gaussian functions in the aperture correspond to shifted and rotated Gaussian beams whose waists are in the aperture. This is because the propagation characteristics of GB's are well known everywhere within the paraxial region. However, as mentioned earlier, Gabor's expansion gives rise to GB's which are not all identical and equally spaced in angle, in contrast to the

119

sub-aperture expansion of (4.32). In fact, as shown in [26], it also gives rise to evanescent type beams which die out away from the aperture. Furthermore, Gabor's expansion is a double infinite summation which must be truncated somehow to be of practical use, as investigated in [26]. In the course of the work detailed in this report, it was found that the expansion of (4.32) is more useful for the open-ended waveguide cavity application. As will be shown later, this expansion also remains valid in both the near and far fields of the aperture.

To find the expansion coefficients $A_m(\theta_i, \theta_n)$, the far field pattern of the mth sub-aperture illuminated by a plane wave is used. This is given by

$$U_{PO}(\rho_m, \theta_m) = 2U_o\Delta\sqrt{\frac{jk}{8\pi}}\frac{e^{-jk(\rho_m + m\Delta\sin\theta_i)}}{\sqrt{\rho_m}}\text{sinc}\left[\frac{1}{2}k\Delta(\sin\theta_m - \sin\theta_i)\right]$$

(4.37)

where

$$\rho_m, \theta_m = \text{polar coordinates of the } m^{th} \text{ sub-aperture (see Figure D.2),}$$

$$U_o = \text{magnitude of the incident plane wave.}$$

(4.37) is derived in Appendix D using the Physical Optics (PO) approximation (or equivalently, the Kirchhoff approximation). This far field pattern can also be written in terms of the far field form of the GB's (4.30) as

$$U_{GB}(\rho_m, \theta_m) = \sum_{n=-N}^{N} A_m(\theta_i, \theta_n)B(\rho_m, \theta_m, \theta_n)$$

(4.38)

where

$$B(\rho_m, \theta_m, \theta_n) = \sqrt{\frac{jb}{\rho_m}}e^{-jk\rho_m}e^{-\frac{1}{2}kb(\theta_m - n\Delta\theta)^2}.$$

(4.39)

(4.38) is a superposition of rotated GB's which have their maxima at $\theta_m = \theta_n = n\Delta\theta$, as (4.39) indicates.

120

In the expansion of (4.38), it remains to find the expansion coefficients $A_m(\theta_i, \theta_n)$ and the beam parameter b in terms of the PO function of (4.37) and the beam spacing $\Delta\theta$. Consider an arbitrary function $f(x)$ expanded as a sum of equally spaced Gaussian distributions with equal standard deviations σ:

$$f(x) = \sum_{n=-\infty}^{\infty} C_n e^{-\frac{(x-n\delta)^2}{2\sigma^2}}, \text{ for } -\infty < x < \infty \qquad (4.40)$$

where

$$C_n = \text{expansion coefficient of the } n^{th} \text{ Gaussian distribution,}$$

$$\sigma = \text{standard deviation of the Gaussian distributions,}$$

$$\delta = \text{spacing between peaks of the Gaussian distributions.}$$

It is theoretically feasible to allow σ and δ to vary with n, as might be true were this a Gabor type expansion, but for our purposes it is desirable to have all the Gaussian distributions (Gaussian beams) be the same. The latter requires that C_n depend only on the function $f(x)$, whereas σ is then required to depend only on the spacing δ and not on $f(x)$. To do this it is assumed that only adjacent beams overlap enough to affect each other. So, beam n' overlaps beams $n' + 1$ and $n' - 1$ but dies out too fast to significantly overlap with beams $n' + 2$ and $n' - 2$ and hence also with all the other beams. It is further assumed that $f(x)$ varies slowly with respect to the beam spacing δ. Figure 52 illustrates this by showing beam n' with two adjacent overlapping beams and $f(x)$ in the vicinity of $x = n'\delta$.

Using the above assumptions, (4.40) and its derivative at $x = n'\delta$ are given approximately by

$$f(n'\delta) \approx C_{n'-1}e^{-\frac{\delta^2}{2\sigma^2}} + C_{n'} + C_{n'+1}e^{-\frac{\delta^2}{2\sigma^2}} \qquad (4.41)$$

$$f'(n'\delta) \approx -\frac{\delta}{\sigma^2}C_{n'-1}e^{-\frac{\delta^2}{2\sigma^2}} + \frac{\delta}{\sigma^2}C_{n'+1}e^{-\frac{\delta^2}{2\sigma^2}} \qquad (4.42)$$

121
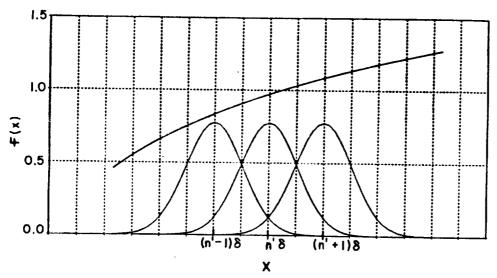
Figure 52: Gaussian basis function n' and the two adjacent basis functions along with $f(x)$.

It is desirable to eliminate $f'(n'\delta)$ from (4.42) by approximating it with the average of the slopes of $f(x)$ on either side of $x = n'\delta$, i.e.,

$$f'(n'\delta) \approx \frac{1}{2}\left[\frac{f(n'\delta) - f(n'\delta - \delta)}{\delta} + \frac{f(n'\delta + \delta) - f(n'\delta)}{\delta}\right]$$

$$= -\frac{1}{2\delta}f\left[(n'-1)\delta\right] + \frac{1}{2\delta}f\left[(n'+1)\delta\right]. \qquad (4.43)$$

Comparing (4.42) and (4.43) implies that each term in (4.42) corresponds to the same term of (4.43). For example, equating the last terms,

$$\frac{\delta}{\sigma^2}C_{n'+1}e^{-\frac{\delta^2}{2\sigma^2}} = \frac{1}{2\delta}f\left[(n'+1)\delta\right], \qquad (4.44)$$

which yields the general relation

$$C_n = \frac{\sigma^2}{2\delta^2}e^{\frac{\delta^2}{2\sigma^2}}f(n\delta). \qquad (4.45)$$

This result shows that the expansion coefficients C_n of (4.40) are proportional to the function $f(x)$ evaluated at the peaks $x = n\delta$ of the Gaussian distributions, as is expected in this point matching technique.

122

Using (4.45) in (4.41) gives

$$f(n'\delta) \ = \ \frac{\sigma^2}{2\delta^2} f\left[(n'-1)\delta\right] + \frac{\sigma^2}{2\delta^2} e^{\frac{\delta^2}{2\sigma^2}} f(n'\delta) + \frac{\sigma^2}{2\delta^2} f\left[(n'+1)\delta\right]$$

(4.46)

which can be rearranged as

$$f(n'\delta)\left(\frac{2\delta^2}{\sigma^2} - e^{\frac{\delta^2}{2\sigma^2}}\right) \ = \ f\left[(n'-1)\delta\right] + f\left[(n'+1)\delta\right].$$

(4.47)

This equation could be solved for σ, but it would depend on n', which is not desirable for reasons mentioned earlier. However, another reasonable approximation is to assume that if $f(x)$ is slowly varying over an incremental distance 2δ, then $f(n'\delta)$ is given approximately by the average of the function on either side of $x = n'\delta$, as

$$f(n'\delta) \ \approx \ \frac{1}{2}\left\{f\left[(n'-1)\delta\right] + f\left[(n'+1)\delta\right]\right\}.$$

(4.48)

It is noted that this approximation and the one in (4.43) become exact as δ approaches zero.

Using (4.48) in (4.47) yields the transcendental equation for σ:

$$\frac{\delta^2}{\sigma^2} - \frac{1}{2} e^{\frac{\delta^2}{2\sigma^2}} - 1 \ = \ 0,$$

(4.49)

which unfortunately has no real solution. However, it does have a maxima which is close to a solution, as shown in Figure 53. This maxima is found by setting the derivative of (4.49) equal to zero and solving for δ^2/σ^2, which yields

$$\frac{\sigma^2}{\delta^2} \ = \ 2\log 4.$$

(4.50)

Using this result along with (4.45) provides the two required parameters of the point-matched Gaussian expansion of (4.40):

$$\sigma \ = \ \frac{\delta}{\sqrt{2\log 4}} \ \approx \ .6006\,\delta$$

(4.51)

123
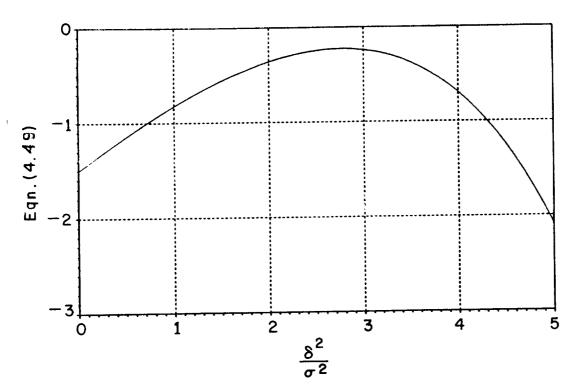
Figure 53: Plot of Equation (4.49).

$$C_n = \frac{1}{\log 4} f(n\delta) \approx .7213 \; f(n\delta). \qquad (4.52)$$

Comparing the expansions of (4.40) and (4.38) along with (4.39), the following correspondences are evident:

$$x \rightarrow \theta_m \qquad (4.53)$$

$$\delta \rightarrow \Delta\theta \qquad (4.54)$$

$$\frac{1}{\sigma^2} \rightarrow kb \qquad (4.55)$$

$$C_n \rightarrow A_m(\theta_i, \theta_n)\sqrt{\frac{jb}{\rho_m}} e^{-jk\rho_m} \qquad (4.56)$$

$$f(n\delta) \rightarrow U_{PO}(\rho_m, \theta_n) \qquad (4.57)$$

which along with (4.37), (4.51) and (4.52) gives

$$b = \frac{2\log 4}{k\Delta\theta^2} \qquad (4.58)$$

124

$$A_m(\theta_i, \theta_n) = \frac{2}{\log 4} U_o \Delta \sqrt{\frac{k}{8\pi b}} e^{-jkm\Delta \sin \theta_i} \text{sinc} \left[\frac{1}{2} k\Delta(\sin \theta_n - \sin \theta_i) \right].$$

$$(4.59)$$

(4.58) gives b in terms of $\Delta\theta$, either of which can be chosen to best fit the given sub-aperture size. For example, $\Delta\theta$ should be small enough so that the far field pattern is adequately reproduced by the GB expansion. This is achieved by requiring that there are at least three or four GB's per lobe of the far field pattern. However, for a small sub-aperture size the lobes might be quite large, so a larger number of narrower GB's may be desirable to keep the GB's well focused and confined within the paraxial region. On the other hand, (4.58) shows that a small $\Delta\theta$ will make b large which will make the beam waist, w_o, of (4.29) large, as discussed earlier in terms of the angular beam width, BW_θ. In fact, the angular beam width can now be written in terms of the beam spacing by substituting (4.58) into (4.32):

$$BW_\theta = \frac{2}{\sqrt{\log 4}} \Delta\theta \approx 1.4427 \, \Delta\theta \qquad (4.60)$$

which shows that the angular beam width is a little larger than the angular beam spacing, as might be expected because the GB's should overlap somewhat to adequately cover all space.

4.3.2 Numerical results of the Gaussian beam sub-aperture expansion.

Consider the aperture geometry of Figure 54. It shows a 14.9 wavelength aperture illuminated by a plane wave incident at 15° and has five sub-apertures of width 2.98 wavelengths, each. Figure 55 shows the physical optics far field pattern of one of the sub-apertures (solid line) and its GB expansion (dotted line) which used approximately 3.5 beams per lobe of the pattern (actually, this means 3.5 beams per side lobe because the main lobe is approximately twice the width of a side lobe). Also shown are four typical adjacent GB's inside the main lobe which

125
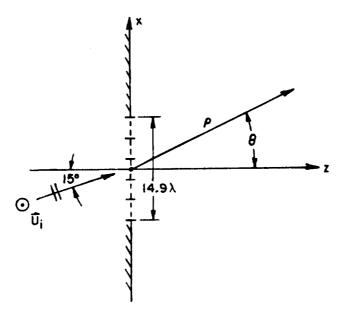
Figure 54: Aperture illuminated by a plane wave incident at 15° with 5 sub-apertures.

together sum up to give the middle part of the main lobe. The GB expansion can be improved in accuracy by increasing the number of beams per lobe, as shown in Figure 56, which is the same case as in Figure 55 except that 4.5 beams per lobe are used.

Figures 57 and 58 show the total aperture far field pattern found by summing the five individual sub-aperture patterns, using 3.5 and. 4.5 beams per lobe, respectively (dotted line). They both give excellent agreement with the PO result (solid line), with the 4.5 beams per lobe case being slightly more accurate than the 3.5 beams per lobe case, as expected.

Because the GB's are valid everywhere, the radiated fields can be back-tracked to the aperture and compared with the incident field in the aperture. Figures 59(a) and (b) show the phase and amplitude of the fields in the plane of the aperture, respectively, corresponding to the far field pattern of Figure 57, which used 3.5 beams per lobe. The agreement is quite good, showing that the Gaussian
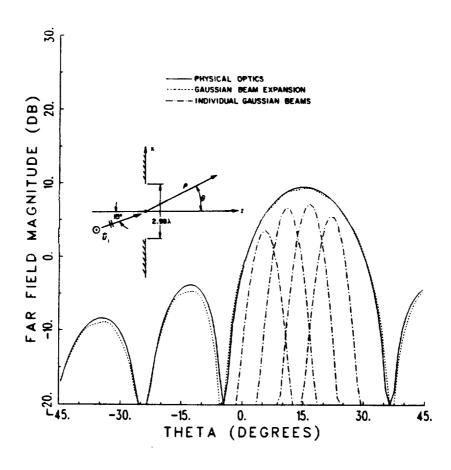
Figure 55: Far field pattern of a sub-aperture illuminated by a plane wave and 4 typical component Gaussian beams, 3.5 beams/lobe. $\Delta\theta = 5.5°$, $b = 64.0\ \lambda$, $w_o = 9.0\ \lambda$.

127
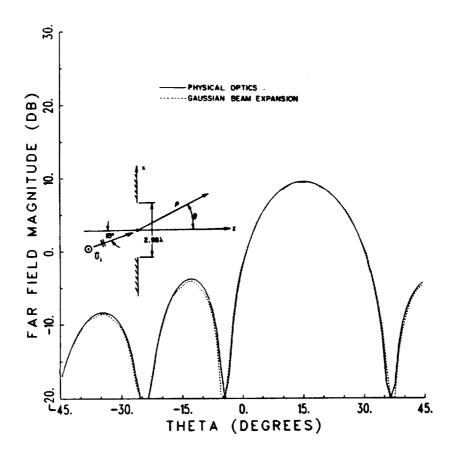
Figure 56: Far field pattern of a sub-aperture illuminated by a plane wave, 4.5 beams/lobe. $\Delta\theta = 4.3°$, $b = 105.8\ \lambda$, $w_o = 11.6\ \lambda$.

128
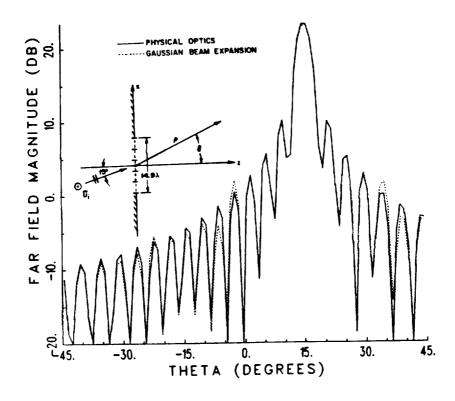
Figure 57: Far field pattern of an aperture illuminated by a plane wave. 5 sub-apertures, 3.5 beams/lobe, $\Delta\theta = 5.5°$, $b = 64.0$ λ, $w_o = 9.0$ λ.

129
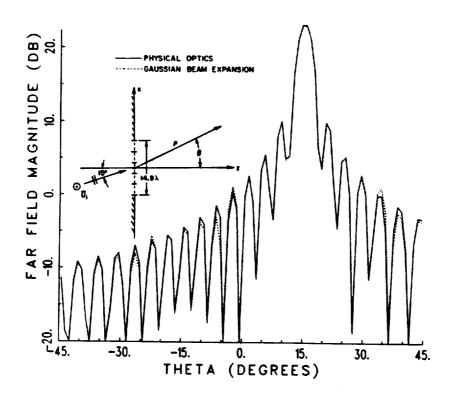
Figure 58: Far field pattern of an aperture illuminated by a plane wave. 5 sub-apertures, 4.5 beams/lobe, $\Delta\theta = 4.3°$, $b = 105.8$ λ, $w_o = 11.6$ λ.

(a) phase

(b) amplitude
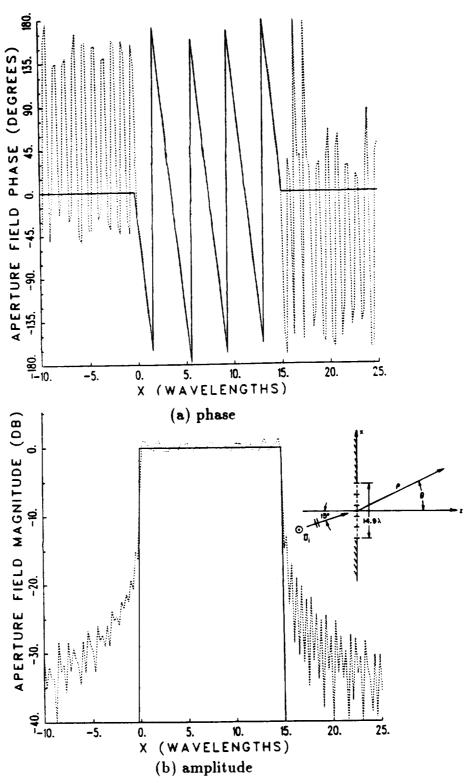
Figure 59: Fields in the plane of an aperture illuminated by a plane wave. 5 sub-apertures, 3.5 beams/lobe, $b = 64.0$ λ, $w_o = 9.0$ λ.

beam expansion of fields can be used in the aperture as well as in the far field, and since the individual GB's are solutions to the wave equation, the expansion is valid everywhere in between. Also, because GB's propagate independently of one another, each beam can be tracked individually via reflections/transmissions through complex environments, provided that there is an adequate beam tracking procedure available.

Notice that for the cases of Figures 55, 57 and 59, the width of the beam waist w_o, is 9.0 λ, which is larger than the sub-aperture width of 2.98 λ and larger than half the aperture width of 14.9 λ. This suggests a problem may arise when it comes to tracing the GB's inside a waveguide cavity because the beams may start out with a width comparable to that of the cavity aperture. This is, in fact, the main limitation of the GB tracking method when applied to open-ended waveguide cavities and will be discussed further in later sections of this chapter.

4.4 Tracking the Gaussian Beams Axially Through the Interior of the Cavity

Once the GB's have been established in the sub-aperture expansion of the fields in the open end of the waveguide cavity, as described in Section 4.3, they must each be tracked individually through the interior of the cavity to the termination. This requires insight into how the beams propagate and reflect in the presence of waveguide walls. To do this rigorously, the fields inside the cavity due to a line source must be found as accurately as possible, and then the line source can be given a location in complex space; this directly furnishes the propagation of a Gaussian beam within the same environment, as discussed in [27,34,35,36,37]. Recall that in Section 4.2, a line source located in complex space generates a Gaussian beam in the paraxial region along some axis. However, to find the fields due

132

to a line source in the presence of arbitrarily shaped waveguide walls as a function of only the source and receiver location is very difficult computationally because the reflection points must be searched for numerically. When the line source is located in complex space, this search becomes an order of magnitude more difficult because the reflecting surfaces have extensions into complex space. This problem has been solved only for a few simple configurations such as reflection and transmission at a planar or curved interface between two dissimilar dielectrics [34,35], single reflection from a parabolic reflector antenna [36], the multiple reflection of a GB inside a circular cross section [37], and the transmission of GB's through a 2-D radome [27].

Inside an arbitrarily shaped waveguide cavity, it is convenient to track the GB's approximately like rays by tracking only their beam axes. In other words, the GB is assumed to have most of its energy confined to a narrow region around the beam axis, and a beam which is incident on a curved reflecting surface is assumed to give rise to a new reflected beam which is also Gaussian in nature. If the parameters of this new GB can be found easily in terms of the incident beam, the GB can be traced from reflection to reflection, much like tracing a ray in the Geometrical Optics (GO) method. However, it has been shown in [35] that the reflected beam in this case may look Gaussian for many practical cases, but in general it has asymmetries present. These asymmetries arise for cases where the incident GB has a width comparable to the radius of curvature of the surface or when the incident GB grazes the surface as shown in Figure 60. Also, because the curvature of the interior waveguide walls gradually changes, the GB's must be kept narrow enough so that the area of the surface that they illuminate has an approximately constant radius of curvature. These limitations are not always easy to overcome, especially at lower frequencies and for waveguide cavities which

133
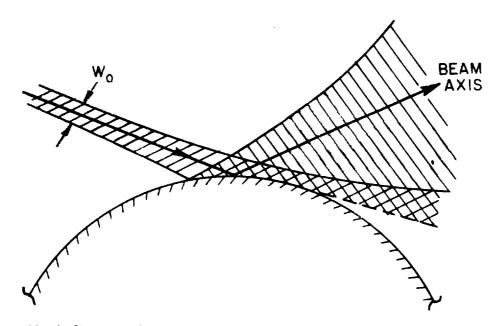
Figure 60: A Gaussian beam which reflects near grazing from a curved surface.

are long compared to their width. This will be discussed further in the numerical results section.

A simple, approximate way of finding the axial reflection of a Gaussian beam from a curved surface very similarly to GO ray tracing, is derived in this section. As will be seen, the main difference between the reflection of the beam axis and GO reflected ray tracing is that, unlike the real GO rays which have real caustic locations, the reflected beam will have complex caustic positions. This is not surprising considering that GB's can be derived from a source which is located in complex space, as described in Section 4.2. In the derivation, it is assumed that the incident GB illuminates a small area on the surface and that it does not come close to grazing incidence on the surface.

Figure 61 shows the geometry for a GB reflecting off a curved surface. It shows an incident beam field given by

$$U_i(x,z) \;=\; U_o' \sqrt{\frac{jb'}{z - z_o' + jb'}} \, e^{-jk\left[z + \frac{1}{2}\frac{(z-z_o')x^2}{(z-z_o')^2 + b'^2}\right]} e^{-\frac{1}{2}\frac{kb'x^2}{(z-z_o')^2 + b'^2}}$$

134
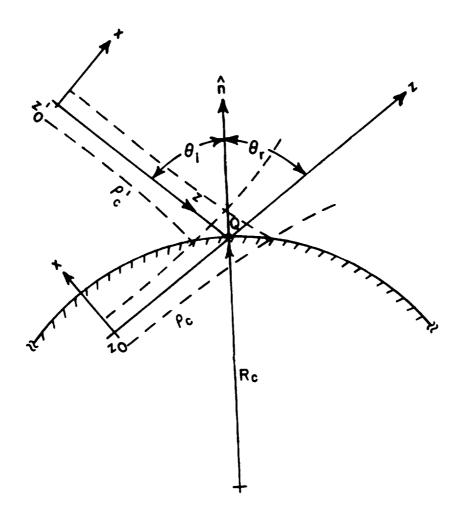
Figure 61: Gaussian beam reflecting off a curved surface.

$$\text{for } z < z'_o + \rho'_c. \tag{4.61}$$

In this approximation, the reflected field is assumed to be a new Gaussian beam whose axis intersects the surface at the same point as the incident beam axis. The reflected beam is given by

$$U_r(x,z) = U_o \sqrt{\frac{jb}{z - z_o + jb}} e^{-jk\left[z + \frac{1}{2}\frac{(z-z_o)x^2}{(z-z_o)^2 + b^2}\right]} e^{-\frac{1}{2}\frac{kbx^2}{(z-z_o)^2 + b^2}}$$
$$\text{for } z > z'_o + \rho'_c. \tag{4.62}$$

These have the same form as the beam basis function of (4.24) but are shifted along the z-axis. The parameters used in (4.61) and (4.62) are defined as

z = the total phase propagation at any point along the beam axis,

x = the coordinate transverse to the z-axis,

U_o, U'_o = coefficients of the beams,

b, b' = beam parameters,

z_o, z'_o = beam waist positions along the z-axis,

where the primed quantities are associated with the GB before reflection and the corresponding unprimed quantities are associated with the GB after reflection. Note that the z-axis, which is always the beam axis, changes directions after reflection. Again referring to Figure 61,

ρ'_c, ρ_c = distances from the beam waist to the point of reflection Q, before and after reflection, respectively,

R_c = radius of curvature of the surface at Q,

$\hat{n}$ = unit vector normal to the surface at the point Q,

θ_i, θ_r = angles the incident and reflected beam axes make with $\hat{n}$, respectively.

This derivation is also valid for concave surfaces for which R_c is negative.

The parameters of the reflected beam, U_o, b, z_o, ρ_c, and θ_r can be found in terms of the incident parameters by matching the fields on the surface in the vicinity of the reflection point Q of the beam axis. First, matching the beams exactly at point Q gives

$$R(\theta_i)U_o'\sqrt{\frac{jb'}{\rho_c' + jb'}}e^{-jk(z_o' + \rho_c')} \;=\; U_o\sqrt{\frac{jb}{\rho_c + jb}}e^{-jk(z_o + \rho_c)} \qquad (4.63)$$

where

$$R(\theta_i) \;=\; \text{reflection coefficient at } Q.$$

This equation yields U_o and z_o as

$$U_o \;=\; R(\theta_i)U_o'\sqrt{\frac{b'(\rho_c + jb)}{b(\rho_c' + jb')}} \qquad (4.64)$$

$$z_o \;=\; z_o' + \rho_c' - \rho_c. \qquad (4.65)$$

The remaining parameters can be found by expanding each of the incident and reflected beam fields in a Taylor series as a function of the displacement from point Q along the surface. Equating the constant terms of these two series gives (4.63) above. Equating the linear terms yields the relation

$$\theta_r \;=\; \theta_i \qquad (4.66)$$

which is the law of reflection for a GO ray. Finally, equating the quadratic terms of the two Taylor series expansions and using the reflection law of (4.66) yields

$$\frac{1}{\rho_c + jb} \;=\; \frac{1}{\rho_c' + jb'} + \frac{2}{R_c \cos\theta_i}. \qquad (4.67)$$

This is the same result as GO would give for a ray along the beam axis, except that the caustic distances are now complex, with real parts ρ_c and ρ_c' and imaginary parts jb and jb'.

ρ_c and b can be solved for separately by inverting (4.67) and equating the real and imaginary parts, which yields

$$\rho_c = R_c \cos \theta_i \frac{\rho_c'(R_c \cos \theta_i + 2\rho_c') + 2b'^2}{(R_c \cos \theta_i + 2\rho_c')^2 + 4b'^2} \tag{4.68}$$

$$b = b' \frac{(R_c \cos \theta_i)^2}{(R_c \cos \theta_i + 2\rho_c')^2 + 4b'^2}. \tag{4.69}$$

Notice from (4.69) that b is going to be smaller than b' for most cases, with the possible exception being for cases when R_c or ρ_c' is negative. The angular beam width BW_θ, given by (4.34) is inversely proportional to b. What this means is that the a GB will usually become more divergent upon reflection from a curved surface. Therefore, the farther a GB propagates inside a curved waveguide cavity, the more it will diverge and the more likely it will become too large to fit nicely inside the cavity and satisfy the restrictions of the axial beam tracing approximation. This is what limits the length to width ratio of the waveguide cavities for which this method can be applied.

The approximations used above assumed that the incident beam illuminated an area confined to the vicinity of the reflection point Q. In reality, this condition may be difficult to achieve for the two cases mentioned earlier, namely, for GB's whose beam half-width at the point of reflection $w(z_0' + \rho_c')$ given by Equation (4.27) is comparable to the surface radius of curvature R_c, and for beams which come close to grazing the surface. If the beam illuminates too large an area of the surface, such as in the two cases mentioned above, the reflected field will no longer be Gaussian in nature. In most cases it may resemble a Gaussian beam, but it will probably be asymmetric to some extent.

Once the axis of a GB has been tracked to the termination via the axial approximation the fields of the beam in the presence of the waveguide walls in the termination plane must be found. If the beam is narrow enough and not close

138

to the waveguide walls at the termination, as shown in Figure 62, the fields are simply those of the GB basis function in free space. However, if the beam crosses the termination plane near a wall, the fields of the image beam should also be included, as shown in Figure 63.

4.5 Numerical Results and Discussion of the Gaussian Beam Shooting Method

In this section, some numerical results are presented which illustrate the use and accuracy of the axial Gaussian beam shooting and tracking method in comparison with other methods. All of the geometries included are made up of perfectly conducting surfaces.

Figures 64(a) and (b) are plots of the magnitude of the fields at a cross-section inside a semi-infinite parallel plate waveguide illuminated by a plane wave, perpendicular ($\perp$) and parallel ($\parallel$) polarization, respectively. Once again, perpendicular polarization means the E-field is normal to the plane of the page and parallel polarization means the H-field is normal to the plane of the page. For comparison, Figure 64 includes results found using the hybrid asymptotic high frequency modal method described in Chapter II. This method is considered sufficiently accurate to be used for reference solutions. Also shown in the figures is the GO ray tracing solution which is described Chapter III. As the plots show, the GO ray tracing solution is discontinuous due to shadowing effects of the GO field. The GB solution agrees nicely with the reference modal solution.

Figure 65 is a plot of the backscattered fields of an open-ended parallel plate waveguide cavity with a short circuit termination for $\perp$ polarization, found using the reciprocity integral formulation of Section 4.1 with Gaussian beams. In this and all subsequent plots, the scattering by the rim at the open end is included
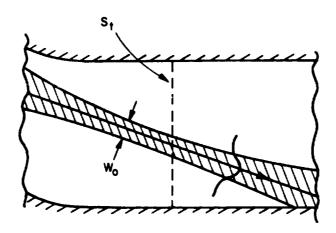
Figure 62: Gaussian beam crossing the plane of the termination inside a
waveguide cavity, away from the walls.
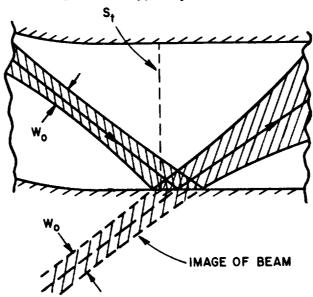
Figure 63: Gaussian beam crossing the plane of the termination inside a
waveguide cavity, near a wall.

in the calculations, and the wedge angle of the rim WA is zero. The figure also shows plots of the modal reference solution and the GO/AI ray tracing solution. The GB solution agrees nicely with the reference solution for all angles shown, while the GO/AI solution agrees well only for incidence angles within about 35° of of the guide axis. It is expected that the GB method should work very well for waveguide cavities with planar walls because the GB reflection from these walls is known exactly from image theory. It is the axial approximation used to find the reflection of GB's from curved walls (see Section 4.4) which introduces the most error in the GB tracing method.

Figures 66(a) and (b) are plots of the backscatter from an open-ended 2-D S-shaped waveguide cavity with a planar termination, $\perp$ and $\parallel$ polarizations, respectively. The cavity is made up of three uniform waveguide sections, two annular guides followed by a parallel plate guide, so the hybrid modal method is used as a reference solution. Each of the sections has an axial length of 5 wavelengths making the overall axial length 15 wavelengths giving a length to width ratio L/d of one. The GB solution used 7 sub-apertures ($M = 3$) and an angular increment $\Delta\theta$ of 7.69°. The beams covered an angular range of $\pm 60°$ making $N = 7$ and giving a total of 105 GB's. This choice allowed 3.5 beams per lobe (see Section 4.3 for a discussion). Using (4.45) and (4.28), the beam parameter is $b = 32.7\lambda$ and the beam waist width is $w_o = 6.45\lambda$. The particular choices of sub-aperture size and angular increment were determined by trial and error. The values were used which gave the minimum number of beams which reached the termination too wide to fit in the guide. As a general rule of thumb, it is best to choose parameters which give a beam waist width w_o in the open end which is less than half the width of the waveguide and an angular beam width BW_θ which is less than 10°. Ideally, both w_o and BW_θ should be as small as possible, but since

141

they are inversely proportional, a trade-off is necessary. For this relatively shallow cavity, the GB solution agrees very well with the modal reference solution.

Figures 67(a) and (b) are the same as Figures 66(a) and (b), respectively, except that the waveguide sections are now each 10 wavelengths long giving an overall L/d of two. Figures 68(a) and (b) are again the same as Figures 66(a) and (b), respectively, except that the waveguide sections are now each 15 wavelengths long giving an overall L/d of three. The results still agree quite well, but perhaps not as well as for the shallower $L/d = 1$ waveguide cavity.

Figures 69(a) and (b) are the same as Figures 68(a) and (b), respectively, but an additional parallel plate waveguide section of length 15 wavelengths has been inserted between the two annular sections giving an overall L/d of four. These figures show the GB solution is getting worse for longer guide lengths. This is due to the fact that the GB's diverge and get wider the farther in they go until they are too wide to fit inside the waveguide. However, because GB's become better focussed at higher frequencies, i.e., they stay narrow over longer propagation paths, the cavities which the GB tracing method can handle are determined by frequency as well as the axial length to width (L/d) ratio. Figure 70 is the same as Figure 69(a) except the frequency is doubled. For this plot 11 sub-apertures and an angular increment of 6.04° were used. It shows a much better agreement with the modal solution than Figure 69(a) does, as expected.

It was found from experience that a general rule of thumb for applying the GB tracing method is

$$L/d \;\; < \;\; \frac{1}{4}d/\lambda \qquad\qquad (4.70)$$

where d and L are the approximate waveguide cavity width and axial length, respectively and λ is the wavelength. This condition determines whether a particular

142

cavity can be analyzed using the GB tracing method at a given frequency. The inequality of (4.70) is only an approximation and it may be found that the GB method will work well for certain waveguide cavities which do not satisfy this condition. Two specific examples of this are parallel plate and rectangular waveguide cavities for which the GB tracing method will work for much larger L/d ratios than in (4.70). This is due to the fact that the planar surfaces of these guides do not change the rate of divergence of the GB's.

(a) ⊥ polarization

(b) ∥ polarization
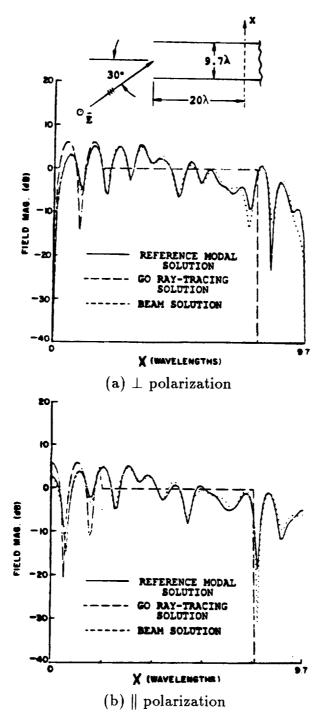
Figure 64: Fields at a cross-section inside a semi-infinite parallel plate waveguide illuminated by a plane wave

144
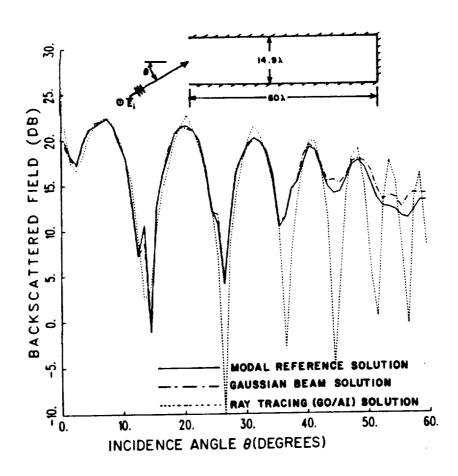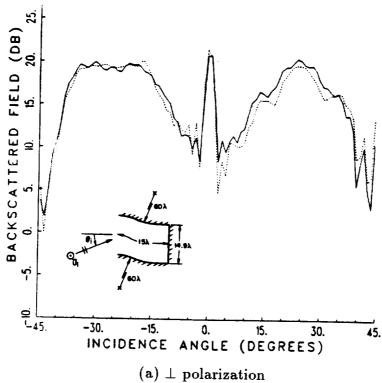
Figure 65: Backscatter pattern of an open-ended parallel plate waveguide cavity with a planar short circuit termination, ⊥ polarization.

145

(a) ⊥ polarization

(b) ∥ polarization
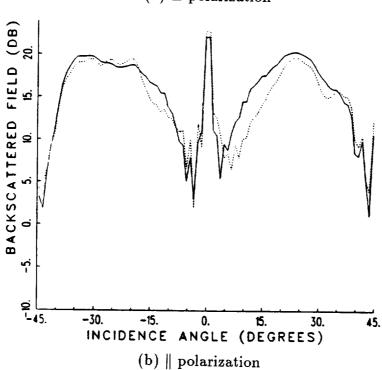
Figure 66: Backscatter from an open-ended 2-D S-shaped waveguide cavity with a planar termination, $L/d = 1$, 7 sub-apertures, $\Delta\theta = 7.69°$.

— hybrid modal solution, - - GB solution.

146

(a) ⊥ polarization

(b) ∥ polarization
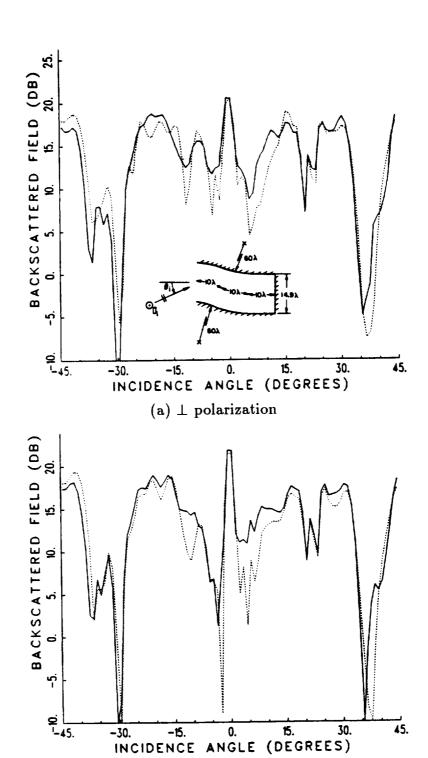
Figure 67: Backscatter from an open-ended 2-D S-shaped waveguide cavity with a planar termination, $L/d = 2$, 7 sub-apertures, $\Delta\theta = 7.69°$.

— hybrid modal solution, - - GB solution.

147

(a) $\perp$ polarization

(b) $\parallel$ polarization
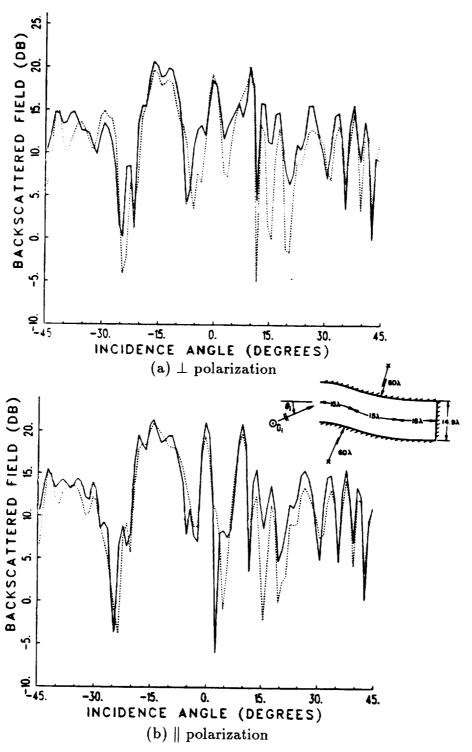
Figure 68: Backscatter from an open-ended 2-D S-shaped waveguide cavity with a planar termination, $L/d = 3$, 7 sub-apertures, $\Delta\theta = 7.69°$.

— hybrid modal solution, - -GB solution.

148

(a) $\perp$ polarization

(b) $\parallel$ polarization
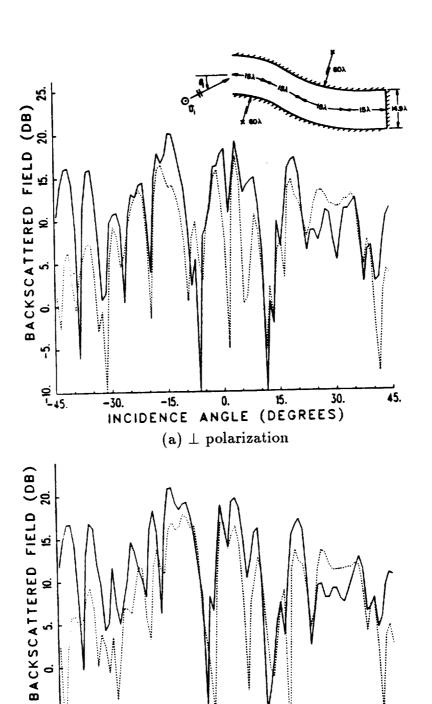
Figure 69: Backscatter from an open-ended 2-D S-shaped waveguide cavity with a planar termination, $L/d = 4$, 7 sub-apertures, $\Delta\theta = 7.69°$.

— hybrid modal solution, - - GB solution.

149
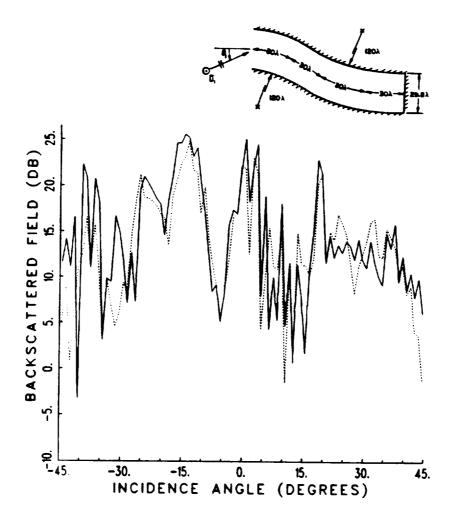
Figure 70: Backscatter from an open-ended 2-D S-shaped waveguide cavity with a planar termination, $L/d = 4$, $\perp$ polarization, 11 sub-apertures, $\Delta\theta = 6.04°$.

— hybrid modal solution, - - GB solution.

150

CHAPTER V

THE GENERALIZED RAY EXPANSION METHOD

The main limitation of the Gaussian beam (GB) shooting method of Chapter IV is that the well focussed GB's used tend to become too wide to fit well inside the waveguide cavity after a few reflections and as a result they sample a rather large portion of the cavity walls at subsequent reflections, thereby leading to a distortion of the beam from a true Gaussian shape after reflections. Hence, a generalized ray expansion (GRE) method is developed to retain many of the useful features of the GB shooting approach and at the same time to try and overcome the problems of beam distortion due to successive reflections in the later approach. In the GRE method, the rays are launched into the cavity from each sub-aperture as in Figure 7; this is done in a manner which is very similar to the launching of GB's form the sub-apertures as shown in Figure 6; but is different from that in the conventional GO or SBR approach. Thus, the field radiating from each sub-aperture in the GRE is expressed as a spherical wave which originates at the center of the sub-aperture and whose amplitude is determined via a far zone Kirchhoff approximation for the field radiated by that sub-aperture in the absence of the cavity walls. The portion of this spherical wave which enters the cavity is then tracked as an ordinary GO ray field within the interior via reflections at the cavity walls. In particular, a grid of ray-tubes are launched from the center of each sub-aperture to represent the spherical wave field which enters the cavity interior. These ray-tubes can be made

arbitrarily small to adequately sample the cavity geometry. Since the ray-optical field radiated by the sub-aperture is found via the Kirchhoff approximation, the GRE method therefore implicitly contains effects of waves diffracted into the cavity via the edges at the open end. This is in contrast to the GO ray shooting method of Chapter III which launches only the incident plane wave GO field directed into the cavity via a set of parallel incident ray-tubes and therefore does not contain such diffraction effects. In addition, the phase-space like array of ray-tubes in the GRE method is preset, as in the GB shooting method, so that the ray-tubes in the GRE need to be tracked only once within the cavity for a wide range of incidence angles, while the GO ray shooting method requires that a new grid of ray-tubes be traced every time the incidence angle changes. Consequently, the GRE method combines the versatility of the GO method with the rigor of the sub-aperture expansion method used in the GB approach, while overcoming most of the limitations of both. However, because the ray-tubes in the GRE method are of course tracked according to GO, they are prone to any caustic effects and cannot account for any diffraction effects within the cavity such as those arising from creeping waves on convex portions of the cavity walls. These effects should be minor for the smooth, slowly varying waveguide cavity geometries of interest. It is noted that while the GB's do not encounter caustics, the GB axial tracking procedure used in Chapter IV is more prone to errors than the well known GO ray tracing technique, especially for long waveguide cavity configurations.

The field scattered by the interior cavity termination can be found using either the termination reciprocity integral, or by an aperture integration over the fields of the ray-tubes which exit the aperture at the open end, as was done in Chapter III for the GO ray shooting method. Section 5.1 of this chapter will describe the manner in which the rays are launched in the GRE based on a knowledge of the

fields coupled through an aperture in the absence of the waveguide cavity, and the simplification that results for the case of planar sub-apertures and a locally planar incident field. Also in Section 5.1, one possible method will be presented for arranging the GRE in a cone-shaped angular grid of ray-tubes carrying equal power. Section 5.2 will discuss how the ray-tubes of the GRE propagate in the presence of the waveguide walls to the termination (or back to the open end) and Section 5.3 will derive the cavity scattered field from the ray-tube fields. In Section 5.4, the GRE method is applied to treat the case of an open-ended waveguide cavity with a rectangular aperture at the open end. Numerical results will be presented in Section 5.5.

5.1 The Generalized Ray Expansion (GRE) for the Fields Coupled through an Aperture

The GRE as described here constitutes a high frequency asymptotic method for finding the fields coupled through an aperture at the open end of a waveguide cavity, and the subsequent tracking of these fields through the interior cavity region. The GRE method expands the fields coupled through an aperture via a superposition of the fields radiated by a suitable array of sub-apertures which make up the aperture. The use of sub-apertures allows one to calculate the fields within the near zone of the original aperture in a ray-optical (spherical wave) form by employing a far zone Kirchhoff approximation for the fields radiated (i.e., transmitted) through each sub-aperture with the cavity walls absent. The ray-optical (spherical wave) fields launched from the coordinate center of each sub-aperture are then tracked via the laws of GO within the interior cavity region. Figure 71 shows an example of the aperture of an open-ended waveguide cavity divided up into N sub-apertures. The figure also shows the relative coordinate origin of each

153
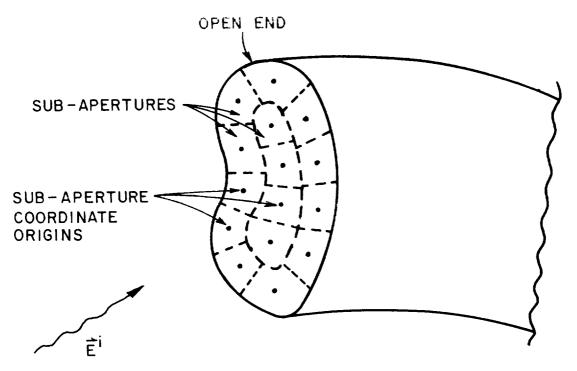
Figure 71: Aperture of an open-ended waveguide cavity divided up into N sub-apertures.

sub-aperture and an arbitrary incident field. Throughout this chapter, the electric (E) field will mainly be dealt with. The magnetic (H) field can be easily derived from the E-field using the Maxwell's equation

$$\vec{H} = \frac{-1}{jkZ_o}\nabla \times \vec{E}.$$ (5.1)

For ray-optic fields (5.1) reduces to

$$\vec{H} = \frac{1}{Z_o}\hat{k} \times \vec{E}$$ (5.2)

where

Z_o = free space impedance ($\approx 377\Omega$),

k = free space wavenumber ($= 2\pi/\lambda$),

λ = free space wavelength,

$\hat{k}$ = unit vector pointing in the direction of propagation.

154

The fields radiated into the cavity by the sub-apertures are well approximated using the fields due to the familiar physical optics (PO) based equivalent electric and magnetic sources $\vec{J}_s$ and $\vec{M}_s$ in the aperture, respectively, which are derived from the incident fields as [32]

$$\vec{M}_s = \vec{E}_i \times \hat{n} \qquad (5.3)$$

$$\vec{J}_s = -\vec{H}_i \times \hat{n} \qquad (5.4)$$

where

$\hat{n}$ = unit surface normal of the aperture pointing into the waveguide cavity.

The fields transmitted or propagated into the cavity beyond the aperture can be written as a sum of the fields which are radiated by each of the N sub-apertures,

$$\vec{E}(P_c) = \sum_{n=1}^{N} \vec{E}_n(P_c) \qquad (5.5)$$

where

$\vec{E}_n(P_c)$ = field from the nth sub-aperture at a point P_c inside the cavity,

provided P_c is in the far zone of the nth sub-aperture.

To find the field $\vec{E}_n(P_c)$ the PO based far zone field radiated by the nth sub-aperture is first found in the absence of the waveguide walls. This far zone $\vec{E}_n(P_c)$ is a spherical wave with its phase center located at the relative coordinate origin of the nth sub-aperture; also, this $\vec{E}_n(P_c)$ has some pattern to it. The field radiated by the sub-aperture is then associated with a cone-shaped angular grid of ray-tubes with constant amplitude originating at the relative coordinate origin of the sub-aperture, with each ray-tube amplitude weighted according to the pattern function. These rays can then be traced from the sub-aperture origin via the laws of geometrical optics (GO), but now in the presence of the waveguide walls. This is the basis of the GRE method.
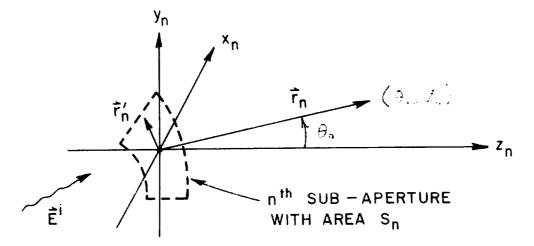
Figure 72: Geometry and coordinate system of the nth sub-aperture illuminated by $\vec{E}_i$.

5.1.1 Far zone fields of the nth sub-aperture.

Figure 72 shows the geometry of the nth sub-aperture and its relative coordinate system, illuminated by $\vec{E}_i$. The sub-aperture has surface area S_n. The far zone field radiated by the nth sub-aperture in the absence of the waveguide walls, derived using the PO based equivalent electric and magnetic surface currents of (5.3) and (5.4) is

$$
\vec{E}_n(\vec{r}_n) = -\frac{jk}{4\pi}\frac{e^{-jkr_n}}{r_n}\left\{\int\int_{S_n}\hat{r}_n\times\left[\hat{s}'_n\times\vec{E}_i(\vec{r}'_n)\right]e^{jk\vec{r}'_n\cdot\hat{r}_n}dS'\right.
$$
$$
\left.-Z_o\hat{r}_n\times\int\int_{S_n}\hat{r}_n\times\left[\hat{s}'_n\times\vec{H}_i(\vec{r}'_n)\right]e^{jk\vec{r}'_n\cdot\hat{r}_n}dS'\right\} \tag{5.6}
$$

where

$\vec{r}_n$ = vector to the observer from the coordinate origin of the nth

        sub-aperture ($\vec{r}_n = \hat{r}_n r_n$),

$\vec{r}'_n$ = vector to a source point in the sub-aperture,

$\hat{s}'_n$ = unit surface normal vector (at a source point) pointing into the cavity,

and the integration is over the primed source points in the sub-aperture. It is noted that $\vec{E}_i(\vec{r}_n')$ and $\vec{H}_i(\vec{r}_n')$ in (5.6) are the incident fields in the sub-aperture in the absence of the cavity walls, as in the Kirchhoff approximation. A more accurate result could be obtained by including the first order diffracted field in $\vec{E}_i(\vec{r}_n')$ and $\vec{H}_i(\vec{r}_n')$, due to the presence of the rim at the open end of the cavity. However, this would add unnecessary complexity to the analysis of practical geometries, so this diffracted field is usually not included.

The far zone criterion required to use (5.6) is

$$r_n \;>\; 2\frac{L_n^2}{\lambda} \tag{5.7}$$

where

$$L_n \;=\; \text{maximum linear dimension of the sub-aperture,}$$

which is the familiar far zone definition encountered in antenna problems. As will be shown later, this requirement is very conservative; (5.7) is roughly twice as large as is necessary.

Equation (5.6) has the form

$$\vec{E}_n(\vec{r}_n) \;=\; \frac{e^{-jkr_n}}{\sqrt{2}r_n}\vec{F}_n(\hat{r}_n,\vec{E}_i) \tag{5.8}$$

where the vector far zone pattern function $\vec{F}_n$ is given by

$$\begin{aligned}
\vec{F}_n(\hat{r}_n,\vec{E}_i) \;=\; & -\frac{jk}{4\pi}\sqrt{2}\left\{ \int\!\!\int_{S_n} \hat{r}_n \times \left[\hat{s}_n' \times \vec{E}_i(\vec{r}_n')\right] e^{jk\vec{r}_n'\cdot\hat{r}_n}dS' \right. \\
& \left. -Z_o\hat{r}_n \times \int\!\!\int_{S_n} \hat{r}_n \times \left[\hat{s}_n' \times \vec{H}_i(\vec{r}_n')\right] e^{jk\vec{r}_n'\cdot\hat{r}_n}dS' \right\}
\end{aligned} \tag{5.9}$$

The factor of $\sqrt{2}$ is introduced in (5.8) and (5.9) for power normalization reasons which will become clear in Section 5.2. Note that $\vec{F}_n(\hat{r}_n,\vec{E}_i)$ depends only on the incident field and the direction of observation, and not the distance to the observer.

Using (5.1) or (5.2), (5.9) can be evaluated numerically for any arbitrary known incident field, or it can be evaluated in closed form for some simple cases such as plane wave incidence.

In general, since (5.8) and (5.9) represent far zone radiated fields, (5.9) can always be decomposed into its $\hat{\theta}_n$ and $\hat{\phi}_n$ polarizations, i.e.,

$$\vec{F}_n(\hat{r}_n, \vec{E}_i) = \hat{\theta}_n F_{\theta_n}(\hat{r}_n, \vec{E}_i) + \hat{\phi}_n F_{\phi_n}(\hat{r}_n, \vec{E}_i). \tag{5.10}$$

Therefore, if the ray-tubes in the GRE are traced for both polarizations, the relative weighting of the amplitude of the ray-tubes can be found using (5.10).

5.1.2 Initial values for the launching of the ray-tube fields from the nth sub-aperture.

The far zone spherical wave fields of the nth sub-aperture given by (5.8) and (5.9) which enter the cavity interior can be associated with an angular grid of closely spaced ray-tubes within a specified cone which have their focus at the coordinate origin of the sub-aperture. The rays that lie outside the chosen cone either contribute insignificantly to the interior cavity field because they undergo a significantly larger number of reflections at the cavity walls, or they do not enter the cavity at all and hence they must be ignored. Additional reasons for ignoring these rays are given later on. As stated earlier, the relative amplitude of a ray-tube launched by the nth sub-aperture is determined by the value of the pattern function evaluated in the direction of the central ray of the ray-tube. Therefore, the radiated pattern of the sub-aperture which is included within the specified cone is approximated in a staircase fashion by the ray-tubes. Using (5.10), (5.8) can now be approximated as a sum over Q ray-tubes along which the fields of the

158

n^{th} sub-aperture are launched into the cavity interior. Thus,

$$\vec{E}_n(\vec{r}_n) = \sum_{q=1}^{Q} \vec{E}_n^q(\vec{r}_n) \qquad (5.11)$$

where

$$\vec{E}_n^q(\vec{r}_n) = F_{\theta_n}(\hat{r}_n^q, \vec{E}_i)\vec{B}_{\theta_n}^q(\vec{r}_n) + F_{\phi_n}(\hat{r}_n^q, \vec{E}_i)\vec{B}_{\phi_n}^q(\vec{r}_n) \qquad (5.12)$$

$$F_{\theta_n,\phi_n}(\hat{r}_n^q, \vec{E}_i) = F_{\theta_n,\phi_n}(\hat{r}_n, \vec{E}_i)\big|_{\hat{r}_n = \hat{r}_n^q} \qquad (5.13)$$

$\hat{r}_n^q$ = unit vector in the direction of the central ray of the

nq^{th} ray-tube.

$\vec{B}_{\theta_n}^q(\vec{r}_n)$ and $\vec{B}_{\phi_n}^q(\vec{r}_n)$ are the nq^{th} ray-tube functions in the expansion of (5.11) which are given by

$$\vec{B}_{\theta_n,\phi_n}^q(\vec{r}_n) = \begin{cases} (\hat{\theta}_n^q, \hat{\phi}_n^q)\dfrac{e^{-jkr_n^q}}{\sqrt{2r_n^q}} & : \text{ for } |\theta_n - \theta_n^q| < \frac{1}{2}\Delta\theta_n^q, \\[2mm] & \quad |\phi_n - \phi_n^q| < \frac{1}{2}\Delta\phi_n^q \\[2mm] 0 & : \text{ elsewhere} \end{cases} \qquad (5.14)$$

where

(θ_n, ϕ_n) = observation direction

(θ_n^q, ϕ_n^q) = direction of the central ray of the nq^{th} ray-tube

$\Delta\theta_n^q, \Delta\phi_n^q$ = angular widths of the nq^{th} ray-tube (cross-sections of the

ray-tubes are approximately square).

Once again, the subscript n refers to the relative coordinate system of the nth sub-aperture. Notice that the qth ray-tube expansion function of (5.14) constitutes a spherically spreading field in the neighborhood of the $\hat{r}_n^q$ direction with its focus at the center of the sub-aperture (n^{th} coordinate origin) and with $\hat{\theta}_n^q$ and $\hat{\phi}_n^q$ polarizations. These expansion or basis functions can be tracked independently of

159
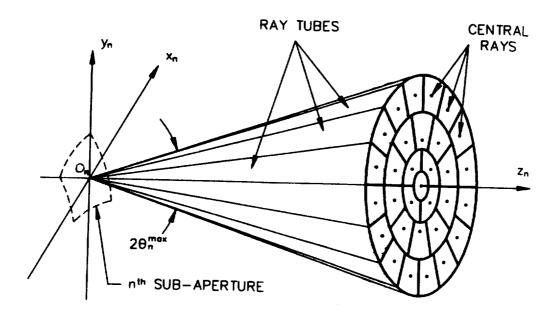
Figure 73: Ray-tubes within a cone of half-angle θ_n^{max} which are launched from the coordinate origin of the nth sub-aperture with the cavity walls absent.

the direction of the incident field because their excitation coefficients $F_{\theta_n}(\hat{r}_n^q, \vec{E}_i)$ and $F_{\phi_n}(\hat{r}_n^q, \vec{E}_i)$ contain all the information on the incident field.

Figure 73 shows how a typical ray-tube expansion within a specified cone might look in the absence of the waveguide cavity walls. Notice that the ray-tube expansion is truncated at some maximum angle θ_n^{max} which is less than $90°$. This is because it is not practical to track all of the ray-tubes filling the $z_n > 0$ half-space for the reasons cited earlier and also because the PO approximation used in (5.6) becomes less accurate for steep angles. Also, in practice steep incidence angles are not usually of interest so the ray-tubes at large θ_n^q angles will normally be very weakly excited, i.e., $F_{\theta_n}(\hat{r}_n^q, \vec{E}_i)$ and $F_{\phi_n}(\hat{r}_n^q, \vec{E}_i)$ will be small enough to neglect these ray-tubes.

The total fields radiated by the entire aperture in the absence of the waveguide

160

cavity walls can now be written as a sum over NQ ray-tubes as

$$\vec{E}(\vec{r}) \;=\; \sum_{n=1}^{N} \sum_{q=1}^{Q} \vec{E}_n^q(\vec{r}_n). \tag{5.15}$$

It should be mentioned here that the expansion of (5.15) is only valid subject to the sub-aperture far zone criterion of (5.7). Therefore, (5.15) is not valid for $r_n < 2L_n^2/\lambda$ for all n. However, if knowledge of the fields nearer to the aperture is required, the sub-aperture sizes can be made arbitrarily small so that the region of validity of (5.15) gets closer to the aperture.

5.1.3 Simplification for planar sub-apertures and a locally planar incident field

If the nth sub-aperture lies completely in a plane (the x_n-y_n plane, by definition) and the incident field is locally planar (or ray-optic), it is easy to extract the polarization components of (5.10) by manipulating the vector portions of (5.9). Also, the $\vec{H}_i$ field can be written in terms of $\vec{E}_i$ using (5.2). First, the E and H fields are each expressed as a unit polarization vector times a scalar:

$$\vec{E}_i(\vec{r}_n') \;=\; \hat{p}_e E_i(\vec{r}_n') \tag{5.16}$$

$$\vec{H}_i(\vec{r}_n') \;=\; \hat{p}_h H_i(\vec{r}_n') \;=\; \hat{p}_h \frac{E_i(\vec{r}_n')}{Z_o} \tag{5.17}$$

$$\hat{p}_h \;=\; \hat{k}_i \times \hat{p}_e \tag{5.18}$$

where

$\hat{p}_e \;=\;$ unit polarization vector of the incident E-field,

$\hat{p}_h \;=\;$ unit polarization vector of the incident H-field,

$\hat{k}_i \;=\;$ unit vector in the direction of propagation of the incident field.

The vector portions of (5.9) come out of the integrals so it can be written for this case, using (5.13) where $\vec{r}_n$ is replaced by the vector in the direction of the central

161

ray of the nq^{th} ray-tube $\vec{r}_n^q$, as

$$\vec{F}_n(\hat{r}_n^q, \vec{E}_i) = \{-\hat{r}_n^q \times (\hat{s}_n \times \hat{p}_e) + \hat{r}_n^q \times [\hat{r}_n^q \times (\hat{s}_n \times \hat{p}_h)]\} I(\hat{r}_n^q, E_i)$$

(5.19)

where

$$I(\hat{r}_n^q, E_i) = \frac{jk}{4\pi}\sqrt{2} \int\int_{S_n} E_i(\vec{r}_n')e^{jk\vec{r}_n'\cdot\hat{r}_n^q}dS'$$

(5.20)

$\hat{s}_n$ = unit surface normal of nth sub-aperture pointing into the cavity

(replaces $\hat{s}_n'$, which is not constant in general).

The vector portion of (5.19) can be decomposed into its $\hat{\theta}_n^q$ and $\hat{\phi}_n^q$ polarization components using the fact that $\hat{s}_n = \hat{z}_n$. This goes as follows, without including the tedious transformations between coordinate systems:

$$\hat{s}_n \times \hat{p}_e = \hat{z}_n \times (\hat{x}_n p_{ex_n} + \hat{y}_n p_{ey_n} + \hat{z}_n p_{ez_n})$$

$$= \hat{y}_n p_{ex_n} - \hat{x}_n p_{ey_n}$$

(5.21)

$$-\hat{r}_n^q \times (\hat{s}_n \times \hat{p}_e) = \hat{\theta}_n^q(p_{ex_n}\cos\phi_n^q + p_{ey_n}\sin\phi_n^q)$$

$$-\hat{\phi}_n^q(p_{ex_n}\sin\phi_n^q - p_{ey_n}\cos\phi_n^q)\cos\theta_n^q$$

(5.22)

$$\hat{r}_n^q \times [\hat{r}_n^q \times (\hat{s}_n \times \hat{p}_h)] = -\hat{\theta}_n^q(p_{hx_n}\sin\phi_n^q - p_{hy_n}\cos\phi_n^q)\cos\theta_n^q$$

$$+\hat{\phi}_n^q(p_{hx_n}\cos\phi_n^q + p_{hy_n}\sin\phi_n^q)$$

(5.23)

where

$$p_{ex_n}, p_{ey_n} = \hat{x}_n \text{ and } \hat{y}_n \text{ components of } \hat{p}_e, \text{ respectively}$$

$$p_{hx_n}, p_{hy_n} = \hat{x}_n \text{ and } \hat{y}_n \text{ components of } \hat{p}_h, \text{ respectively.}$$

The components of the vector pattern function of (5.10) can now be written as

$$F_{\theta_n}(\hat{r}_n^q, \vec{E}_i) = [(p_{ex_n} + p_{hy_n}\cos\theta_n^q)\cos\phi_n^q$$

162

$$+(p_{ey_n} - p_{hx_n} \cos \theta_n^q) \sin \phi_n^q] I(\hat{r}_n^q, E_i) \tag{5.24}$$

$$F_{\phi_n}(\hat{r}_n^q, \vec{E}_i) = [(p_{ey_n} \cos \theta_n^q + p_{hx_n}) \cos \phi_n^q$$

$$+(-p_{ex_n} \cos \theta_n^q + p_{hy_n}) \sin \phi_n^q] I(\hat{r}_n^q, E_i). \tag{5.25}$$

Note that (5.24) and (5.25) depend on the $\hat{x}_n$ and $\hat{y}_n$ components of the incident field. This allows for easy decomposition of the incident field into horizontal $(\hat{x}_n)$ and vertical $(\hat{y}_n)$ polarization cases. (5.20), (5.24) and (5.25) will be used later in Section 5.4 for the special case of a plane wave incident on a waveguide cavity with a rectangular open end.

5.1.4 An angular grid of ray-tubes carrying equal power within the cone.

In this section a method is presented for setting up the angular grid of ray-tubes within the specified cone which represent the fields radiating from a sub-aperture into the cavity in the GRE approach described above. In the method described below, all the individual ray-tubes are chosen to carry the same power, or equivalently, they all have the same initial angular area, and the initial cross-sectional area of the ray-tubes is approximately square. Using (5.11), the fields radiating from the nth sub-aperture can be expanded as

$$\vec{E}_n(\vec{r}_n) = \sum_{p=0}^{P_n} \sum_{q=1}^{Q_n^p} \vec{E}_n^{pq}(\vec{r}_n) \tag{5.26}$$

where

$$\vec{E}_n^{pq}(\vec{r}_n) = F_{\theta_n}(\hat{r}_n^{pq}, \vec{E}_i) \vec{B}_{\theta_n}^{pq}(\vec{r}_n) + F_{\phi_n}(\hat{r}_n^{pq}, \vec{E}_i) \vec{B}_{\phi_n}^{pq}(\vec{r}_n). \tag{5.27}$$

The single summation of (5.11) over the index q has been replaced with an equivalent double summation over the indices pq, representing a summation over the θ_n^{pq} and ϕ_n^{pq} angles, respectively. p is the index of a given annular ring of ray-tubes

163

which make an angle $\theta_n^{pq} = \theta_n^p$ with the z_n axis (see Figure 74) and q is the index of a given ray-tube in that ring. Note that the inner summation limit Q_n^p may depend on p in (5.26). This is because the number of ray-tubes in a given annular ring of ray-tubes depends on the angle θ_n^p, as shown in Figure 74.

Once again, $(\theta_n^{pq}, \phi_n^{pq})$ is the direction of the central ray of the npq^{th} ray-tube. $F_{\theta_n, \phi_n}(\hat{r}_n^{pq}, \vec{E}_i)$ is given by (5.9), (5.10) and (5.13) evaluated in the $\hat{r}_n^{pq}$ direction, and $\vec{B}_{\theta_n, \phi_n}^{pq}(\vec{r}_n)$ is given by (5.14) with the superscript q replaced by pq, i.e., by

$$\vec{B}_{\theta_n, \phi_n}^{pq}(\vec{r}_n) = \begin{cases} (\hat{\theta}_n^{pq}, \hat{\phi}_n^{pq}) \dfrac{e^{-jkr_n^{pq}}}{\sqrt{2r_n^{pq}}} & : \text{ for } |\theta_n - \theta_n^{pq}| < \frac{1}{2}\Delta\theta_n^{pq}, \\ & \quad\quad |\phi_n - \phi_n^{pq}| < \frac{1}{2}\Delta\phi_n^{pq} \quad\quad (5.28) \\ 0 & : \text{ elsewhere} \end{cases}$$

where

$$\Delta\theta_n^{pq}, \Delta\phi_n^{pq} = \text{ angular widths of the } npq^{th} \text{ ray-tube which points in the}$$
$$(\theta_n^{pq}, \phi_n^{pq}) \text{ direction.}$$

Again, $\vec{E}_n(\vec{r}_n)$ of (5.26) represents the fields radiating from the nth sub-aperture in terms of a double summation of ray-tube basis functions incremented in θ_n and ϕ_n, which are the angular components of the relative spherical coordinates of the nth sub-aperture.

For consistency as well as convenience, we want the angular area (Ω) of all the ray-tubes to be the same, i.e.,

$$\Omega_n^{pq} = \Omega. \quad\quad (5.29)$$

It is also convenient if the angular width in the $\hat{\theta}_n$ direction of the ray-tubes is constant for all the ray-tubes:

$$\Delta\theta_n^{pq} = \Delta\theta \quad\quad (5.30)$$

164

and

$$\theta_n^{pq} \ = \ p\Delta\theta \ = \ \theta_n^p. \tag{5.31}$$

A convenient choice for the angular area of all the ray-tubes is then

$$\Omega \ = \ \Delta\theta^2. \tag{5.32}$$

It remains to find $\Delta\phi_n^{pq}$ and ϕ_n^{pq}. For a given θ_n^p, let $\Delta\phi_n^{pq}$ be constant:

$$\Delta\phi_n^{pq} \ = \ \Delta\phi^p \tag{5.33}$$

$$\phi_n^{pq} \ = \ q\Delta\phi^p. \tag{5.34}$$

Also for a given θ_n^p, let there be an integral number of ray-tubes:

$$\Delta\phi^p \ = \ \frac{2\pi}{Q^p} \tag{5.35}$$

where

$$Q^p \ = \ \text{number of ray-tubes in a ring for a given } \theta_n^p,$$

as illustrated in Figure 74. Now the only thing left to find is Q^p. For a ring of Q^p ray-tubes at a given angle θ_n^p, as in Figure 74, the total angular area of the ring is given by

$$\begin{aligned} Q^p\Omega \ &= \ \int_0^{2\pi} \int_{\theta_n^p - \frac{1}{2}\Delta\theta}^{\theta_n^p + \frac{1}{2}\Delta\theta} \sin\theta d\theta d\phi \\ &= \ 4\pi \sin\left(\frac{1}{2}\Delta\theta\right) \sin\theta_n^p. \end{aligned} \tag{5.36}$$

For practical cases, $\Delta\theta$ is going to be very small so (5.36) can be written as

$$Q^p\Omega \ = \ 2\pi\Delta\theta \sin p\Delta\theta \tag{5.37}$$
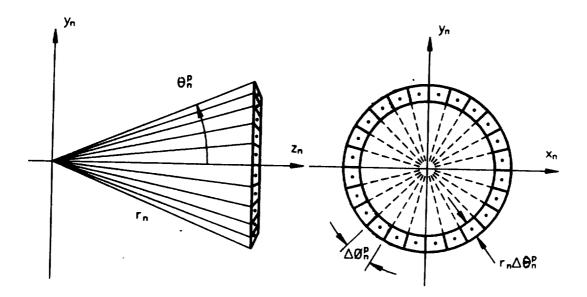
Figure 74: Ring of Q^p ray-tubes for a given θ_n^p.

where $p\Delta\theta$ has replaced θ_n^p using (5.31). Q^p can now be solved for using (5.32) and (5.37), along with the requirement that Q^p is an integer,

$$
\begin{aligned}
Q^p &= \text{Int}\left[\frac{2\pi\Delta\theta\sin p\Delta\theta}{\Omega}\right] \\
&= \text{Int}\left[\frac{2\pi\Delta\theta\sin p\Delta\theta}{\Delta\theta^2}\right] \\
&= \text{Int}\left[\frac{2\pi\sin p\Delta\theta}{\Delta\theta}\right]
\end{aligned}
\tag{5.38}
$$

where

$$
\text{Int}[x] = \text{nearest integer to } x. \tag{5.39}
$$

However, (5.38) is not correct for the special case of $p = 0$. Q^p should be 1 for this case, so (5.38) should be rewritten as

$$
Q^p = \begin{cases} \text{Int}\left[\frac{2\pi\sin p\Delta\theta}{\Delta\theta}\right] & : \text{ for } p > 0 \\ 1 & : \text{ for } p = 0. \end{cases} \tag{5.40}
$$

For the special case of $p = 0$, $\Delta\phi^p$ is 2π from (5.34). In other words, the axial ray-tube of a sub-aperture has a circular cross-section instead of square. This is

166
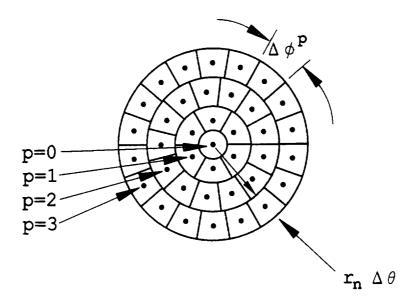
Figure 75: Cross-sections of the ray-tubes near the sub-aperture axis.

illustrated in Figure 75 which shows a nose-on view of how the cross-sections of the ray-tubes would look for the first few θ_n^p angles.

Because Q^p is an integer, the angular area of the npq^{th} ray-tube is not going to be exactly $\Delta\theta^2$, i.e., Equation (5.32) is not exact but is very nearly so. The exact angular area is given by

$$\Omega^p = \Delta\theta\Delta\phi^p \sin p\Delta\theta \tag{5.41}$$

which can be written as

$$\Omega^p = \begin{cases} \dfrac{2\pi\Delta\theta\sin p\Delta\theta}{\text{Int}\left[\frac{2\pi\sin p\Delta\theta}{\Delta\theta}\right]} & : \text{ for } p > 0 \\ \\ \frac{\pi}{4}\Delta\theta^2 & : \text{ for } p = 0 \end{cases} \tag{5.42}$$

using (5.35) and (5.40). The four worst cases, in order, are for $p = 0, 1, 2$ and 3, which are

$$\Omega^0 = \frac{\pi}{4}\Delta\theta^2 \approx 0.79\Omega \tag{5.43}$$

167

$$\Omega^1 = \frac{\pi}{3}\Delta\theta^2 \approx 1.05\Omega \tag{5.44}$$

$$\Omega^2 = \frac{4\pi}{13}\Delta\theta^2 \approx 0.97\Omega \tag{5.45}$$

$$\Omega^3 = \frac{6\pi}{19}\Delta\theta^2 \approx 0.99\Omega. \tag{5.46}$$

These four exact angular areas are close enough to Ω for practical purposes, considering that there will be a very large number of ray-tubes per sub-aperture. As (5.43)-(5.46) show, the difference decreases with increasing p.

In summary, the expansion of the fields of the nth sub-aperture into a cone-shaped angular grid of ray-tubes (5.27,5.28) is done by making $\Delta\theta_n^{pq}$ constant as in (5.30) and by requiring that the angular area of each ray-tube Ω_n^{pq} is also constant, as given by (5.32). The expansion is a double summation over P_n angles in θ_n, each with Q^p ray-tubes (5.40) with their central rays going in the $(\theta_n^p, \phi_n^{pq}) = (p\Delta\theta, q\Delta\phi^p)$ direction. Thus, the number of ray-tubes Q^p for a given θ_n^p, depends on p, as in (5.40). The maximum θ_n angle in the cone-shaped grid is $P_n\Delta\theta$. The cross-section of all the ray-tubes is approximately square, except for the $p = 0$ axial ray-tube which is circular, as shown in Figure 75.

5.2 Tracking the Generalized Ray Expansion (GRE) into the Interior Waveguide Cavity Region

In Section 5.1 the derivation was for a sub-aperture illuminated by an incident field in the absence of the waveguide cavity walls. To find the fields inside the cavity, the ray-tubes in the GRE representation of (5.15), which are launched from the coordinate centers of the sub-apertures, are allowed to propagate via the laws of GO to points inside the waveguide cavity. This is done using standard ray

tracing. The central ray of each ray-tube is traced from the coordinate origin of its sub-aperture to some cross-section within the cavity, or until it exits the cavity, via multiple reflections inside the cavity. The field of this central ray is assumed to represent the field across the ray-tube. The cross-sectional area of the ray-tube after each reflection at the cavity walls is found by conserving power in the ray-tube. If there is any power loss in the ray-tube due to reflections from non-perfectly conducting walls, this is not included in the power conservation, i.e., power is conserved by assuming a lossless cavity. As the initially square ray-tube undergoes reflections from curved surfaces, the cross-sectional shape of the ray-tube will become distorted. However, if the area of the ray-tube is kept to less than approximately $\left(\frac{1}{2}\lambda\right)^2$, then the exact shape of the cross-section is not important. So, any convenient shape can be used, such as a circle or square.

An efficient ray-tube tracing technique which uses curvature matrices is described in detail in Section 3.1.2 for the GO ray shooting method, and will not be repeated here. The only difference is that the ray-tubes in the GRE method are initially launched as diverging spherical waves originating at the coordinate origins of the sub-apertures, whereas the GO ray-tubes of Chapter III are launched as parallel, non-diverging ray-tubes representing the incident plane wave (these, too, will start diverging after reflection from a curved wall). Figures 3 and 7 illustrate the GO and GRE ray-tube launching schemes, respectively, for a 2-D geometry.

The fields at any point P_c inside the cavity can be written as a sum over NQ ray-tubes, similar to the summation of (5.15):

$$\vec{E}(P_c) \;=\; \sum_{n=1}^{N} \sum_{q=1}^{Q} \vec{E}_n^q(P_c) \tag{5.47}$$

where

$$\vec{E}_n^q(P_c) \;=\; F_{\theta_n}(\hat{r}_n^q, \vec{E}_i)\vec{B}_{\theta_n}^q(P_c) + F_{\phi_n}(\hat{r}_n^q, \vec{E}_i)\vec{B}_{\phi_n}^q(P_c) \tag{5.48}$$

169

$\vec{B}^q_{\theta_n,\phi_n}(P_c)$ = vector ray-tube basis function at a point P_c inside the

cavity which was initially $\hat{\theta}_n, \hat{\phi}_n$ polarized.

The expansion coefficients $F_{\theta_n,\phi_n}(\hat{r}^q_n, \vec{E}_i)$ are found from (5.9), (5.10) and (5.13) for the general case. The vector ray-tube basis functions of (5.48) were originally given by (5.14) before they were launched into the cavity. These ray-tubes were launched from the coordinate origin of the nth sub-aperture in the $\hat{r}^q_n$ direction and traced via GO to some cross-section inside the cavity containing P_c. Note that both polarizations can traced simultaneously because their GO ray paths will be identical. All polarization relevant information will be accounted for using the dyadic reflection coefficient of (3.16) for each reflection.

The cross-sectional area $A^q_n(P_c)$ of the nq^{th} ray-tube at P_c is again found by conserving power in the ray-tube, without wall loss. Using the ray-tube field of (5.12) along with (5.13) and (5.14), in the absence of the waveguide cavity walls, the input power of the nq^{th} ray-tube is given by

$$
\begin{aligned}
(\text{input power})^q_n &= \int_{\Omega^q_n} \left| \vec{E}^q_n(\vec{r}_n) \right|^2 r^2_n d\Omega \\
&= \int_{\Omega^q_n} \left| \hat{\theta}_n F_{\theta_n}(\hat{r}^q_n, \vec{E}_i) + \hat{\phi}_n F_{\phi_n}(\hat{r}^q_n, \vec{E}_i) \right|^2 \left| \frac{e^{-jkr_n}}{\sqrt{2}r_n} \right|^2 r^2_n d\Omega \\
&= \frac{1}{2} \left[\left| F_{\theta_n}(\hat{r}^q_n, \vec{E}_i) \right|^2 + \left| F_{\phi_n}(\hat{r}^q_n, \vec{E}_i) \right|^2 \right] \Omega^q_n \quad (5.49)
\end{aligned}
$$

where

Ω^q_n = beam solid angle of the nq^{th} ray-tube when it is launched.

Since the ray-tubes are tracked independently of the excitation, the cross-sectional area $A^q_n(P_c)$ can be found for arbitrary $F_{\theta_n,\phi_n}(\hat{r}^q_n, \vec{E}_i)$. Therefore, it is convenient to choose the excitation

$$
F_{\theta_n}(\hat{r}^q_n, \vec{E}_i) = F_{\phi_n}(\hat{r}^q_n, \vec{E}_i) = 1 \quad (5.50)
$$

which makes the input power of the nq^{th} ray-tube simply

$$(\text{input power})^q_n = \Omega^q_n.$$

(5.51)

This explains why the normalization factor of $\sqrt{2}$ was introduced back in (5.8) and (5.9) of Section 5.5.1.

The output power of the nq^{th} ray-tube at some point P_c is given by

$$(\text{output power})^q_n = \left|\vec{E}^{q,ll}_n(P_c)\right|^2 A^q_n(P_c)$$

(5.52)

where

$$\vec{E}^{q,ll}_n(P_c) = \text{electric field of the } nq^{th} \text{ ray-tube at a point } P_c \text{ due to the}$$

$$\text{unit excitation of (5.50), without wall loss.}$$

Equating (5.51) and (5.52) yields the ray-tube cross-sectional area at P_c to be

$$A^q_n(P_c) = \frac{\Omega^q_n}{\left|\vec{E}^{q,ll}_n(P_c)\right|^2}.$$

(5.53)

This cross-sectional area along with the fields of the central ray completely define the ray-tube at any point P_c if $A^q_n(P_c)$ is less than $\left(\frac{1}{2}\lambda\right)^2$, as mentioned earlier. This is because the exact shape of the ray-tube can then be chosen arbitrarily as some convenient axially symmetric geometry such as a circle or square. If it is found that a ray-tube has a cross-sectional area greater than $\left(\frac{1}{2}\lambda\right)^2$ at P_c, it is more efficient to sub-divide and re-launch that ray-tube rather than re-launching a whole new denser grid of ray-tubes. This was also discussed in 3.2 for the GO method. It is this capability which gives the GRE method an advantage over the Gaussian beam shooting method for cavities with larger length-to-width ratios, because GB's cannot be sub-divided into arbitrarily narrow beams like the ray-tubes can.

171

Note that (5.53) is only valid subject to the constraint of (5.50) (unit excitation). In practice, the ray-tubes would be traced with the unit excitation of (5.50) and their cross-sectional areas would be found from (5.53) before the incident field is varied via the excitation coefficients in (5.48). This is a very useful property of the GRE method because the array of ray-tubes need to be traced only once for a wide range of incident fields (i.e., for all incident fields which lie within the angular region covered by the GRE grid).

To summarize the GRE method described so far, the open end of the waveguide cavity is divided up into N sub-apertures and for each sub-aperture a cone-shaped grid of Q ray-tubes is defined, with each ray-tube originating at the relative coordinate origin of the sub-aperture. The fields at a point inside the cavity are then expanded as a sum of the fields of all the ray-tubes of all the sub-apertures as in (5.47) and (5.48). The expansion coefficients of (5.48) are related to the incident field and the direction of the ray-tube and are given by (5.9), (5.10) and (5.13). The ray-tubes are tracked only once (independent of the incident angle) via geometrical optics (GO) along the central ray which is launched in the (θ_n^q, ϕ_n^q) direction; only the initial amplitudes (expansion coefficients) are changed but not the ray directions with changes in the incidence angle. The area of the ray-tube after undergoing multiple reflections is found by conserving power (without loss) and is given by (5.53). The field is assumed constant across a ray-tube and the shape of a cross-section of a ray-tube can be chosen arbitrarily (as long as it is approximately axially symmetric) if the area of the ray-tube is kept to less than about $\left(\frac{1}{2}\lambda\right)^2$.

5.3 Obtaining the Cavity Scattered Field from the GRE Fields Inside the Cavity

As in the GO ray shooting method of Chapter III, one of two integral methods are normally used to find the fields scattered by the cavity using the GRE fields. The first of these is the aperture integration method, referred to as GRE/AI, and the second is a termination reciprocity integral method referred to as GRE/RI. The main difference between the two is that in the GRE/AI method, the ray-tubes are traced within the cavity to the termination and back until they exit through the aperture at the open end where they are integrated, and in the GRE/RI method they are traced within the cavity until they reach some conveniently located cross-section near the termination of the cavity where they are reacted via a reciprocity integral formulation with all the other ray-tubes. However, in general, the GRE/RI method also requires the use of an aperture integration because some ray-tubes will never reach the termination but will exit through the open end. The main advantage of the GRE/RI over the GRE/AI method is that complex terminations can be included in the former approach; the latter can handle only simple terminations such as a planar one. Of course, the GRE/RI requires one to be able to characterize the EM termination reflection properties; this was also discussed in Section 3.2.

Because the methods of obtaining the cavity scattered fields in the GRE/AI and GRE/RI methods are so similar to the GO/AI and GO/RI methods of Section 3.2, many of the equations of that section will be referenced but not repeated here. Therefore, as in Section 3.2, the far-field bistatic scattered field is found here for the case of incident plane wave excitation in this section. However, unlike the GO method, the GRE method is not restricted to plane wave incidence and could be extended to arbitrary excitations by adjusting the expansion coefficients

$F_{\theta_n}(\hat{r}_n^q, \vec{E}_i)$ and $F_{\phi_n}(\hat{r}_n^q, \vec{E}_i)$ of (5.48) in a straightforward manner. Therefore, the GRE method is not limited to any particular incident field, as long as it originates outside the waveguide cavity.

5.3.1 GRE combined with aperture integration (GRE/AI).

The desired contribution to the field scattered by the waveguide cavity $\vec{E}^s$ is given by (3.24); this includes only the scattering by the rim at the open end and the interior of the cavity, and no other external scattering mechanisms for reasons mentioned previously. The rim scattered field $\vec{E}^{sr}$ is found using GTD and ECM in Chapter II, and is given by Equations (2.21) thru (2.24). In the GRE/AI method, the cavity scattered field is given as in (3.25) by

$$\vec{E}^{sc} = \sum_{m=1}^{M} \vec{E}_m^{sc} \qquad (5.54)$$

where

M = number of ray-tubes which exit the cavity through the open end,

$\vec{E}_m^{sc}$ = field radiated by the mth ray-tube which exits the open end

after reflecting from a simple interior cavity termination.

Note that the sum in (5.54) is over all the ray-tubes from all of the sub-apertures which have been traced throughout the cavity and which exit through the open end. The cavity scattering contribution of each of these ray-tubes $\vec{E}_m^{sc}$ is given by (3.26) and (3.27), with the n subscripts replaced by m (this is to avoid confusing the sum over ray-tubes with the sum over sub-apertures, which used the subscript n earlier in this chapter).

If the ray-tube cross-sectional area A_m is less than $\left(\frac{1}{2}\lambda\right)^2$, then the shape function of (3.27) can be replaced by (3.30) or (3.32), which are shape independent.

174

This cross-sectional area is given by (5.53) with the indices n and q replaced by the single index m, which covers all the ray-tubes of all the all sub-apertures, which exit through the open end.

5.3.2 GRE combined with the termination reciprocity integral (GRE/RI).

The GRE/RI method is exactly the same as the GO/RI method described in Section 3.2.2, with the only difference being in the way the ray-tubes are launched and their cross-sectional areas found. This was also the case for the GRE/AI method of the last section, for which the important differences were described. Therefore, it is assumed that the reader can infer the GRE/RI method from a close examination of the GO/RI method of Section 3.2.2 and the GRE/AI method of Section 5.3.1, so the details will not be repeated here. Simply put, the fields of the GRE expansion of (5.47) and (5.48) are used in the termination reciprocity integral (3.36), which is described in Appendix C. However, the modal form of the reciprocity integral (3.44) is most often used in practice. The integration is over all the points P_c in a cross-section near the termination. The bistatic radar cross-section (RCS) is then obtained from the termination reciprocity integral as described in Section 3.2.2 and given by (3.43). It is of course assumed that the EM reflection properties of the complex interior cavity termination are known.

5.4 Generalized Ray Expansion for an Open-Ended Cavity with a Rectangular Aperture

In this section the GRE method as described so far is applied to the special case of a waveguide cavity with a rectangular aperture (at the open end) which is illuminated by an externally incident plane wave field. The equations of Section 5.1.3 for planar sub-apertures and a locally planar incident field along with the equations of Section 5.1.4 for the cone-shaped angular grid of ray-tubes carrying

175
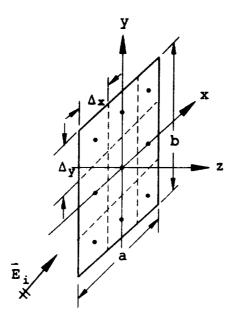
Figure 76: Geometry of a rectangular aperture divided up into rectangular sub-apertures illuminated by a plane wave.

equal power will be used to illustrate the use of the GRE method so that it can be understood well enough to be extended to more complicated geometries and incident fields.

Figure 76 shows the geometry of the rectangular aperture in the absence of the waveguide cavity walls, illuminated by a plane wave incident from the (θ_i, ϕ_i) direction, where θ_i is measured from the $-z$ axis of the figure. As shown in the figure, the aperture is divided up into identical rectangular sub-apertures with dimensions Δ_x and Δ_y given by

$$\Delta_x = \frac{a}{2M+1} \tag{5.55}$$

$$\Delta_y = \frac{b}{2N+1} \tag{5.56}$$

where

$$a, b = x,y \text{ dimensions of the aperture, respectively,}$$

$$2M + 1 \quad = \quad \text{number of sub-apertures in the } x \text{ direction,}$$

$$2N + 1 \quad = \quad \text{number of sub-apertures in the } y \text{ direction.}$$

For the aperture shown in Figure 76, $M = N = 1$ and there are a total of $(2M + 1)(2N + 1) = 9$ sub-apertures making up the rectangular aperture. The figure also shows the relative coordinate origins of each sub-aperture.

The fields radiating from the aperture can be expanded similarly to (5.15) as a sum over all of the ray-tubes which point in the $\hat{r}_{mn}^{pq}$ directions:

$$\vec{E}_{aper}(\vec{r}) \quad = \quad \sum_{m=-M}^{M} \sum_{n=-N}^{N} \sum_{p=0}^{P} \sum_{q=1}^{Q^p} \vec{E}_{mn}^{pq}(\vec{r}_{mn}) \tag{5.57}$$

where, as in (5.12) or (5.27),

$$\vec{E}_{mn}^{pq}(\vec{r}_{mn}) \quad = \quad F_{\theta_{mn}}(\hat{r}_{mn}^{pq}, \vec{E}_i)\vec{B}_{\theta_{mn}}^{pq}(\vec{r}_{mn}) + F_{\phi_{mn}}(\hat{r}_{mn}^{pq}, \vec{E}_i)\vec{B}_{\phi_{mn}}^{pq}(\vec{r}_{mn}).$$
$$\tag{5.58}$$

Throughout this section, the subscript indices m and n designate the mn^{th} sub-aperture and the superscript indices p and q designate the pq^{th} ray-tube of the mn^{th} sub-aperture. So, $\vec{r}_{mn}^{pq}$ originates at the center of the mn^{th} sub-aperture and points in the $(\theta_{mn}^{pq}, \phi_{mn}^{pq})$ direction. x_m and y_n are the relative coordinates of the mn^{th} sub-aperture and are given by

$$x_m \quad = \quad x - m\Delta_x \tag{5.59}$$

$$y_n \quad = \quad y - n\Delta_y, \tag{5.60}$$

as can be deduced from Figure 76.

$\vec{B}_{\theta_{mn}, \phi_{mn}}^{pq}(\vec{r}_{mn})$ are the vector ray-tube basis functions as in (5.14) or (5.28)

given by

$$
\vec{B}^{pq}_{\theta_{mn},\phi_{mn}}(\vec{r}_{mn}) = \begin{cases} (\hat{\theta}^{pq}_{mn}, \hat{\phi}^{pq}_{mn}) \dfrac{e^{-jkr^{pq}_{mn}}}{\sqrt{2}r^{pq}_{mn}} & : \text{ for } |\theta_{mn} - \theta^{pq}_{mn}| < \frac{1}{2}\Delta\theta^{pq}_{mn}, \\ & \qquad |\phi_{mn} - \phi^{pq}_{mn}| < \frac{1}{2}\Delta\phi^{pq}_{mn} \quad (5.61) \\ 0 & : \text{ elsewhere} \end{cases}
$$

where

$$
\Delta\theta^{pq}_{mn} = \Delta\theta \tag{5.62}
$$

$$
\theta^{pq}_{mn} = \theta^p_{mn} = p\Delta\theta \tag{5.63}
$$

$$
\Delta\phi^{pq}_{mn} = \Delta\phi^p = \frac{2\pi}{Q^p} \tag{5.64}
$$

$$
\phi^{pq}_{mn} = q\Delta\phi^p \tag{5.65}
$$

$$
Q^p = \begin{cases} \text{Int}\left[\dfrac{2\pi\sin p\Delta\theta}{\Delta\theta}\right] & : \text{ for } p \neq 0 \\ 1 & : \text{ elsewhere} \end{cases} \tag{5.66}
$$

as in (5.30), (5.31), (5.33), (5.35), (5.34) and (5.40). Simply put, (5.62)-(5.66) mean that the angular ray-tube width $\Delta\theta$ in the $\hat{\theta}$ direction is constant for all the cone-shaped angular grids of ray-tubes, the angular width $\Delta\phi^p$ in the $\hat{\phi}$ direction is constant for a given p and there are Q^p ray-tubes for a given p. The vector ray-tube pulse basis function of Equation (5.61) implies that the field of the $mnpq^{th}$ ray-tube is a spherical wave originating at the coordinate origin of the mn^{th} sub-aperture if the observation direction (θ_{mn}, ϕ_{mn}) is within the $mnpq^{th}$ ray-tube; otherwise it is zero. The $mnpq^{th}$ ray-tube points in the $\hat{r}^{pq}_{mn}$ direction, i.e., towards $(\theta^{pq}_{mn}, \phi^{pq}_{mn})$.

The expansion coefficients in (5.58) are given by

$$
\begin{aligned}
F_{\theta_{mn}}(\hat{r}^{pq}_{mn}, \vec{E}_i) = & \left[(p_{ex} + p_{hy}\cos\theta^{pq}_{mn})\cos\phi^{pq}_{mn} \right. \\
& \left. + (p_{ey} - p_{hx}\cos\theta^{pq}_{mn})\sin\phi^{pq}_{mn})\right] I_{mn}(\hat{r}^{pq}_{mn}, E_i)
\end{aligned}
$$

$$\tag{5.67}$$

$$
F_{\phi_{mn}}(\hat{r}^{pq}_{mn}, \vec{E}_i) = \left[(p_{ey}\cos\theta^{pq}_{mn} + p_{hx})\cos\phi^{pq}_{mn} \right.
$$

178

$$+(-p_{ex}\cos\theta_{mn}^{pq} + p_{hy})\sin\phi_{mn}^{pq}\big]\, I_{mn}(\hat{r}_{mn}^{pq}, E_i)$$

$$(5.68)$$

where

$$p_{ex}, p_{ey} = \hat{x}, \hat{y} \text{ components of the unit polarization vector } \hat{p}_e \text{ of the}$$

$$\text{incident } E\text{-field,}$$

$$p_{hx}, p_{hy} = \hat{x}, \hat{y} \text{ components of the unit polarization vector } \hat{p}_h \text{ of the}$$

$$\text{incident } H\text{-field,}$$

and $I_{mn}(\hat{r}_{mn}^{pq}, E_i)$ is the radiation integral over the fields in the sub-aperture evaluated in the direction $\hat{r}_{mn}^{pq}$ given by

$$I_{mn}(\hat{r}_{mn}^{pq}, E_i) = \frac{jk}{4\pi}\sqrt{2}\int_{-\frac{1}{2}\Delta_y}^{\frac{1}{2}\Delta_y}\int_{-\frac{1}{2}\Delta_x}^{\frac{1}{2}\Delta_x} E_i(x'_m, y'_n)e^{jk\vec{r}'_{mn}\cdot\hat{r}_{mn}^{pq}}dx'_m dy'_n$$

$$(5.69)$$

as in (5.24), (5.25) and (5.20), respectively. The plane wave incident field is given by

$$\vec{E}_i = \hat{p}_e E_o e^{-jk(z\cos\theta_i + x\sin\theta_i\cos\phi_i + y\sin\theta_i\sin\phi_i)}$$

$$(5.70)$$

where

$$E_o = \text{magnitude of the incident plane wave,}$$

$$(\theta_i, \phi_i) = \text{direction from which the incident plane wave originates, with}$$

$$\theta_i \text{ measured from the } -z \text{ axis.}$$

So, using (5.59) and (5.60), the scalar portion of the incident field in the plane of the mn^{th} sub-aperture ($z = 0$) is given by

$$E_i(x'_m, y'_n) = E_o e^{-jk(m\Delta_x\cos\phi_i + n\Delta_y\sin\phi_i)\sin\theta_i} e^{-jk(x'_m\cos\phi_i + y'_n\sin\phi_i)\sin\theta_i}.$$

$$(5.71)$$

179

It can be shown that the exponential term in the integrand of (5.69) is

$$\vec{r}_{mn}' \cdot \hat{r}_{mn}^{pq} = (x_m' \cos \phi_{mn}^{pq} + y_n' \sin \phi_{mn}^{pq}) \sin \theta_{mn}^{pq} \tag{5.72}$$

by decomposing $\vec{r}_{mn}'$ and $\hat{r}_{mn}^{pq}$ into their $(\hat{x}_n, \hat{y}_m, \hat{z})$ components.

Substituting (5.71) and (5.72) into (5.69) and integrating gives

$$
\begin{aligned}
I_{mn}(\hat{r}_{mn}^{pq}, E_i) = {} & \frac{jk}{4\pi}\sqrt{2}E_o\Delta_x\Delta_y e^{-jk(m\Delta_x \cos \phi_i \sin \theta_i + n\Delta_y \sin \phi_i \sin \theta_i)} \\
& \cdot \text{sinc}\left[\frac{1}{2}k\Delta_x(\cos \phi_{mn}^{pq} \sin \theta_{mn}^{pq} - \cos \phi_i \sin \theta_i)\right] \\
& \cdot \text{sinc}\left[\frac{1}{2}k\Delta_y(\sin \phi_{mn}^{pq} \sin \theta_{mn}^{pq} - \sin \phi_i \sin \theta_i)\right]
\end{aligned}
\tag{5.73}
$$

where

$$\text{sinc}[x] = \frac{\sin x}{x}, \tag{5.74}$$

which, along with (5.67) and (5.68), gives the $\hat{\theta}_{mn}$ and $\hat{\phi}_{mn}$ components of the expansion coefficients of (5.58).

The ray-tube basis functions can now be traced from their sub-aperture coordinate origins to points inside the waveguide cavity via the laws of geometrical optics (GO), as described in Section 5.2. The fields inside the cavity can be written as in (5.47) and (5.48) as

$$\vec{E}(P_c) = \sum_{m=-M}^{M} \sum_{n=-N}^{N} \sum_{p=0}^{P} \sum_{q=1}^{Q^p} \vec{E}_{mn}^{pq}(P_c) \tag{5.75}$$

$$\vec{E}_{mn}^{pq}(P_c) = F_{\theta_{mn}}(\hat{r}_{mn}^{pq}, \vec{E}_i)\vec{B}_{\theta_{mn}}^{pq}(P_c) + F_{\phi_{mn}}(\hat{r}_{mn}^{pq}, \vec{E}_i)\vec{B}_{\phi_{mn}}^{pq}(P_c)$$

$$\tag{5.76}$$

where $\vec{B}_{\theta_{mn}}^{pq}$ and $\vec{B}_{\phi_{mn}}^{pq}$ are the vector ray-tube basis functions for the initially $\hat{\theta}_{mn}$ and $\hat{\phi}_{mn}$ polarized $mnpq^{th}$ ray-tube, respectively, which have been traced inside the cavity to some cross-section containing P_c. The cross-sectional area of the

$mnpq^{th}$ ray-tube at P_c inside the cavity is given as in (5.53) by

$$A_{mn}^{pq}(P_c) = \frac{\Omega}{\left|\vec{E}_{mn}^{pq,ll}(P_c)\right|^2} \qquad (5.77)$$

where

$\vec{E}_{mn}^{pq,ll}(P_c) =$ electric field of the $mnpq^{th}$ ray-tube at P_c due to the unit

excitation of (5.50) without loss, as in (5.52),

$\Omega =$ initial beam solid angle of the ray-tubes.

For this example, the initial beam solid angle has been chosen to be constant for all ray-tubes, and is given by

$$\Omega = \Delta\theta^2 \qquad (5.78)$$

as in (5.32). It should be mentioned again that the exact shape of the ray-tube is not important if the area given by (5.77) is less than $(\frac{1}{2}\lambda)^2$, so the shape can be chosen arbitrarily. Also, if ray-tube sub-division is going to used to increase the efficiency of the ray tracing, then of course the beam solid angle Ω in (5.77) for a sub-divided ray-tube must also be sub-divided accordingly.

Both the $\hat{\theta}_{mn}$ and $\hat{\phi}_{mn}$ polarizations for each ray-tube should be traced, as the expansion of (5.57) and (5.58) indicates. However, as discussed in Section 5.3, both polarization can easily be traced simultaneously because they follow identical GO paths. Furthermore, all of the ray-tubes in the expansion of (5.57) need to be traced only once independent of incidence angle because the $\hat{r}_{mn}^{pq}$ directions of the ray-tubes do not change with the incidence angle. The effect of incidence angle is contained entirely in the expansion coefficients of (5.67) and (5.68). Therefore, once all the ray-tubes have been traced, the fields inside the waveguide cavity

can be found for any given incidence angle which is well within the angular range covered by the angular grids of ray-tubes, simply by adjusting (5.67) and (5.68).

Finally, it should be mentioned that the region of validity of the expansions of (5.57) and (5.75) is restricted by the sub-aperture far zone criterion of (5.7). For the rectangular aperture case the largest linear dimension of a sub-aperture is its diagonal length $\sqrt{\Delta_x^2 + \Delta_y^2}$ so the far field restriction is

$$r_{mn} > 2\frac{\Delta_x^2 + \Delta_y^2}{\lambda}, \quad \text{for all } mn. \tag{5.79}$$

This means that the fields inside the cavity given by (5.75) and (5.76) are not valid within a distance $2(\Delta_x^2 + \Delta_y^2)/\lambda$ of the aperture. However, the sub-aperture size can be reduced arbitrarily (with a corresponding increase in the number of sub-apertures) if the fields closer to the aperture are desired. Therefore, the sub-aperture size should be chosen to be small enough to obtain the fields at a desired distance from the open end. But on the other hand, the smaller the sub-aperture size, the more sub-apertures are necessary and therefore the more ray-tubes must be traced. For practical application, it is most efficient to make the sub-apertures as large as (5.79) permits. In practice it has been found that this criterion is somewhat more extreme than necessary. Numerical results will be presented in the next section for some 2-D cases which suggest that (5.79) is roughly twice as large as is actually required for acceptable accuracy.

5.5 Numerical Results and Discussion of the Generalized Ray Expansion Method

In this section, numerical results obtained using the GRE method will be presented for some 2-D straight (parallel-plate), curved (annular) and S-shaped (parallel-plate and annular) open-ended waveguide cavities. 3-D results have not

yet been obtained due to the complexity of the computer coding required for 3-D ray-tracing. Several groups are currently working on this task, so 3-D results should be forthcoming in the near future. These can be verified with realistic experimental results which are already available, and with results generated using the more predictive hybrid modal method of Chapter II. For now it is assumed that relevant principles of the GRE method are adequately represented in 2-D so that conclusions based on these more insightful 2-D results can be reached. This assumption is supported by the fact that the three basic components of the GRE method, i.e., the sub-aperture expansion, the GO ray-tube tracing and the termination reciprocity integral or aperture integration, all have straightforward correspondences between their 2-D and 3-D application.

In this section, "perpendicular" polarization ($\perp$) is for the case when the electric field is normal to the plane of incidence, i.e., perpendicular to the plane of the geometry or page, and "parallel" polarization ($\parallel$) is for the case when the electric field in parallel to the plane of incidence, i.e., the magnetic field is normal to the plane of the geometry. All the GRE results will be compared with a hybrid asymptotic modal reference solution, and in some cases the GO result will also be included.

Figure 77 shows the backscatter pattern of an open-ended parallel-plate waveguide with a planar short circuit termination. Three sub-apertures were used in the GRE result which makes the far field distance from the aperture 50λ using (5.7). This is the length of the waveguide of Figure 77, so the GRE/RI result agrees very well with the modal reference solution, as expected. It is noted that the computer code which generated the GRE/RI result used a ray-tube sub-division algorithm for ray-tubes which were larger than $\frac{1}{2}\lambda$ across when they reached the termination. Therefore, the total number of ray-tubes listed in the caption of Figure 77 (and

subsequent figures) does not refer to a fixed number of equally sized ray-tubes, but to the total number of ray-tubes that was required to satisfy the $\frac{1}{2}\lambda$ criterion using sub-division. This number will vary somewhat depending on the coding algorithm in use. Finally, for the $\pm 45°$ pattern of Figure 77 (and others) all ray-tubes within a range of $\pm 60°$ were traced for each sub-aperture.

Figure 78 shows a backscatter pattern for the same case as in Figure 77 except that the guide is 30λ long instead of 50λ, thus violating the condition of (5.7). Once again, the GRE/RI result agrees very well with the modal reference solution, suggesting that the condition of (5.7) is too stringent. The open-ended waveguide of Figure 79(a) pushes the far field condition even further with a length of 15λ, again using three sub-apertures. Here, the GRE/RI result begins to show noticeable deviation from the modal reference solution, even though the agreement is quite good for some incidence angles. From these results it is reasonable to conclude that the far field condition of (5.7) is about twice as much as is actually required in practice, and can be rewritten as

$$r_n \; > \; \frac{L_n^2}{\lambda}, \text{ for all } n, \tag{5.80}$$

to obtain reasonably accurate results more efficiently.

Figure 79(b) shows the same case as Figure 79(a), except that five sub-apertures are used instead of three. As expected, the agreement with the reference solution is quite good because the far field distance is 9λ, using the approximation of (5.80). Note that this five sub-aperture case of course required more total ray-tubes than the three sub-aperture case. Also note that, in general, the longer the waveguide the more ray-tubes are required because the ray-tubes are diverging.

Figures 80(a) and (b) show the backscatter patterns for an open-ended annular waveguide cavity with a planar short circuit termination, found using three and

184

five sub-apertures, respectively. Here, the effect of wall curvature is important and the differences between the three and five sub-aperture cases suggest how the radii of curvature of the two walls affect the choice of sub-aperture size. Although, as expected, the five sub-aperture result agrees better with the reference solution than the three sub-aperture result, the three sub-aperture result is still quite reasonable. This is an important result because it is difficult to prove analytically why it is allowable to launch ray-tubes from a sub-aperture which lies adjacent to a curved surface. The numerical results alone support the validity of this practice. In contrast, it can be proven that it is allowable to launch ray-tubes from a sub-aperture adjacent to a planar surface using image theory. So, it could be argued that the curved surface case becomes rigorous as the radius of curvature of the surface approaches infinity, and that most likely it is a very good approximation for finite curvatures that are much larger than the sub-aperture size. In any case, the numerical results thus far have supported the later argument for practical applications.

The geometry of Figure 80 reveals some further valuable insight into the mechanisms of the GRE method. Because the GRE method uses GO ray tracing, it is prone to some of the errors of GO field theory. The GRE method is rigorous for the open-ended parallel-plate waveguide due to image theory as discussed above. However, curved walls introduce errors in the GO ray tracing procedure. The four most important sources of error in the GO ray tracing schemes are:

(1) ray caustics (focii),

(2) ray-tubes which come close to grazing a convex surface, and

(3) creeping waves which diffract from the convex surface,

(4) diffraction by discontinuities in the curvature of the walls.

The last three of these can in theory be handled by the uniform theory of

diffraction (UTD) [2], but it would not be very practical to do so in the GRE method because the ray-optical nature of the ray-tubes would be lost. The first of these, i.e. caustics, have as yet no simple means of correction on a ray-tube by ray-tube basis. Therefore, it appears that until the GRE method evolves to the point where these inherent errors are overcome, it is necessary to evaluate there effect on the accuracy of the method. Figure 80 may offer some insight into the first three sources of error above, and some S-shaped cavity results which will be discussed later may offer some insight into the fourth source of error because the S-shaped cavities have discontinuities in curvature.

For positive angles of incidence, the reflection of the incident plane wave GO field will form a caustic coming off of the outermost wall of the cavity as Figure 3 illustrates for a similar geometry. This caustic would extend to the termination of the geometry of Figure 80, where the fields are integrated according to the GRE/RI procedure. Therefore, if this caustic presents a significant error, it should appear in the backscatter results for positive angles of incidence. Figures 80(a) and (b) both show some error in the range $\theta_i > 0°$, but it is not very significant (the errors near axial incidence in these figures will be discussed later next). So it is possible that the effect of the caustic is reduced by integrating across it such that the singularity is balanced out. Numerically, it is highly unlikely that a ray-tube will have a singularity exactly in the cross-section of integration. In fact it can be shown that integrating across the type of ray-tube used in this method very near but not exactly on a caustic yields a finite value.

The second and third of the above errors would be evident in Figure 80 for angles of incidence near the axis because the incident plane wave field will come close to grazing the innermost wall of the cavity and a creeping wave which travels along this innermost wall will be most strongly excited for such cases as in error

186

(3). It follows that errors (2) and (3) will always go hand-in-hand. Both of the graphs in Figure 80 seem to show the most error in the range $-10° < \theta_i < 10°$, suggesting that these mechanisms are the main source of error. Since these errors are associated with surface diffraction effects, it is expected that the error will diminish with increasing frequency. Figure 81 shows the backscatter pattern for an open-ended annular waveguide cavity as in Figure 80, except that it is twice as large in terms of wavelength, and five sub-apertures are used as in Figure 80(b). The overall agreement is better than for the case of 5.10(b) but there is still some error near axial incidence, probably again due to grazing/creeping wave effects.

Figures 82 and 83 show the backscatter patterns of a small parallel-plate cavity and a small S-shaped cavity, respectively, comparing the GRE/AI and GO/AI methods with the modal reference solution. The GRE/AI result agrees very well for the parallel-plate case and reasonably well for the S-shaped case. It is much better than the GO/AI result for both cases because the diffracted field not present in the GO/AI method is more significant for these smaller geometries.

Figures 84 (a) and (b) show the backscatter patterns of a larger S-shaped cavity using the GRE/RI method with three and five sub-apertures, respectively. Note that these cavities are made up of alternating parallel-plate and annular waveguide sections. The five sub-aperture result agrees quite well with the reference solution and the three sub-aperture result agrees reasonably well. Of course the three sub-aperture result required fewer ray-tubes to be traced (600 as opposed to 1000 for the five sub-aperture case). The excellent agreement of Figure 84(b) with the reference solution suggests that the fourth source of error—diffraction from discontinuities in curvature—is not significant.

Figures 85 (a) and (b) are the same cases as in 84(a) and (b), respectively, except that waveguide cavity is three times as long. Here both the three and

five sub-aperture results agree only reasonably well, with the five sub-aperture result being slightly better. Once again, the three sub-aperture required fewer ray-tubes to be traced (2000 as opposed to 3500 for the five sub-aperture case). There is a simple explanation for the degradation of the accuracy of the GRE/RI method for this longer cavity. It is because the errors associated with the GO ray tracing technique used in the GRE method accumulate as the ray-tubes propagate farther inside the waveguide. Therefore, the GRE method is expected to decrease in accuracy as the length of the waveguide cavity increases, for a given waveguide cross-sectional area and frequency. Furthermore, it is not expected that the method will improve much in accuracy simply by using more sub-apertures or smaller ray-tubes. However, the accuracy is expected to increase with frequency for a given geometry because the errors associated with neglecting the curved surface diffraction effects decrease.

— modal reference solution, - - GRE/RI solution
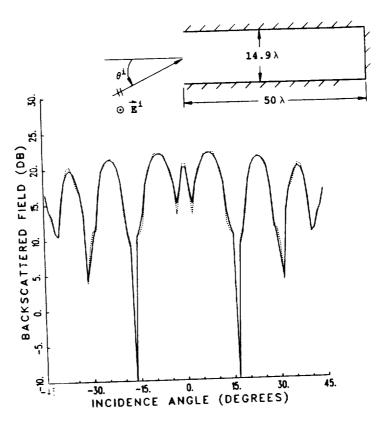
Figure 77: Backscatter pattern of an open-ended parallel-plate waveguide with a short circuit termination. $\perp$ polarization, 3 sub-apertures, 1200 total ray-tubes.

— modal reference solution, - - GRE/RI solution
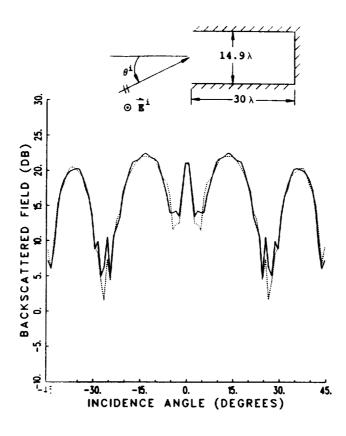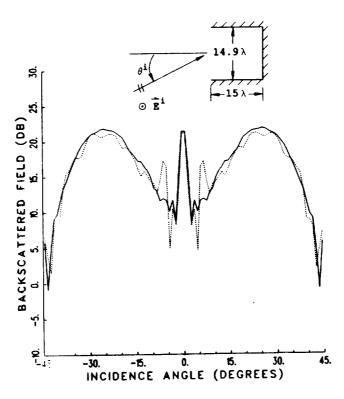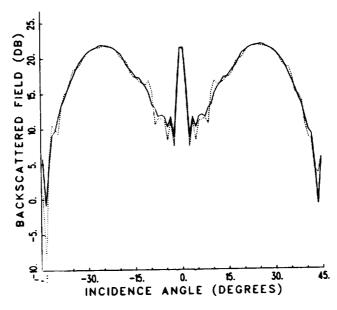
Figure 78: Backscatter pattern of an open-ended parallel-plate waveguide with a short circuit termination. ⊥ polarization, 3 sub-apertures, 600 total ray-tubes.

190
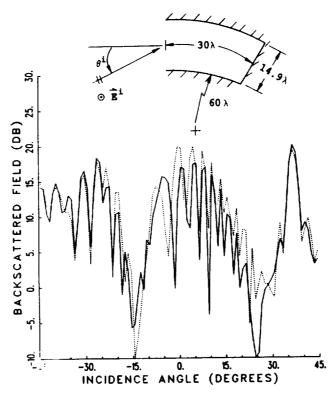
(a) 3 sub-apertures, 300 total ray-tubes
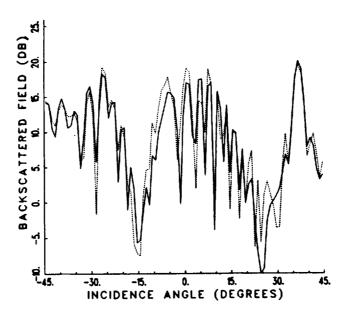
(b) 5 sub-apertures, 550 total ray-tubes

— modal reference solution, - - GRE/RI solution

Figure 79: Backscatter pattern of an open-ended parallel-plate waveguide with a short circuit termination, $\perp$ polarization.

191

(a) 3 sub-apertures, 700 total ray-tubes

(b) 5 sub-apertures, 1000 total ray-tubes

— modal reference solution, - - GRE/RI solution

Figure 80: Backscatter pattern of an open-ended annular waveguide with a short circuit termination, ⊥ polarization.

192

— modal reference solution, - - GRE/RI solution
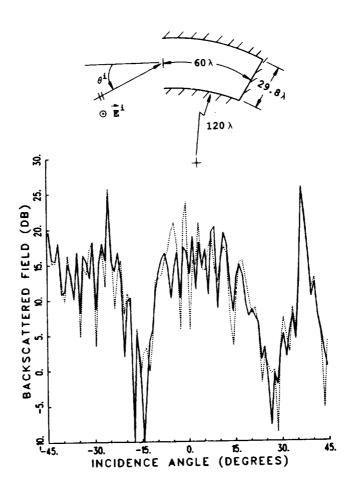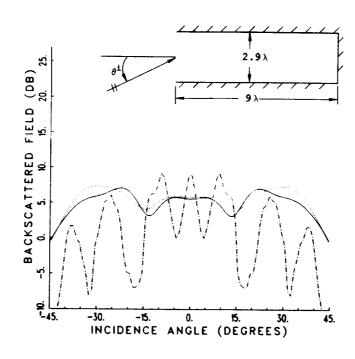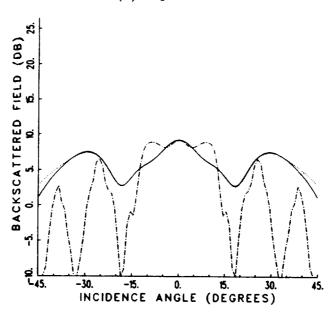
Figure 81: Backscatter pattern of an open-ended annular waveguide with a short circuit termination. $\perp$ polarization, 5 sub-apertures, 2000 total ray-tubes.

(a) ⊥ polarization

(b) ∥ polarization
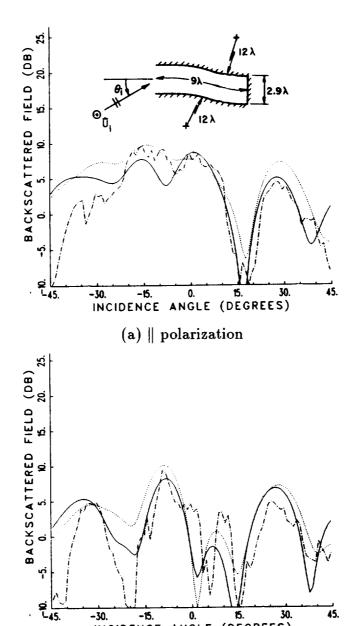
—— modal reference solution, - - - GRE/AI solution, – - – GO/AI solution

Figure 82: Backscatter pattern of a small open-ended parallel plate waveguide cavity with a planar short circuit termination, 3 sub-apertures, 150 total rays.

194

(a) ∥ polarization

(b) ⊥ polarization

—— modal reference solution, - - - GRE/AI solution, – – – GO/AI solution
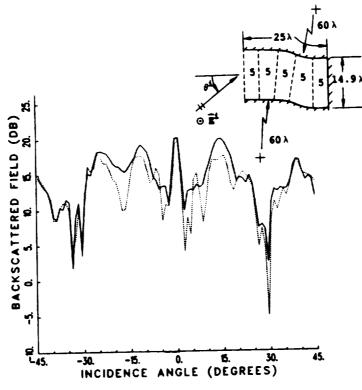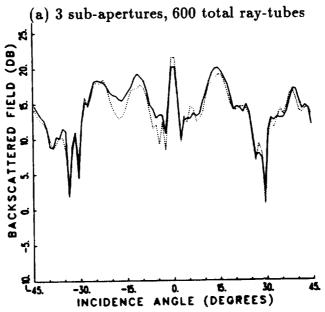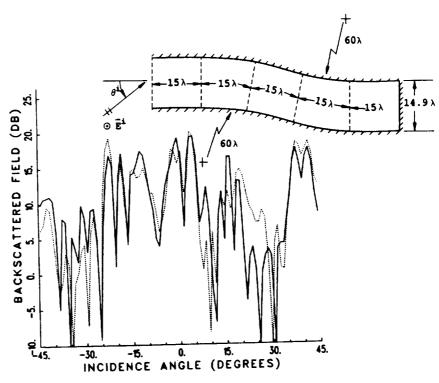
Figure 83: Backscatter pattern of a small open-ended annular waveguide cavity with a planar short circuit termination, 3 sub-apertures, 150 total rays.

(a) 3 sub-apertures, 600 total ray-tubes

(b) 5 sub-apertures, 1000 total ray-tubes

— modal reference solution, - - GRE/RI solution
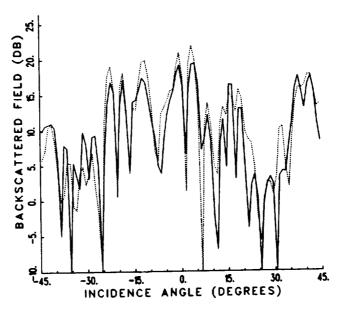
Figure 84: Backscatter patterns of a large open-ended S-shaped waveguide cavity with a planar short circuit termination, ⊥ polarization.

(a) 3 sub-apertures, 2000 total ray-tubes

(b) 5 sub-apertures, 3500 total ray-tubes

— modal reference solution, - - GRE/RI solution

Figure 85: Backscatter patterns of a large open-ended S-shaped waveguide cavity with a planar short circuit termination, ⊥ polarization.

197

CHAPTER VI

CONCLUSIONS AND DISCUSSION

In this report four different high frequency methods have been described for analyzing the EM scattering by relatively general open-ended waveguide cavities. They are the hybrid asymptotic modal method (Chapter II), the geometrical optics (GO) ray shooting method (Chapter III), the Gaussian beam (GB) shooting method (Chapter IV), and the generalized ray expansion (GRE) method (Chapter V). It was seen that each of these methods have some advantage over the other methods in terms of applicability and/or reliability, as well as some limitations. This report is concerned more with the development of the GB and GRE methods; the other two methods have been developed previously elsewhere but are included here for comparison.

The hybrid modal method of Chapter II is the most accurate of the four methods because it uses a high frequency asymptotic approximation to the exact eigenfunction solution, using the waveguide modes of the interior sections making up the cavity, and employs that along with the geometrical theory of diffraction (GTD) combined with the equivalent current method (ECM) to handle the reflection and transmission of modes across junctions. The multiple interactions between the junctions between waveguide sections, the open end and the termination are handled self-consistently using the multiple scattering matrix (MSM) concept. It was seen that many of the component reflection type matrices of the

MSM can be left out because they are negligible compared with the termination reflection matrix $[S_\Gamma]$, greatly simplifying the computation. Smooth junctions between waveguide sections, such as between a parallel-plate section and an annular section, are examples where the junction reflection matrix would be minimal.

The main limitation of the hybrid modal method is applicability—it is only practical to use when the open-ended cavity is made up of sections of uniform waveguides whose walls coincide with a separable coordinate system for which the eigenmodal fields can be found. Some common examples of this type of uniform waveguide are cylindrical (circular), rectangular, 2-D parallel-plate and annular, linearly tapered (wedge shaped) and conical (spherical). Also, even if waveguide modes can be defined, it is very difficult to include any effects of loss in 3-D geometries because of power coupling between the otherwise orthogonal modes. For some 2-D geometries, the modal perturbation technique of [7] can handle a small amount of wall loss.

The second limitation of the hybrid modal method is the large number of propagating modes which can exist in some electrically large, realistic cavity geometries, which make the method inefficient computationally. However, this limitation can sometimes be offset using the selective modal scheme of [13] which greatly reduces the number of modes needed in the calculation, provided it can be applied to the specific waveguide configuration under consideration.

To overcome some of the limitations of the hybrid modal method, the GO ray shooting method could be used for electrically large cavities where it is expected that internal diffraction effects will be minimal. The main advantage of this method is that it can handle arbitrary non-uniform geometries for which modes cannot be defined in the conventional sense; also this method can account for the presence of interior cavity wall loss. It is also conceptually simple and yields results which are

199

usually acceptable for practical purposes. However, the method typically requires a very large amount of ray tracing because a new dense grid of ray-tubes needs to be tracked for each incidence angle, thus making it computationally time consuming when scattering data is needed over a wide range of incidence angles. Furthermore, it is prone to the errors inherent in the GO field, such as ray caustics and non-inclusion of any interior diffraction effects. These interior diffraction effects could be due to the rim at the open end, discontinuities in curvature along the inner cavity walls, and convex interior surfaces which cause creeping waves and non-ray-optic transition regions to form for near grazing incidence. Consequently, the GO ray shooting method usually does not give the details of a scattering pattern well in terms of matching peaks and nulls, but it does give the general trends in the envelope of the pattern providing useful engineering figures. Recently it has been demonstrated that the GO ray shooting method, or equivalently the "shooting and bouncing rays" (SBR) method [17], yields good agreement with modal solutions for waveguide cavities which are larger than 10λ across [38].

The Gaussian beam (GB) shooting method was developed to overcome some of the problems associated with the GO ray shooting method while retaining its generality. The GB's by nature have no caustics associated with them. Also, each beam stands alone as a basis function which is Maxwellian, i.e., a solution to the wave equation (paraxially), which is valid everywhere from the near to far field, unlike individual ray-tubes which are discontinuous across their boundaries and are not valid near caustics. It is noted that the ray-tubes individually are non-Maxwellian but when combined with all the other ray-tubes they represent a total GO field which is asymptotically Maxwellian.

The sub-aperture expansion technique of arraying the GB's to represent the fields radiating from an aperture in free space and in the presence of cavity walls

followed from a modification of the Gabor expansion used in [26] and [27]. In this type of expansion, only the expansion coefficients depend on the direction of the incident field so the GB's need to be tracked only once for a wide range of incidence angles; this is in contrast to the GO ray shooting method which requires a new set of ray-tubes be tracked each time the incidence angle changes. Furthermore, fewer total GB's need to be tracked than ray-tubes, in general. These properties make the GB shooting method very computationally efficient.

The main difficulty with the GB shooting method is that the GB's that are launched by the aperture must be well focussed to maintain resolution after being tracked along their axes via successive reflections off the interior cavity walls. However the well focussed GB's which are narrow spectrally are typically quite wide spatially in order to be narrow spectrally (i.e., slowly divergent). This is due to their independent Maxwellian functional form. And when they reflect from curved walls in the axial beam tracking scheme they tend to diverge more, so they become wider the farther they propagate inside the cavity. Eventually they become too wide spatially to fit inside the cavity or too wide to adequately sample the wall geometry (i.e., the curvature of the wall may vary too much in the area illuminated by a beam to obtain an accurate reflected beam). As the GB's become wider, the axial method of tracking them breaks down and the problem of grazing convex surfaces becomes much more serious. Therefore, the GB shooting method is limited to waveguide cavities which are large in terms of wavelength and relatively shallow in terms of the length to width ratio L/d. Some general rules of thumb were presented in Section 4.5 for assessing the applicability of the method to a given cavity configuration. The accuracy of the method is quite adequate for most practical purposes with some small errors stemming from beam divergence effects due to reflection from curved walls.

201

The generalized ray expansion (GRE) was developed to overcome some of the difficulties associated with the GB shooting methods by replacing the Gaussian beam basis functions with GO ray-tubes. Thus, the GRE method uses the GO ray-tube tracking technique of the GO method along the the sub-aperture expansion technique of the GB method. Using this combination, the angular grid of ray-tubes needs to be tracked only once for a wide range of incidence angles as in the GB method and the open-ended waveguide cavity can be made arbitrarily long because the ray-tubes can be made arbitrarily narrow (because they are non-Maxwellian). In theory this is true, but in practice it is seen that the errors associated with the GO ray-tube tracking technique accumulate the farther a ray-tube propagates, so the accuracy degrades the longer the cavity. It is noted that in all of the latter GRE and GB shooting methods it is only necessary to trace the fields in the cavity to the termination and not back out again, by using the termination reciprocity integral if desired. This greatly reduces the amount of ray or beam tracking and should theoretically reduce the errors associated with long propagation paths. However, in practice it is seen that the reciprocity integral tends to be more sensitive to errors in the fields of the integrand than the aperture integral, so it is difficult to conclude that the one-way field tracking of the reciprocity integral methods is more accurate than the two-way field tracing of the aperture integral methods. In any case, the reciprocity integral method greatly reduces the amount of ray or beam tracking and so it is always more efficient.

The total number of ray-tubes which need to be tracked in the GRE method is generally much greater than the number of ray-tubes tracked in the GO ray shooting method for a single incidence angle. However, the GRE method provides scattering data over a continuous range of incidence angles, the size of which is determined by how wide the cone of ray-tubes is in the aperture expansion. To

202

obtain the same information using the GO method would generally require a much larger number of total ray-tubes to be tracked because a new set is tracked for each incidence angle. Therefore, in terms of ray-tube tracking efficiency, the GO or SBR method would be superior to the GRE method only when scattering data is required over a very narrow range of incidence angles. Furthermore, because the GRE method includes the effect of interior diffraction by the rim at the open end, it is generally more accurate than the GO method. This is especially true for smaller cavities (less than 10λ across) for which the interior contribution arising from the rim diffracted field is more significant.

To summarize, the hybrid modal method should be used for applications requiring highly accurate results where the open-ended waveguide cavity can be modeled by joining sections of uniform separable waveguides for which the modal fields are known, and for which the number of propagating modes is not too large to be prohibitive. It is often used as a reference solution to verify the accuracy of more general methods which are not as limited by the geometry. The GO ray shooting method is useful for general non-uniform waveguide cavity applications where the cavity is large in terms of wavelength and the accuracy of the result is not as critical. However, the GRE method is generally superior to the GO (or SBR) method in terms of accuracy and efficiency, with the possible exception being for cases where only a small number of incidence angles are required in which case the GRE loses its efficiency but not accuracy over the GO (SBR) approach. In any case the GRE method is expected to be more accurate than the GO method, especially for smaller cavities, but not as accurate as the hybrid modal method. The GB shooting method is applicable to non-uniform open-ended cavities with large cross-sections but which are not too long. In general the GB method is superior to the GO and GRE methods in terms of accuracy and efficiency, but only

for large, relatively shallow cavity configurations. For longer non-uniform cavities, the GRE or possibly the GO (SBR) method is recommended over the GB method.

Because the GB shooting method has demonstrated its usefulness for 2-D geometries, it should be extended to 3-D to evaluate its effectiveness on such configurations. In the extension to 3-D it is noted that the Gaussian beam basis functions would in general become astigmatic after interior cavity wall reflections, similar to the astigmatic GO ray-tube shown in Figure 34 with two different beam waists corresponding to the two caustics of the ray-tube. The tracking of such a 3-D GB would be done axially in a manner analogous to GO ray tracing, as was done for the 2-D case described in Section 4.4. Furthermore, ways to overcome the limited application to shallow cavities should be investigated. One likely possibility would be to generate a new GB expansion at a cross-section inside the waveguide cavity at some point before the original beam expansion begins to break down. This process could be repeated for cross-sections deeper and deeper within the cavity until the termination is reached. If this method is pursued, close attention should be paid to the possibility of beam turn-around. This means that for some geometries it is possible that a GB may reflect in such a way that it is turned around and propagates back to the open end before reaching the termination or some conveniently pre-defined cross-section near the termination.

More work needs to be done on the GRE method to verify its usefulness in realistic 3-D applications and to overcome some of the errors associated with the GO ray-tube tracking. As measured data on non-uniform open-ended cavities becomes available, the GRE method should be verified experimentally, especially for cases where wall loss is present. Also, methods need to be developed for evaluating the interior scattering by realistic cavity terminations via a modal reflection matrix $[S_\Gamma]$ or some other self-consistent characterization, so that they can be combined

with one of the methods described in this report for tracking the fields inside the waveguide cavity to the termination. It would be very valuable to be able to obtain such termination characterization through some sort of measurement technique so that the terminations could be arbitrarily complex.

To improve the GRE method, one area of investigation would be to consider different types of expansions of the fields radiating from an aperture, rather than through the use of sub-apertures. Using spherical vector wave functions (free space modes in spherical coordinates) to represent the fields radiating from an aperture which would subsequently be tracked in the presence of the waveguide cavity walls, is an example of a possible expansion technique. The fields inside the cavity would appear to be originating from a single point in the open end, rather than from several sub-apertures. However, the non-ray-optical nature of this type of expansion in the near zone of the open end may make field tracking in the presence of the cavity walls difficult.

Another area of investigation for improving the GRE method would be to consider different basis functions other than ray-tubes which could possibly overcome the problem of caustics, like the Gaussian beams did, while remaining narrow enough to adequately sample the cavity geometry. It would also be useful to have basis functions which did not suffer the $\left(\frac{1}{2}\lambda\right)^2$ restriction on cross-sectional area so that a smaller number of basis functions would have to be traced, similar to the GB method. It seems likely that a middle ground between the GB method and the GRE method can be reached which allows arbitrarily narrow ray or beam-like basis functions to adequately sample the cavity geometry without excessive divergence, but which do not have to be frequency dependent like the $\left(\frac{1}{2}\lambda\right)^2$ ray-tubes. These new basis functions may also be valid near caustics, thus eliminating some of the problems associated with finding the reflection of incident waves that have

caustics near the point of reflection. At any rate, it is along these lines that future research on ray and beam tracing methods should evolve.

APPENDIX A

MODAL FIELDS OF 2-D PARALLEL-PLATE AND ANNULAR WAVEGUIDES

This appendix derives the expressions for the orthonormal modal fields of the uniform 2-D parallel-plate and annular waveguides. The modal ray form of these modes is also derived.

"Orthonormal" means that each mode carries power independently of all the other modes and they are normalized to carry unit power. Mathematically, this is written

$$\int_S \left(\hat{e}_{mt} \times \hat{h}_{nt} \right) \cdot d\vec{S} \;=\; \delta_{mn} \tag{A.1}$$

where

$$\delta_{mn} \;=\; \begin{cases} 1 & \text{if } m = n \\ 0 & \text{if } m \neq n \end{cases} \tag{A.2}$$

$\hat{e}_{mt}$ = transverse component of the electric field of the mth waveguide mode,

$\hat{h}_{nt}$ = transverse component of the magnetic field of the nth waveguide mode,

$\vec{S}$ = any complete cross-section of the guide.

A.1 Orthonormal Modes of the Parallel-Plate Waveguide

Figure 86 shows a parallel-plate waveguide of infinite extent. The modes will
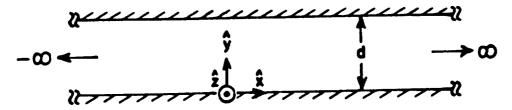
Figure 86: Parallel-plate waveguide geometry.

be split into TE_x (E transverse to x) and TM_x (H transverse to x) categories. For the TE_x case, the electric field is in the $\hat{z}$ direction and may be sometimes referred to as the perpendicular ($\perp$) or soft polarization. For the TM_x case, the magnetic field is in the $\hat{z}$ direction and may be sometimes referred to as the parallel ($\parallel$) or hard polarization. Starting with the TE_x case, the electric field is in the $\hat{z}$-direction and is a function of x and y:

$$\vec{E}(x,y) = \hat{z}E_z(x,y). \qquad (A.3)$$

The E-field is a solution to the wave equation

$$(\nabla^2 + k^2)\vec{E}(x,y) = 0 \qquad (A.4)$$

which in scalar form is

$$\left(\frac{\partial^2}{\partial x^2} + \frac{\partial^2}{\partial y^2} + k^2\right)E_z(x,y) = 0 \qquad (A.5)$$

where

$$k = \text{free space wave number} = 2\pi/\lambda$$

The boundary condition is that E_z equals zero on the walls of the guide. Using separation of variables and enforcing the boundary conditions the solution is found to be an infinite summation of modes

$$\vec{E}(x,y) = \sum_{n=1}^{\infty}\left[A_n^+\hat{e}_n(y)e^{-j\beta_n x} + A_n^-\hat{e}_n(y)e^{j\beta_n x}\right] \qquad (A.6)$$

208

where

$$\hat{e}_n(y) \;=\; \hat{z} P_n \sin\left(\frac{n\pi}{d}y\right) \tag{A.7}$$

$$\beta_n \;=\; \sqrt{k^2 - \left(\frac{n\pi}{d}\right)^2} \tag{A.8}$$

$P_n \;=\;$ normalization constant of the nth mode,

$A_n^{\pm} \;=\;$ modal field expansion coefficients for the nth $\pm\hat{x}$ propagating

(or evanescing) modes.

The infinite sum is usually truncated to include only propagating modes. For n greater than N, the modes are evanescent in nature and die out exponentially along the axis of the guide. This cutoff number is one less than the value of n which makes β_n pure imaginary, or

$$N \;=\; \mathrm{Int}\left(\frac{kd}{\pi}\right), \text{ the integer portion of } kd/\pi. \tag{A.9}$$

The H-field of the guide is derived directly from the E-field using one of Maxwell's equations

$$\nabla \times \vec{E}(x,y) \;=\; -j\omega\mu\vec{H}(x,y) \tag{A.10}$$

where

$$\omega\mu \;=\; \frac{k}{Y_o} \tag{A.11}$$

$Y_o \;=\;$ free space admittance ($\approx 1/377\ \Omega^{-1}$).

This gives

$$\vec{H}(x,y) \;=\; \frac{Y_o}{jk}\left(\hat{y}\frac{\partial}{\partial x} - \hat{x}\frac{\partial}{\partial y}\right) E_z(x,y)$$

$$=\; \sum_{n=1}^{\infty}\left[A_n^+ \hat{h}_n^+(y)e^{-j\beta_n x} + A_n^- \hat{h}_n^-(y)e^{j\beta_n x}\right] \tag{A.12}$$

where

$$\hat{h}_n^{\pm}(y) \;=\; \pm\hat{y}h_{ny}(y) + \hat{x}h_{nx}(y) \tag{A.13}$$

$$h_{ny}(y) \;=\; -P_n Y_o \frac{\beta_n}{k}\sin\left(\frac{n\pi}{d}y\right) \tag{A.14}$$

$$h_{nx}(y) \;=\; -P_n Y_o \frac{n\pi}{jkd}\cos\left(\frac{n\pi}{d}y\right). \tag{A.15}$$

P_n is found by normalizing to unity the power carried by the nth mode. This is done by integrating the Pointing vector over a cross-section of the guide and setting this equal to unity,

$$\int_0^d \hat{e}_n(y) \times \hat{h}_n^{\pm}(y) \cdot (\pm\hat{x})dy \;=\; 1. \tag{A.16}$$

Substituting and integrating yields

$$P_n \;=\; \sqrt{\frac{2kZ_o}{d\beta_n}} \tag{A.17}$$

where

$$Z_o \;=\; \text{free space impedance } (\approx 377\ \Omega),$$

$$=\; 1/Y_o. \tag{A.18}$$

The ray-optical form of these modes is found by writing the sine function of equation (A.7) in its Euler (exponential) form and combining the exponentials of (A.6):

$$\hat{e}_n(y)e^{\mp j\beta_n x} \;=\; \hat{z}\frac{P_n}{2j}\left[e^{j\left(\frac{n\pi}{d}y\mp\beta_n x\right)} - e^{j\left(-\frac{n\pi}{d}y\mp\beta_n x\right)}\right]. \tag{A.19}$$

By making the substitution

$$\sin\theta_n \;=\; \frac{n\pi}{kd}, \tag{A.20}$$

210
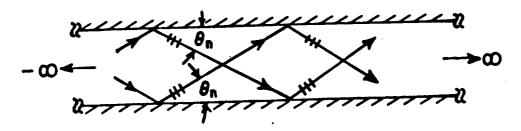
Figure 87: Modal rays of the parallel-plate waveguide.

and using

$$\begin{aligned}
\beta_n &= \sqrt{k^2 - \left(\frac{n\pi}{d}\right)^2} \\
&= k\sqrt{1 - \left(\frac{n\pi}{kd}\right)^2} \\
&= k\sqrt{1 - \sin^2\theta_n} \\
&= k\cos\theta_n \qquad\qquad (A.21)
\end{aligned}$$

equation (A.19) can be rewritten

$$\hat{e}_n(y)e^{\mp j\beta_n x} = \hat{z}\frac{P_n}{2j}\left[e^{jk(y\sin\theta_n \mp x\cos\theta_n)} - e^{jk(-y\sin\theta_n \mp x\cos\theta_n)}\right]. \quad (A.22)$$

This form represents two crossing plane waves which make an angle of θ_n with the guide walls as shown in Figure 87.

The TM_x case is handled analogously to the TE_x case, with the boundary condition now being $\partial H_z/\partial y$ equal zero on the walls:

$$\vec{H}(x,y) = \hat{z}H_z(x,y) \qquad\qquad (A.23)$$

$$(\nabla^2 + k^2)\vec{H}(x,y) = \left(\frac{\partial^2}{\partial x^2} + \frac{\partial^2}{\partial y^2} + k^2\right)H_z(x,y) = 0 \qquad (A.24)$$

$$\vec{H}(x,y) = \sum_{n=0}^{\infty}\left[A_n^+\hat{h}_n(y)e^{-j\beta_n x} + A_n^-\hat{h}_n(y)e^{j\beta_n x}\right] \qquad (A.25)$$

$$\hat{h}_n(y) = \hat{z}P_n\cos\left(\frac{n\pi}{d}y\right) \qquad\qquad (A.26)$$

$$\beta_n = \sqrt{k^2 - \left(\frac{n\pi}{d}\right)^2} \qquad\qquad (A.27)$$

211

$$\nabla \times \vec{H}(x, y) = j\omega\varepsilon\vec{E}(x, y) \tag{A.28}$$

$$\omega\varepsilon = \frac{k}{Z_o} \tag{A.29}$$

$$\vec{E} = -\frac{Z_o}{jk}\left(\hat{y}\frac{\partial}{\partial x} - \hat{x}\frac{\partial}{\partial y}\right)H_z(x, y)$$

$$= \sum_{n=0}^{\infty}\left[A_n^+\hat{e}_n^+(y)e^{-j\beta_n x} + A_n^-\hat{e}_n^-(y)e^{j\beta_n x}\right] \tag{A.30}$$

$$\hat{e}_n^{\pm}(y) = \pm\hat{y}e_{ny}(y) + \hat{x}e_{nx}(y) \tag{A.31}$$

$$e_{ny}(y) = P_nZ_o\frac{\beta_n}{k}\cos\left(\frac{n\pi}{d}y\right) \tag{A.32}$$

$$e_{nx}(y) = -P_nZ_o\frac{n\pi}{jkd}\sin\left(\frac{n\pi}{d}y\right) \tag{A.33}$$

$$P_n = \sqrt{\frac{2kY_o}{d\beta_n\varepsilon_n}} \tag{A.34}$$

$$\varepsilon_n = \begin{cases} 2 & \text{if } n = 0 \\ \\ 1 & \text{otherwise} \end{cases} \tag{A.35}$$

and the ray-optical form of the TM_x modes is given by

$$\hat{h}_n(y)e^{\mp j\beta_n x} = \hat{z}\frac{P_n}{2}\left[e^{jk(y\sin\theta_n\mp x\cos\theta_n)} + e^{jk(-y\sin\theta_n\mp x\cos\theta_n)}\right]. \tag{A.36}$$

Notice that for the TM_x case, the $n = 0$ term is included in the summation. This corresponds to a TEM mode. Ray-optically this mode is a plane wave traveling down the guide with θ_n equal zero.

A.2 Orthonormal Modes of the Annular Waveguide

Figure 88 shows an annular waveguide of infinite extent. This does not make sense physically because the guide would join ends to form a ring. However, it is allowable mathematically to assume that ϕ goes to infinity in both directions, instead of being periodic. It is necessary to make this assumption to get the correct waveguide modes to describe the fields in small sections of an annular guide, such as the ones used to make up the inlet. Starting with the TE_x case, the electric

212
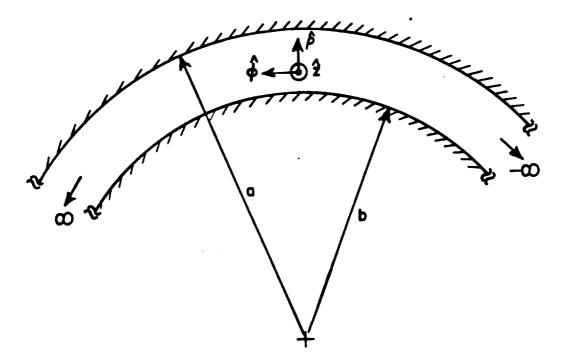
Figure 88: Annular waveguide geometry.

field is in the $\hat{z}$-direction and is a function of ρ and ϕ

$$\vec{E}(\rho,\phi) \;=\; \hat{z}E_z(\rho,\phi). \tag{A.37}$$

The E-Field is a solution to the wave equation

$$(\nabla^2 + k^2)\vec{E}(\rho,\phi) \;=\; 0 \tag{A.38}$$

which in scalar form is (using the cylindrical form of the Laplacian)

$$\left[\frac{1}{\rho}\frac{\partial}{\partial\rho}(\rho\frac{\partial}{\partial\rho}) + \frac{1}{\rho^2}\frac{\partial^2}{\partial\phi^2} + k^2\right] E_z(\rho,\phi) \;=\; 0. \tag{A.39}$$

The boundary condition is that E_z equals zero on the walls of the guide. Separating variables and substituting into equation (A.39), multiplying by ρ^2 and dividing out $E_z(\rho,\phi)$ yields

$$\frac{\rho}{R(\rho)}\frac{d}{d\rho}\left[\rho\frac{dR(\rho)}{d\rho}\right] + \frac{1}{\Phi(\phi)}\frac{d^2\Phi(\phi)}{d\phi^2} + (k\rho)^2 \;=\; 0 \tag{A.40}$$

213

where the separation equation is

$$E_z(\rho, \phi) = R(\rho)\Phi(\phi). \tag{A.41}$$

Introducing the separation constant ν gives two independent differential equations:

$$\frac{1}{\Phi(\phi)}\frac{d^2\Phi(\phi)}{d\phi^2} = -\nu^2 \tag{A.42}$$

$$\rho\frac{d}{d\rho}\left[\rho\frac{dR(\rho)}{d\rho}\right] + [(k\rho)^2 - \nu^2]R(\rho) = 0. \tag{A.43}$$

The solutions to equation (A.42) are

$$\Phi(\phi) = e^{j\nu\phi} \text{ and } e^{-j\nu\phi}. \tag{A.44}$$

(A.43) is Bessel's equation and has solutions

$$R(\rho) = H_\nu^{(1)}(k\rho) \text{ and } H_\nu^{(2)}(k\rho) \tag{A.45}$$

where

$$H_\nu^{(1)}(k\rho), H_\nu^{(2)}(k\rho) = \text{Hankel functions of the first and second kinds,}$$

$$\text{respectively, of order } \nu \text{ and argument } k\rho.$$

Using linear combinations of these solutions and enforcing the boundary conditions gives the complete solution for the electric field as

$$\vec{E}(\rho, \phi) = \sum_{n=1}^{\infty}\left[B_n^+\hat{e}_n(\rho)e^{-j\nu_n\phi} + B_n^-\hat{e}_n(\rho)e^{j\nu_n\phi}\right] \tag{A.46}$$

where

$$\hat{e}_n(\rho) = \hat{z}A_n R_n(k\rho) \tag{A.47}$$

$$R_n(k\rho) = \frac{1}{2j}\left[H_{\nu_n}^{(2)}(kb)H_{\nu_n}^{(1)}(k\rho) - H_{\nu_n}^{(1)}(kb)H_{\nu_n}^{(2)}(k\rho)\right] \tag{A.48}$$

214

in which $R_n(kb) = 0$ has been employed, and

$$A_n \quad = \quad \text{normalization constant of the } n^{th} \text{ mode,}$$

$$B_n^{\pm} \quad = \quad \text{modal field expansion coefficients for the } n^{th} \pm \hat{\phi} \text{ propagating}$$

$$\text{(or evanescing) mode.}$$

If ϕ had a periodic boundary condition corresponding to a $360°$ degree annular ring, the eigenvalues ν_n would be completely determined. However, for the annular guide of infinite extent, the eigenvalues must be found using the remaining ρ dependent boundary condition. Thus, they are found from the transcendental equation

$$R_n(ka) \quad = \quad 0 \tag{A.49}$$

which usually must be solved numerically.

As in a parallel-plate guide, the summation generally only includes values of n for which ν_n is real. This is because for some values of n, ν_n will be purely imaginary and the mode will die out exponentially along the axis of the guide.

The H-field of the guide is derived directly from the E-field using one of Maxwell's equations

$$\nabla \times \vec{E}(\rho,\phi) \quad = \quad -j\omega\mu\vec{H}(\rho,\phi) \tag{A.50}$$

$$\omega\mu \quad = \quad \frac{k}{Y_o} \tag{A.51}$$

which gives

$$\vec{H}(\rho,\phi) \quad = \quad -\frac{Y_o}{jk}\left(\hat{\rho}\frac{1}{\rho}\frac{\partial}{\partial\phi} - \hat{\phi}\frac{\partial}{\partial\rho}\right)E_z(\rho,\phi)$$

$$= \quad \sum_{n=1}^{\infty}\left[B_n^{+}\hat{h}_n^{+}(\rho)e^{-j\nu_n\phi} + B_n^{-}\hat{h}_n^{-}(\rho)e^{j\nu_n\phi}\right] \tag{A.52}$$

where

$$\hat{h}_n^{\pm}(\rho) \quad = \quad \pm\hat{\rho}h_{n\rho}(\rho) + \hat{\phi}h_{n\phi}(\rho) \tag{A.53}$$

215

$$h_{n\rho}(\rho) = A_n Y_o \frac{\nu_n}{k\rho} R_n(k\rho) \qquad (A.54)$$

$$h_{n\phi}(\rho) = -jA_n Y_o R'_n(k\rho). \qquad (A.55)$$

A_n is found by normalizing to unity the power carried by the nth mode. This done by integrating the Poynting vector over a cross-section of the guide and setting this equal to unity,

$$\int_b^a \hat{e}_n(\rho) \times \hat{h}_n^\pm(\rho) \cdot (\pm\hat{\phi})d\rho = 1. \qquad (A.56)$$

Substituting and changing the variable of integration to $u = k\rho$ gives the normalization coefficient

$$A_n = \left[\frac{\nu_n}{kZ_o} \int_{kb}^{ka} R_n^2(u) \frac{du}{u} \right]^{-\frac{1}{2}}. \qquad (A.57)$$

The integral of equation (A.57) can be written in closed form using a property of Hankel functions. However, the resulting equation is quite long and cumbersome and contains derivatives with respect to the order ν_n of the Hankel functions. It was found that it is easier to just do the integration numerically.

The ray-optical form of the waveguide modes in the annular guide is obtained using the large argument approximation to the Hankel functions (also known as the Debye Tangent approximation). For the Hankel function of the second kind, it is given by

$$H_\nu^{(2)}(x) \approx \sqrt{\frac{j2}{\pi x \sin\gamma}} e^{-j(x\sin\gamma - \nu\gamma)}, \text{ for } x \gg 1, \ x \neq \nu \qquad (A.58)$$

where

$$\cos\gamma = \frac{\nu}{x}. \qquad (A.59)$$

Using this approximation, the $H_{\nu_n}^{(2)}$ term of a mode with the ϕ variation included can be written as

$$H_{\nu_n}^{(2)}(k\rho)e^{-j\nu_n\phi} \approx \sqrt{\frac{j2}{\pi k\rho \sin\gamma}} e^{-j[k\rho\sin\gamma + \nu_n(\phi - \gamma)]} \qquad (A.60)$$

216
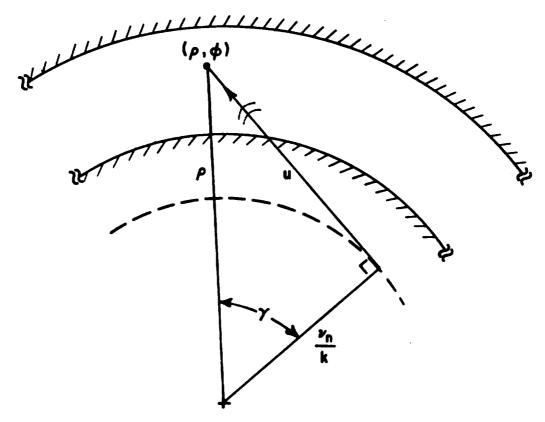
Figure 89: Geometrical significance of the asymptotic form of the modes in an annular waveguide.

$$\cos\gamma = \frac{\nu_n}{k\rho}.\tag{A.61}$$

Changing variables gives the ray-optical form

$$H_{\nu_n}^{(2)}(k\rho)e^{-j\nu_n\phi} \approx \sqrt{\frac{j2}{\pi ku}}e^{-j(ku+\nu_n\phi_o)}\tag{A.62}$$

where

$$u = \rho\sin\gamma\tag{A.63}$$

$$\phi = \gamma + \phi_o\tag{A.64}$$

and ϕ_o is a constant. This is the form of an outward traveling cylindrical wave. Figure 89 shows the geometrical significance of this derivation. Notice that u is the

217

distance from a concentric caustic of radius ν_n/k and γ is the angular displacement from this caustic. The $H_{\nu_n}^{(1)}$ term is handled the same way,

$$H_\nu^{(1)}(x) \approx \sqrt{\frac{-j2}{\pi x \sin \gamma}} e^{j(x \sin \gamma - \nu \gamma)} \tag{A.65}$$

$$H_{\nu_n}^{(1)}(k\rho)e^{-j\nu_n\phi} \approx \sqrt{\frac{-j2}{\pi k u}} e^{j(ku+\nu_n\phi_o)} \tag{A.66}$$

which is the form of the corresponding inward traveling (converging) cylindrical wave.

Figure 90 illustrates the modal ray form of the modes of the annular waveguide. It consists of crossing cylindrical waves which share a concentric caustic of radius ν_n/k. The angles the rays make with the walls of the guide are obtained easily from the ray-optic geometry,

$$\theta_{an} = \cos^{-1}\left(\frac{\nu_n}{ka}\right) \tag{A.67}$$

$$\theta_{bn} = \cos^{-1}\left(\frac{\nu_n}{kb}\right). \tag{A.68}$$

It happens that the modal ray caustic can lie inside the guide, as shown in figure 91. This special case is referred to as a "Whispering Gallery" (WG) mode. The significance of this type of mode is that almost all of the power in the mode is confined between the modal caustic and the outer wall of the guide. The propagating portion of the fields never "see" the inner wall (although the modal caustic radius ν_n/k depends on it) because the fields are evanescent between the caustic and the inner wall, as shown in figure 92.

The TM_x case is handled similarly, with the boundary condition being $\partial H_z/\partial y$ equal zero on the walls,

$$\vec{H}(\rho,\phi) = \hat{z} H_z(\rho,\phi) \tag{A.69}$$

$$(\nabla^2 + k^2)\vec{H}(\rho,\phi) = \left[\frac{1}{\rho}\frac{\partial}{\partial\rho}(\rho\frac{\partial}{\partial\rho}) + \frac{1}{\rho^2}\frac{\partial^2}{\partial\phi^2} + k^2\right] H_z(\rho,\phi)$$

218
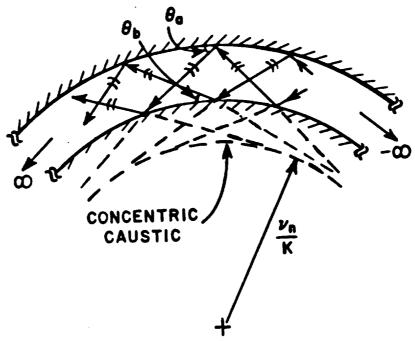
Figure 90: Modal rays of the annular waveguide.
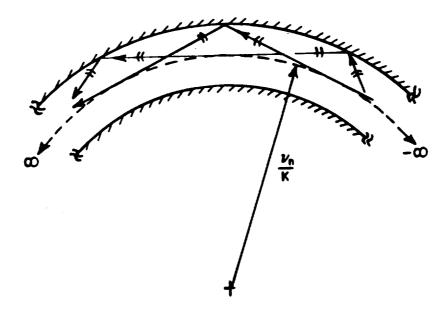
Figure 91: Whispering gallery modal rays of the annular waveguide.

219
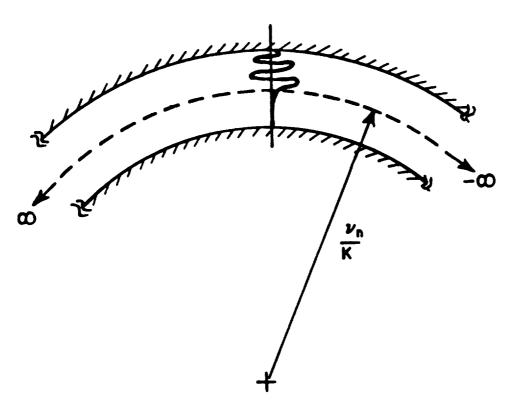
Figure 92: Field of a whispering gallery mode.

$$= 0 \tag{A.70}$$

$$\vec{H}(\rho, \phi) = \sum_{n=1}^{\infty} \left[B_n^+ \hat{h}_n(\rho) e^{-j\nu_n \phi} + B_n^- \hat{h}_n(\rho) e^{j\nu_n \phi} \right] \tag{A.71}$$

$$\hat{h}_n(\rho) = \hat{z} A_n R_n(k\rho) \tag{A.72}$$

$$R_n(k\rho) = \frac{1}{2j} \left[H_{\nu_n}^{(2)\prime}(kb) H_{\nu_n}^{(1)}(k\rho) - H_{\nu_n}^{(1)\prime}(kb) H_{\nu_n}^{(2)}(k\rho) \right] \tag{A.73}$$

$$R_n'(ka) = 0 \tag{A.74}$$

$$\nabla \times \vec{H}(\rho, \phi) = j\omega \varepsilon \vec{E}(\rho, \phi) \tag{A.75}$$

$$\omega \varepsilon = \frac{k}{Z_o} \tag{A.76}$$

$$\vec{E}(\rho, \phi) = -\frac{Z_o}{jk} \left(-\hat{\rho} \frac{1}{\rho} \frac{\partial}{\partial \phi} - \hat{\phi} \frac{\partial}{\partial \rho} \right) H_z(\rho, \phi)$$

$$= \sum_{n=1}^{\infty} \left[B_n^+ \hat{e}_n^+(\rho) e^{-j\nu_n \phi} + B_n^- \hat{e}_n^-(\rho) e^{j\nu_n \phi} \right] \tag{A.77}$$

$$\hat{e}_n^{\pm}(\rho) = \pm \hat{\rho} e_{n\rho}(\rho) + \hat{\phi} e_{n\phi}(\rho) \tag{A.78}$$

$$e_{n\rho}(\rho) = -A_n Z_o \frac{\nu_n}{k\rho} R_n(k\rho) \tag{A.79}$$

$$e_{n\phi}(\rho) = -j A_n Z_o R_n'(k\rho) \tag{A.80}$$

$$A_n = \left[\frac{\nu_n}{kY_o} \int_{kb}^{ka} R_n^2(u) \frac{du}{u} \right]^{-\frac{1}{2}} . \tag{A.81}$$

Notice that the eigenvalues ν_n for this case are found from the transcendental equation (A.74). The ray optical form for the TM_x case is the same as the TE_x case with the appropriate change of constants.

APPENDIX B

APERTURE INTEGRATION OF GO RAY-TUBES

A simple method of obtaining the scattering by open-ended waveguide cavities using ray-tube tracking methods, such as the geometrical optics with aperture integration (GO/AI) and the generalized ray expansion with aperture integration (GRE/AI) methods, is to perform a physical optics (PO) aperture integration on the ray-tubes which exit the cavity. The scattering by external features of the waveguide cavity must be added separately. The scattering by the rim at the open end of the cavity is an important component of external scattering and is usually included in open-ended waveguide cavity scattering calculations. High frequency asymptotic methods such as the geometrical theory of diffraction (GTD) and the equivalent current method (ECM) are often used for such calculations. Details of this can be found in [5,6,1,3,10] and in Chapter II of this report, so this scattering mechanism will not be discussed further here.

Figure 93 shows the geometry of the aperture (open end) of a waveguide cavity with a single ray-tube exiting through the aperture. For this n^{th} ray-tube:

$\hat{k}_n$ = unit vector pointing in the direction of propagation of the central ray of the nth ray-tube,

$\vec{r}_n'$ = vector from the origin to the point where the central ray intersects the aperture.
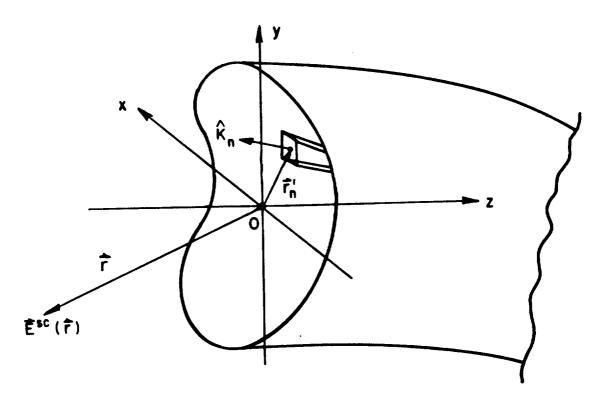
Figure 93: Open end of a waveguide cavity with a single ray-tube exiting.

The cavity scattered field can be written as the sum of the fields radiated by all of the N ray-tubes leaving the cavity through the open end as

$$\vec{E}^{sc}(\vec{r}) = \sum_{n=1}^{N} \vec{E}_n^{sc}(\vec{r}) \tag{B.1}$$

where

$$\vec{E}_n^{sc}(\vec{r}) = \text{field radiated by the equivalent sources in the aperture of the}$$

$$n^{th} \text{ ray-tube.}$$

To find the fields radiated by the nth ray-tube, the far zone PO based radiation integral is used. However, instead of integrating the fields in the ray-tube over its projection in the aperture, as might be expected for an aperture integration problem, it is easier to integrate over the cross-section of the ray-tube where it intersects the aperture [18] because the fields in a ray-tube are assumed constant

223
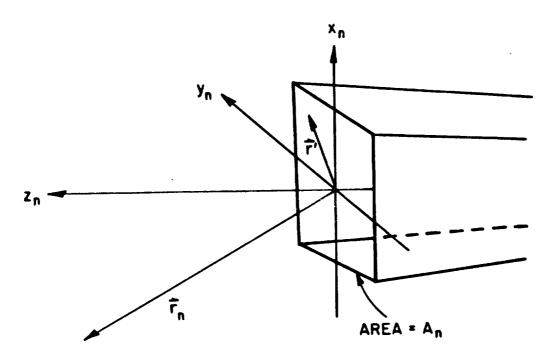
Figure 94: Geometry and relative coordinate system of the cross-section of the nth ray-tube at the point where it intersects the aperture.

in a given cross-section. Figure 94 shows the geometry of the cross-section of the nth ray-tube and its relative coordinate system, (x_n, y_n, z_n), which is centered at the point where the ray-tube intersects the aperture. The z_n-axis is along the direction of $\hat{k}_n$ of Figure 93.

The far zone fields radiated by the equivalent sources of the nth ray-tube in the open end is given by the following PO based radiation integral:

$$\vec{E}_n^{sc}(\vec{r}) = -\frac{jk}{4\pi}\frac{e^{-jkr_n}}{r_n}\left[\int\int_{A_n}\vec{M}_{sn}\times\hat{r}_n e^{jk\vec{r}\,'\cdot\hat{r}_n}dS'\right.$$
$$\left.-Z_o\hat{r}_n\times\int\int_{A_n}\hat{r}_n\times\vec{J}_{sn}e^{jk\vec{r}\,'\cdot\hat{r}_n}dS'\right] \tag{B.2}$$

where

$$\vec{J}_{sn} = \hat{k}_n\times\vec{H}_{no} \tag{B.3}$$

$$\vec{M}_{sn} = \vec{E}_{no}\times\hat{k}_n \tag{B.4}$$

$\vec{E}_{no}, \vec{H}_{no}$ = electric and magnetic fields in the cross-section of the ray-tube

224

in the open end,

$\vec{r}_n$ = vector from the point where the central ray of the ray-tube intersects the open end to the observer,

$\vec{r}\,'$ = vector to a source point in the ray-tube cross-section from the point where the central ray intersects the open end,

A_n = cross-sectional area of the ray-tube in the open end,

Z_o = free space impedance ($\approx 377\Omega$)

and the integration is over $\vec{r}\,'$ in the x_n-y_n plane.

Because of the ray-optical nature of the fields of the ray-tube, $\vec{E}_{no}$ and $\vec{H}_{no}$ in (B.3) and (B.4) can be written as

$$\vec{E}_{no} = \hat{p}_{en}E_{no} \tag{B.5}$$

$$\vec{H}_{no} = \hat{p}_{hn}H_{no} = \hat{p}_{hn}\frac{E_{no}}{Z_o} \tag{B.6}$$

where

$\hat{p}_{en}$ = electric polarization unit vector of the ray-tube in the open end,

$\hat{p}_{hn}$ = magnetic polarization unit vector,

$$= \hat{k}_n \times \hat{p}_{en}. \tag{B.7}$$

Using (B.3)-(B.7) and the following relations:

$$\hat{r}_n = \hat{r} \tag{B.8}$$

$$r_n = r - \vec{r}_n'\cdot\hat{r} \tag{B.9}$$

$$\hat{k}_n \times \hat{p}_{hn} = -\hat{p}_{en}, \tag{B.10}$$

(B.2) now reduces to

$$\vec{E}_n^{sc}(\vec{r}) = -[\hat{r}\times\hat{p}_{hn} + \hat{r}\times(\hat{r}\times\hat{p}_{en})]\frac{jk}{4\pi}\frac{e^{-jkr}}{r}E_{no}A_ne^{jk\vec{r}_n'\cdot\hat{r}}S_n(\hat{r})$$

225

where $S_n(\hat{r})$ is the shape function given by

$$S_n(\hat{r}) = \frac{1}{A_n} \int \int_{A_n} e^{jk\vec{r}\,'\cdot\hat{r}} dS'.$$
(B.12)

The form of (B.11) is that of a spherical wave originating at the point where the central ray of the nth ray-tube intersects the aperture with a pattern determined by the shape function of (B.12). This is similar to the result found in [17] and [18].

The integral in (B.12) is actually a two-dimensional Fourier transform of the polygonal shape of the ray-tube cross-section and can therefore be evaluated rather efficiently if the shape is known [17]. However, as suggested in Chapter III of this report, the recommended way of tracking a ray-tube is to ray-trace the central ray using the laws of GO and to choose an initial cross-sectional area so that the area of the ray-tube is less than $\left(\frac{1}{2}\lambda\right)^2$ when it exits through the open end. If this is done then the exact shape of the ray-tube when it exits is not known. But if the ray-tube is small enough it is expected that only the cross-sectional area affects the shape function and not the shape. If this assumption is true, the shape function of (B.12) is expected to give a pattern that is rotationally symmetric about the z_n axis for a given cross-sectional area and arbitrary shape. This will be investigated by considering the shape function for a small rectangle.

Assume the shape of the ray-tube is a rectangle which is of length a in the x_n direction and of width b in the y_n direction. The shape function of (B.12) for this case is

$$
\begin{aligned}
S_n(\hat{r}) &= \frac{1}{ab} \int_{-\frac{1}{2}b}^{\frac{1}{2}b} \int_{-\frac{1}{2}a}^{\frac{1}{2}a} e^{jk\vec{r}\,'\cdot\hat{r}} dx'_n dy'_n \\
&= \frac{1}{ab} \int_{-\frac{1}{2}b}^{\frac{1}{2}b} \int_{-\frac{1}{2}a}^{\frac{1}{2}a} e^{jk(x'_n \cos\phi_n \sin\theta_n + y'_n \sin\phi_n \sin\theta_n)} dx'_n dy'_n \\
&= \operatorname{sinc}\left(\frac{1}{2}ka\cos\phi_n\sin\theta_n\right) \operatorname{sinc}\left(\frac{1}{2}kb\sin\phi_n\sin\theta_n\right)
\end{aligned}
$$
(B.13)

where

$$\text{sinc}(x) = \frac{\sin x}{x} \tag{B.14}$$

θ_n, ϕ_n = angular spherical coordinates of the observer in the relative

coordinate system of the nth ray-tube where it intersects

the open end.

So far, this result shows that the integral is shape dependent, i.e., it is not rotationally symmetric about the z_n-axis because it has a ϕ_n dependence. Now impose the requirement

$$a, b < \frac{1}{2}\lambda. \tag{B.15}$$

The sinc functions are now well approximated by the quadratic portions of their Taylor series expansions and (B.13) becomes

$$
\begin{aligned}
S_n(\hat{r}) &\approx \left[1 - \frac{1}{6}\left(\frac{1}{2}ka\cos\phi_n\sin\theta_n\right)^2\right]\left[1 - \frac{1}{6}\left(\frac{1}{2}kb\sin\phi_n\sin\theta_n\right)^2\right] \\
&= 1 - \frac{1}{24}(ka\sin\theta_n)^2\cos^2\phi_n - \frac{1}{24}(kb\sin\theta_n)^2\sin^2\phi_n \\
&\quad + \frac{1}{576}(ka\sin\theta_n)^2(kb\sin\theta_n)^2\cos^2\phi_n\sin^2\phi_n.
\end{aligned} \tag{B.16}
$$

Using (B.15), the second and third terms of (B.16) are at most $.411\sin^2\theta_n$ and the last term is at most $.042\sin^4\theta_n$. Therefore, the last term can be dropped but the second and third terms should be kept, leaving

$$S_n(\hat{r}) \approx 1 - \frac{1}{24}(ka\sin\theta_n)^2\left(\cos^2\phi_n + \frac{b^2}{a^2}\sin^2\phi_n\right). \tag{B.17}$$

This result is still shape dependent because it depends on ϕ_n. However, if the rectangle becomes approximately square, i.e.,

$$b \approx a \tag{B.18}$$

227

then the ϕ_n dependence disappears and (B.17) becomes

$$
\begin{aligned}
S_n(\hat{r}) &\approx 1 - \frac{1}{24}(ka\sin\theta_n)^2 \\
&= 1 - \frac{1}{6}(\frac{1}{2}k\sqrt{A_n}\sin\theta_n)^2 \\
&\approx \operatorname{sinc}\left(\frac{1}{2}k\sqrt{A_n}\sin\theta_n\right)
\end{aligned}
\tag{B.19}
$$

where

$$
A_n = a^2
\tag{B.20}
$$

$$
= \text{cross-sectional area of the ray-tube.}
$$

This result can be compared with the result given in [18] for a circular cross-section of equal area. The shape function for this case is given by

$$
S_n(\hat{r}) = \frac{2J_1(u)}{u}
\tag{B.21}
$$

where

$$
u = k\sqrt{\frac{A_n}{\pi}}\sin\theta_n
\tag{B.22}
$$

$$
J_1(u) = \text{first order Bessel function of the first kind.}
$$

The quadratic portion of the Taylor series expansion of (B.21) for small u is given by

$$
\frac{2J_1(u)}{u} \approx 1 - \frac{1}{8}u^2
\tag{B.23}
$$

so

$$
S_n(\hat{r}) \approx 1 - \frac{1}{8\pi}\left(k\sqrt{A_n}\sin\theta_n\right)^2
\tag{B.24}
$$

which is nearly identical to (B.19) for the square cross-section. This result lends support to the assumption that if the cross-section is small enough, the pattern of

228

the shape function depends on the area and not the shape. (B.17) shows that if (B.18) is not satisfied, i.e., if the shape is not roughly symmetric about the z_n axis, the pattern does depend on the shape somewhat. However, the approximation of (B.19) has been shown to give numerically convergent results provided that

$$A_n \ < \ \left(\frac{1}{2}\lambda\right)^2, \tag{B.25}$$

as mentioned earlier. The convergence was tested by making the ray-tubes smaller and smaller in cross-sectional area. Furthermore, it can be shown using (B.16), (B.19), or (B.24) that $S_n(\hat{r}) \approx 1$ if $A_n < \left(\frac{1}{4}\lambda\right)^2$. In other words, the shape function disappears completely from (B.11) for a ray-tube with a cross-section of less than $\left(\frac{1}{4}\lambda\right)^2$.

The shape function can now be well approximated under the constraint of (B.25) by

$$S_n(\hat{r}) \ \approx \ \mathrm{sinc}\left(\frac{1}{2}k\sqrt{A_n}\left|\hat{r} \times \hat{k}_n\right|\right) \tag{B.26}$$

where the relation

$$\sin\theta_n \ = \ \left|\hat{r} \times \hat{k}_n\right| \tag{B.27}$$

has been used. The output area of a ray-tube is found by conserving power and is given by

$$A_n \ = \ \frac{\left|\vec{E}^i\right|^2}{\left|\vec{E}^{ll}_{no}\right|^2}A_{in} \tag{B.28}$$

where

$\vec{E}^{ll}_{no}$ = electric field of the nth ray-tube, without wall loss, as it exits through the open end,

$\vec{E}^i$ = electric field of the incident plane wave,

A_{in} = input cross-sectional area of the ray-tube,

229

for when the GO/AI method is used, and

$$A_n = \frac{\Omega_n}{\left|\vec{E}_{no}^{ll}\right|^2} \tag{B.29}$$

where

Ω_n = beam solid angle of the nth ray-tube when it is launched,

for when the GRE/AI method is used.

APPENDIX C

TERMINATION RECIPROCITY INTEGRAL DERIVATION

In this appendix, the method of using a termination reciprocity integral to find the cavity scattered fields is briefly described. The main advantage of this method is that the fields only need to be tracked from the open end of the waveguide cavity to the termination. It is not necessary to track them back from the termination to the open end. The other advantage is that this method allows the termination to be arbitrarily complex, as long as the reflection properties of the termination are known (e.g., through a modal reflection matrix or a plane wave spectral expansion).

C.1 General Bistatic Scattering Derivation for Three Dimensional Cavities

Figure 95 shows an arbitrary open-ended waveguide cavity illuminated by an infinitesimal electric current element $\vec{p}\,'$ at point P'. The cavity is semi-infinite to the right with an interior obstacle or termination existing somewhere inside the cavity to the right of the arbitrarily chosen cross-section S_t, as shown in the figure. Let the fields due to $\vec{p}\,'$ be denoted by $\vec{E}'$ and $\vec{H}'$. Let V_Σ be the volume defined by the external region of Figure 95 plus the interior of the cavity up to the plane S_t in front of the termination. Σ is the surface enclosing this volume and is decomposed as

$$\Sigma = \Sigma_\infty + S_w + S_t \qquad (C.1)$$

231
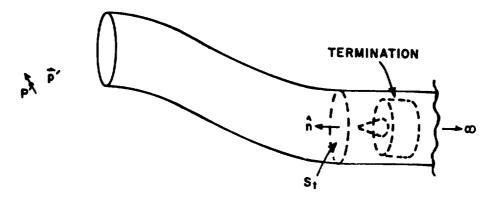
Figure 95: Open-ended waveguide cavity with an interior obstacle (termination) illuminated by an infinitesimal electric current element.

where

Σ_∞ = the free space surface at infinity in the exterior region,

S_w = the semi-infinite exterior surface of the waveguide cavity and the interior surface of the waveguide cavity up to S_t,

S_t = the cross-section of the waveguide in front of the termination,

as shown in Figure 96. The fields $\vec{E}'$ and $\vec{H}'$ satisfy Maxwell's curl equations in V_Σ:

$$\nabla \times \vec{H}' = jkY_o\vec{E}' + \vec{p}\,'\delta(P')$$ (C.2)

$$-\nabla \times \vec{E}' = jkZ_o\vec{H}'$$ (C.3)

where

k = free space wavenumber $(2\pi/\lambda)$,

Z_o = $1/Y_o$ = free space impedance ($\approx 377\Omega$),

$\delta(P')$ = delta function which is non-zero only at P'.

232
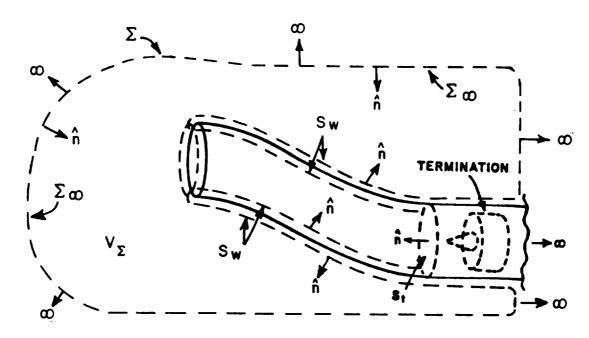
Figure 96: The surface Σ enclosing the volume V_Σ, composed of Σ_∞, S_w and S_t.

The fields $\vec{E}'$ and $\vec{H}'$ can be decomposed into incident and scattered components as

$$\vec{E}', \vec{H}' = \vec{E}'_i, \vec{H}'_i + \vec{E}'_s, \vec{H}'_s \tag{C.4}$$

where

$\vec{E}'_i, \vec{H}'_i$ = fields due to the current element $\vec{p}\,'$ in the absence of the
termination,

$\vec{E}'_s, \vec{H}'_s$ = fields due to the current element $\vec{p}\,'$ scattered by the
termination.

So, the incident fields are defined by the same geometry as in Figure 95, but with the termination beyond S_t removed, and it is assumed that these incident fields

233
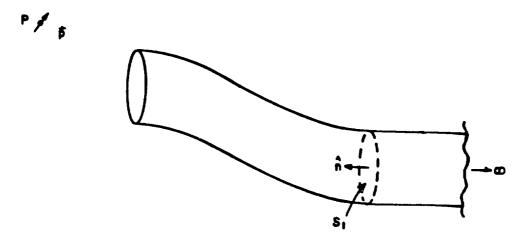
Figure 97: Cavity geometry of Figure 95 without the termination and illuminated by an electric current element at P.

are known. It is desired to find the scattered fields of (C.4) at some point P in the external region due to the presence of the termination.

Now consider the related configuration of Figure 97 which shows the same cavity geometry as in Figure 95 in the absence of the termination, illuminated by an infinitesimal electric current element $\vec{p}$ located at point P. Let the fields in the same volume V_Σ for this case be denoted by $\vec{E}_i$ and $\vec{H}_i$, with the subscript i denoting an incident field because the termination is not present. These fields satisfy Maxwell's curl equations in V_Σ similar to (C.2) and (C.3) above:

$$\nabla \times \vec{H}_i = jkY_o\vec{E}_i + \vec{p}\delta(P) \tag{C.5}$$

$$-\nabla \times \vec{E}_i = jkZ_o\vec{H}_i \tag{C.6}$$

where

$\vec{E}_i, \vec{H}_i$ = fields due to the electric current element $\vec{p}$ in the absence of

the termination.

Following the procedure in [32, pages 116–117], the differential form of the reciprocity relationship between the fields of (C.2), (C.3), (C.5) and (C.6) is given

234

by

$$-\nabla \cdot \left(\vec{E}' \times \vec{H}_i - \vec{E}_i \times \vec{H}' \right) \;=\; \vec{E}' \cdot \vec{p}\delta(P) - \vec{E}_i \cdot \vec{p}\,'\delta(P') \qquad \text{(C.7)}$$

which is valid in V_{Σ}. The procedure involves straightforward algebraic manipulation and a single differential vector identity.

Integrating (C.7) over the volume V_{Σ} and using the divergence theorem yields

$$\oint_{\Sigma} \left(\vec{E}' \times \vec{H}_i - \vec{E}_i \times \vec{H}' \right) \cdot \hat{n} dS \;=\; \vec{E}'(P) \cdot \vec{p} - \vec{E}_i(P') \cdot \vec{p}\,' \qquad \text{(C.8)}$$

where

$$\hat{n} \;=\; \text{unit surface normal pointing into } V_{\Sigma}.$$

$$\vec{E}'(P) \;=\; \text{electric field due to the source } \vec{p}\,' \text{ in the presence of the}$$

$$\text{termination, evaluated at } P,$$

$$\vec{E}_i(P') \;=\; \text{electric field due to the source } \vec{p} \text{ in the absence of the}$$

$$\text{termination, evaluated at } P'.$$

The surface integral of (C.8) is over the three surfaces which make up Σ as defined in (C.1),

$$\oint_{\Sigma} \left(\vec{E}' \times \vec{H}_i - \vec{E}_i \times \vec{H}' \right) \cdot \hat{n} dS \;=\; \int_{\Sigma_{\infty}+S_w+S_t} \left(\vec{E}' \times \vec{H}_i - \vec{E}_i \times \vec{H}' \right) \cdot \hat{n} dS.$$

$$\text{(C.9)}$$

On the surface at infinity Σ_{∞}, it can be shown that the integrand of (C.8) vanishes due to the radiation condition, so

$$\int_{\Sigma_{\infty}} \left(\vec{E}' \times \vec{H}_i - \vec{E}_i \times \vec{H}' \right) \cdot \hat{n} dS \;=\; 0. \qquad \text{(C.10)}$$

On the interior and exterior surfaces of the waveguide cavity walls S_w, it can be shown that the integrand of (C.8) also vanishes because the two sets of fields $\vec{E}', \vec{H}'$

235

and $\vec{E}_i, \vec{H}_i$ satisfy the same boundary conditions, so

$$\int_{S_w} \left(\vec{E}' \times \vec{H}_i - \vec{E}_i \times \vec{H}' \right) \cdot \hat{n} dS = 0. \tag{C.11}$$

(C.9)-(C.11) reduce (C.8) to

$$\int_{S_t} \left(\vec{E}' \times \vec{H}_i - \vec{E}_i \times \vec{H}' \right) \cdot \hat{n} dS = \vec{E}'(P) \cdot \vec{p} - \vec{E}_i(P') \cdot \vec{p}\,' \tag{C.12}$$

which only requires an integration of the fields over the cross-section S_t near the termination.

By replacing $\vec{E}'$ and $\vec{H}'$ in (C.12) with their incident and scattered components defined in (C.4), (C.12) becomes

$$\int_{S_t} \left(\vec{E}_i' \times \vec{H}_i - \vec{E}_i \times \vec{H}_i' \right) \cdot \hat{n} dS + \int_{S_t} \left(\vec{E}_s' \times \vec{H}_i - \vec{E}_i \times \vec{H}_s' \right) \cdot \hat{n} dS =$$

$$\vec{E}_i'(P) \cdot \vec{p} + \vec{E}_s'(P) \cdot \vec{p} - \vec{E}_i(P') \cdot \vec{p}\,'. \tag{C.13}$$

The first integral on the left side of (C.13) is a function of only the incident fields (in the absence of the termination), as are the first and last terms on the right side of (C.13). If the termination were not present, $\vec{E}_s'$ and $\vec{H}_s'$ would be zero so the second integral on the left side of (C.13) and the second term on the right would vanish, leaving only terms which depend on the incident fields. It therefore follows that (C.13) can be decoupled as

$$\vec{E}_i'(P) \cdot \vec{p} - \vec{E}_i(P') \cdot \vec{p}\,' = \int_{S_t} \left(\vec{E}_i' \times \vec{H}_i - \vec{E}_i \times \vec{H}_i' \right) \cdot \hat{n} dS \tag{C.14}$$

$$\vec{E}_s'(P) \cdot \vec{p} = \int_{S_t} \left(\vec{E}_s' \times \vec{H}_i - \vec{E}_i \times \vec{H}_s' \right) \cdot \hat{n} dS \tag{C.15}$$

The first of these equations (C.14) yields no useful information, but the second of these (C.15) is the desired reciprocity integral which gives the termination scattered field at P in terms of an integration of fields over the cross-section S_t near the termination inside the cavity.

236

Typically, $\vec{E}'_s$ is the desired quantity because it is the electric field due to $\vec{p}\,'$ which is scattered by the termination. $\vec{E}'_i$ is also of interest because it includes all other scattering by the open-ended cavity, such as the scattering by the rim at the open end and the scattering due to energy which couples into the cavity which is reflected back before it reaches the termination. The total field at P due to the source $\vec{p}\,'$ is of course the sum of these two incident and scattered fields. It is noted that (C.15) intrinsically includes all multiple wave interactions between the open end of the cavity and the termination; however, in practice it may be very difficult to include these multiple interactions in evaluating $\vec{E}'_s$ and $\vec{H}'_s$ at the plane S_t in (C.15). Luckily, for most realistic applications these higher order effects can be neglected because the first order reflection of incident energy by the termination is usually by far the most dominant. The multiple wave interactions could be added separately if so desired, but this leads to a very complicated analysis which is usually not necessary because these higher order effects are not of primary interest. See Chapter II on the multiple scattering matrix (MSM) method as applied to the hybrid modal method, for a further discussion of multiple interaction effects.

In the following it is assumed that $\vec{E}'_i$, $\vec{H}'_i$, $\vec{E}_i$ and $\vec{H}_i$ are known a priori using methods such as those discussed in this report and elsewhere in the literature. It is also assumed that the fields from $\vec{p}\,'$ reflected by the termination, $\vec{E}'_s$ and $\vec{H}'_s$, are known at the cross-section S_t but without the multiple wave interactions with the open end of the cavity as discussed above. From these, the termination scattered field $\vec{E}'_s$ at P can be found using (C.15) without having to track the fields from the termination back down the waveguide to radiate from the open end.

$\vec{E}'_s(P)$ can now be extracted from (C.15) by choosing an appropriate $\vec{p}$. For example, to find the $\hat{x}$ component of the scattered field, simply replace $\vec{p}$ in (C.15)

with $\hat{x}$ to obtain

$$
\begin{aligned}
E'_{sx}(P) &= \vec{E}'_s(P) \cdot \hat{x} \\
&= \vec{E}'_s(P) \cdot \vec{p}\,\Big|_{\vec{p}=\hat{x}}
\end{aligned}
\tag{C.16}
$$

where

$$
E'_{sx}(P) = \hat{x} \text{ component of } \vec{E}'_s(P).
$$

At this point it may be useful to review the fields radiated from an infinitesimal electric current element $\vec{p}$ in free space, for use in identifying the fields incident on the open end of the cavity from the sources at P and P'. The electric field $\vec{E}_{\vec{p}}$ of such a current element is given by

$$
\vec{E}_{\vec{p}}(\vec{R}) = -\hat{R} \times \hat{R} \times \vec{p}\,\frac{jkZ_o}{4\pi R}e^{-jkR}, \text{ for } kR \gg 1
\tag{C.17}
$$

where

$$
\vec{R} = \hat{R}R = \text{ vector from the current element to the receiver.}
$$

The magnetic field radiated by an electric current element is then given by

$$
\vec{H}_{\vec{p}}(\vec{R}) = \frac{1}{Z_o}\hat{R} \times \vec{E}_{\vec{p}}(P).
\tag{C.18}
$$

For the present case, $\vec{R}$ would be the vector from the source at P or P' to some point in the vicinity of the open end of the waveguide cavity.

C.2 Modal Form of the Termination Reciprocity Integral

If the termination of the open-ended waveguide cavity is complex, as shown in Figure 95, finding the fields E'_s and H'_s in the integral of (C.15) may be difficult. However, if the region of the cavity near the termination is a uniform waveguide

section for which the waveguide modal fields are known, then the scattered fields $\vec{E}_s'$ and H_s' can be found in terms of the incident fields E_i' and H_i' using the modal termination reflection matrix $[S_\Gamma]$ described in Chapter II (assuming of course that $[S_\Gamma]$ is known). For example, the region near the termination in Figure 95 is a circular waveguide, as is most often the case for realistic geometries. First, the incident and scattered fields in the vicinity of the termination are expanded as a sum of N ortho-normal waveguide modes propagating in the $\pm\hat{\eta}$ directions as

$$\left(\vec{E}_i, \vec{H}_i\right) = \sum_{n=1}^{N} A_n^+ \left(\hat{e}_n^+, \hat{h}_n^+\right) e^{-j\beta_n \eta} \tag{C.19}$$

$$\left(\vec{E}_i', \vec{H}_i'\right) = \sum_{n=1}^{N} A_n^{+\prime} \left(\hat{e}_n^+, \hat{h}_n^+\right) e^{-j\beta_n \eta} \tag{C.20}$$

$$\left(\vec{E}_s', \vec{H}_s'\right) = \sum_{n=1}^{N} A_n^{-\prime} \left(\hat{e}_n^-, \hat{h}_n^-\right) e^{j\beta_n \eta} \tag{C.21}$$

where

$\hat{e}_n^\pm, \hat{h}_n^\pm$ = n^{th} electric and magnetic waveguide modal fields propagating in the $\pm\hat{\eta}$ directions, respectively,

β_n = propagation constant of the nth modal field,

η = axial coordinate of the waveguide, increasing towards the termination.

The modal reflection matrix $[S_\Gamma]$ then relates the incident modal coefficients to the reflected modal coefficients, as

$$[A^{-\prime}] = [S_\Gamma][A^{+\prime}] \tag{C.22}$$

where $[A^{\pm\prime}]$ are column matrices of order N composed of the modal coefficients $A_n^{\pm\prime}$ and $[S_\Gamma]$ is a square matrix of order $N \times N$. These modal fields are illustrated in Figure 98. Notice that the region near the cavity termination is modeled by
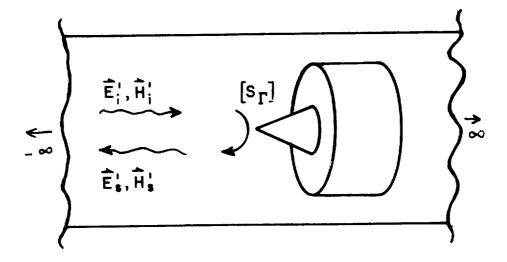
Figure 98: Modal reflection of fields from a termination.

a semi-infinite uniform waveguide in Figure 98. See Chapter II for a more complete discussion on waveguide modal methods, and especially Section 2.2.4 on the termination reflection matrix $[S_\Gamma]$.

The waveguide modal fields in (C.19)-(C.20) can be decoupled into transverse (to $\hat{\eta}$) and axial ($\hat{\eta}$) components as

$$\hat{e}_n^\pm = \hat{e}_{nt} \pm \hat{\eta} e_{n\eta} \tag{C.23}$$

$$\hat{h}_n^\pm = \pm \hat{h}_{nt} + \hat{\eta} h_{n\eta} \tag{C.24}$$

where

$\hat{e}_{nt}, \hat{h}_{nt}$ = transverse components of the nth electric and magnetic modal fields, respectively,

$e_{n\eta}, h_{n\eta}$ = scalar portions of the axial component of the nth electric and magnetic modal fields, respectively.

240

The ortho-normality property of these modes can then be expressed as

$$\int\int_{S_c} \left(\hat{e}_{it} \times \hat{h}_{jt} \right) \cdot \hat{\eta} \, dS \;=\; \delta_{ij} \tag{C.25}$$

where

$$\delta_{ij} \;=\; \begin{cases} 1 & : \text{ if } i = j \\[2mm] 0 & : \text{ if } i \neq j \end{cases} \tag{C.26}$$

$$S_c \;=\; \text{any planar cross-section of the waveguide,}$$

which states that each mode carries unit power, independently of all other modes. This ortho-normality condition can be used to simplify the termination reciprocity integral of (C.15) using (C.19) and (C.20) thru (C.24). (C.15) then becomes

$$
\begin{aligned}
\vec{E}'_s(P) \cdot \vec{p} \;=\; & -\int\int_{S_t} \left[\sum_{m=1}^{N} A_m^+ (\hat{e}_{mt} + \hat{\eta} e_{m\eta}) \right] \\
& \times \left[\sum_{n=1}^{N} A_n^{-\prime} \left(-\hat{h}_{nt} + \hat{\eta} h_{n\eta} \right) \right] \cdot (-\hat{\eta}) \, dS \\
& + \int\int_{S_t} \left[\sum_{n=1}^{N} A_n^{-\prime} (\hat{e}_{nt} - \hat{\eta} e_{n\eta}) \right] \\
& \times \left[\sum_{m=1}^{N} A_m^+ \left(\hat{h}_{mt} + \hat{\eta} h_{m\eta} \right) \right] \cdot (-\hat{\eta}) \, dS \\
\;=\; & -\sum_{m=1}^{N} \sum_{n=1}^{N} A_m^+ A_n^{-\prime} \int\int_{S_t} \left(\hat{e}_{mt} \times \hat{h}_{nt} \right) \cdot \hat{\eta} \, dS \\
& + \sum_{m=1}^{N} \sum_{n=1}^{N} A_m^+ A_n^{-\prime} \int\int_{S_t} \left(\hat{e}_{nt} \times \hat{h}_{mt} \right) \cdot \hat{\eta} \, dS \\
\;=\; & -2 \sum_{m=1}^{N} \sum_{n=1}^{N} A_m^+ A_n^{-\prime} \delta_{mn} \\
\vec{E}'_s(P) \cdot \vec{p} \;=\; & -2 \sum_{n=1}^{N} A_n^+ A_n^{-\prime}.
\end{aligned}
\tag{C.27}
$$

This result along with (C.22) can be used to find the termination scattered field $\vec{E}'_s(P)$, if the coefficients A_n^+ and $A_n^{+\prime}$ of the incident modal fields of (C.19) and (C.20) are known.

If the coefficients of the incident modal fields are not known, they can be found easily from the incident fields, again using the ortho-normality property of the modes. From (C.19), assuming $\eta = 0$ is chosen to coincide with the cross-section S_t,

$$\vec{H}_i = \sum_{m=1}^{N} A_m^+ \hat{h}_m^+.$$ (C.28)

Crossing both sides of this with $\hat{e}_{nt}$ and integrating the dot product of this with $\hat{\eta}$ over S_t gives

$$
\begin{aligned}
\int\!\int_{S_t} \left(\hat{e}_{nt} \times \vec{H}_i \right) \cdot \hat{\eta} dS &= \int\!\int_{S_t} \left(\hat{e}_{nt} \times \sum_{m=1}^{N} A_m^+ \hat{h}_m^+ \right) \cdot \hat{\eta} dS \\
&= \sum_{m=1}^{N} A_m^+ \int\!\int_{S_t} \left(\hat{e}_{nt} \times \hat{h}_{mt} \right) \cdot \hat{\eta} dS \\
&= \sum_{m=1}^{N} A_m^+ \delta_{nm} = A_n^+.
\end{aligned}
$$

So,

$$A_n^+ = \int\!\int_{S_t} \left(\hat{e}_{nt} \times \vec{H}_i \right) \cdot \hat{\eta} dS.$$ (C.29)

and similarly,

$$A_n^{+\prime} = \int\!\int_{S_t} \left(\hat{e}_{nt} \times \vec{H}_i^{\prime} \right) \cdot \hat{\eta} dS.$$ (C.30)

In other words, the modal coefficient of the nth incident waveguide mode is found by the integrating the cross product of transverse component of the electric field of the nth mode and the incident magnetic field at S_t. The incident magnetic field is found by tracking the fields coupled through the open end from $\vec{p}$ and $\vec{p}\,'$, down the waveguide cavity to the cross-section S_t using, for example, one of the methods described in this report.

C.3 Plane Wave Bistatic Scattering Using the Termination Reciprocity Integral

The plane wave bistatic scattering by an open-ended waveguide cavity can be found using the termination reciprocity integral of (C.15) by letting the sources at P and P' recede to infinity. The co-polarized and cross-polarized bistatic radar cross-sections (RCS), or "echo areas", are usually the figures of interest. In terms of $\hat{\theta}$ and $\hat{\phi}$ polarizations, the two co-polarized echo widths are $\sigma_{\theta\theta}$ and $\sigma_{\phi\phi}$ and the two cross-polarized echo widths are $\sigma_{\theta\phi}$ and $\sigma_{\phi\theta}$. For example, $\sigma_{\theta\phi}$ is defined by

$$\sigma_{\theta\phi} = \lim_{r \to \infty} 4\pi r^2 \frac{\left|E'_{s\theta}(P)\right|^2}{\left|E'_{o\phi}\right|^2} \qquad (C.31)$$

where

$$
\begin{aligned}
E'_{s\theta}(P) &= \vec{E}'_s(P) \cdot \vec{p}\,\Big|_{\vec{p}=\hat{\theta}} \qquad\qquad (C.32)\\
&= \hat{\theta} \text{ component of the scattered field at } P,\\
r &= \text{distance from the open end of the cavity to } P \text{ and } P',\\
E'_{o\phi} &= \text{magnitude of the } \hat{\phi} \text{ polarized plane wave field incident on the}\\
&\quad\ \text{cavity from the direction of } P'.
\end{aligned}
$$

The other three bistatic echo widths are defined in exactly the same manner with appropriate interchanges of θ and ϕ.

(C.31) can be simplified using (C.17). The plane wave field due to the $\hat{\theta}$ oriented current element at P incident on the cavity can be written as

$$\vec{E}_{\vec{p}}(\vec{R})\Big|_{\vec{p}=\hat{\theta}} = \lim_{R \to \infty} -\hat{R} \times \hat{R} \times \hat{\theta}\, \frac{jkZ_o}{4\pi R} e^{-jkR} \qquad (C.33)$$

where

$$\vec{R} = -\vec{r} \qquad (C.34)$$

243

$=$ vector from P to the open end of the cavity.

Using (C.34), (C.33) becomes

$$\vec{E}_{\vec{p}}(\vec{r})\Big|_{\vec{p}=\hat{\theta}} = \lim_{r \to \infty} \hat{\theta}\, \frac{jkZ_o}{4\pi r}e^{jkr}$$

$$= \hat{\theta}E_{o\theta}e^{jkr} \tag{C.35}$$

where

$$E_{o\theta} = \lim_{r \to \infty} \frac{jkZ_o}{4\pi r} \tag{C.36}$$

$=$ magnitude of the $\hat{\theta}$ polarized plane wave field incident on the

cavity from the direction of P.

Therefore, from (C.36)

$$\lim_{r \to \infty} 4\pi r^2 = 4\pi \left| \frac{jkZ_o}{4\pi E_{o\theta}} \right|^2$$

$$= \frac{(kZ_o)^2}{4\pi \left| E_{o\theta} \right|^2} \tag{C.37}$$

which makes (C.31) become

$$\sigma_{\theta\phi} = \frac{(kZ_o)^2}{4\pi} \frac{\left| E'_{s\theta}(P) \right|^2}{\left| E_{o\theta} \right|^2 \left| E'_{o\phi} \right|^2}. \tag{C.38}$$

The other three bistatic echo widths are found using this same equation with the appropriate interchanges of θ and ϕ. The form of (C.38) is easy to use computationally because the echo width is given in terms of the scattered field found using the termination reciprocity integral as in (C.32) and (C.15) or (C.27), and in terms of the components of the plane waves incident on the cavity from the directions of P and P'. The monostatic RCS (backscatter echo area) is found by simply making P and P' the same point.

244

APPENDIX D

SUB-APERTURE FIELD EXPANSION METHOD IN 2-D

The method of expanding the fields in an aperture in terms of the fields of smaller sub-apertures which make up the aperture is described in this appendix. For simplicity, the derivation is for the two dimensional (2-D) case. The extension to 3-D is straightforward and is not included in this appendix, but is described for application to the generalized ray expansion method in Chapter V.

Figure 99 shows the geometry of an aperture in the $z = 0$ plane with a known incident field $\vec{U}_i(x)$ inside the aperture. Throughout this appendix, $\vec{U}$ represents the field which is normal to the plane of the page, either electric or magnetic, depending on polarization. U means "the scalar portion of $\vec{U}$".

Using equivalent currents in the aperture and the 2-D radiation integral, the field for $z > 0$ is given by

$$U(\rho, \theta) \;=\; 2\sqrt{\frac{jk}{8\pi}}\cos\theta \int_{-\frac{d}{2}}^{\frac{d}{2}} U_i(x')\frac{e^{-jk\rho'}}{\sqrt{\rho'}}dx' \tag{D.1}$$

where

$k \;\;=\;\;$ free space wave number $2\pi/\lambda$,

$\lambda \;\;=\;\;$ free space wavelength,

$\rho' \;\;=\;\;$ distance from a point in the aperture $(x', 0)$, to a field point (ρ, θ).
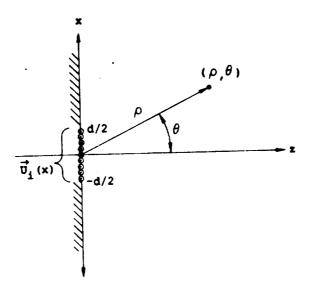
Figure 99: Geometry of an aperture with a known incident field.

The aperture integral in (D.1) can be broken up into $2M + 1$ equally sized sub-aperture integrals of width Δ:

$$\int_{-\frac{d}{2}}^{\frac{d}{2}} U_i(x') \frac{e^{-jk\rho'}}{\sqrt{\rho'}} dx' = \sum_{m=-M}^{M} \int_{(m-\frac{1}{2})\Delta}^{(m+\frac{1}{2})\Delta} U_i(x') \frac{e^{-jk\rho'}}{\sqrt{\rho'}} dx' \qquad (D.2)$$

where

$$\Delta = \frac{d}{2M+1}. \qquad (D.3)$$

Define a new variable of integration,

$$x'_m = x' - m\Delta \qquad (D.4)$$

and define ρ_m and θ_m as shown in Figure 100 for the mth sub-aperture. ρ' is now given by

$$\rho' = \sqrt{\rho_m^2 + x_m'^2 - 2\rho_m x'_m \sin \theta_m}. \qquad (D.5)$$

where

ρ_m, θ_m = polar coordinates of the mth sub-aperture with their origin

at $(x, z) = (m\Delta, 0)$.
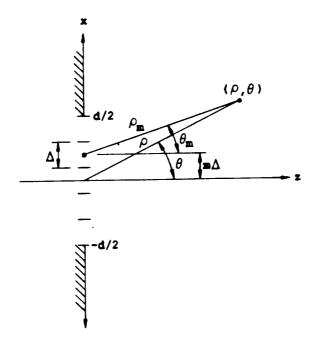
246

Figure 100: Geometry of the mth sub-aperture defining ρ_m and θ_m.

Keeping the first three terms in the Taylor series for ρ' expanded around $x'_m = 0$ gives

$$\rho' \approx \rho_m - x'_m \sin\theta_m + \frac{1}{2}\frac{x'^2_m}{\rho_m} - \frac{1}{8}\frac{(x'^2_m - 2\rho_m x'_m \sin\theta_m)^2}{\rho^3_m}. \qquad \text{(D.6)}$$

Getting rid of all terms of higher order than quadratic reduces (D.6) to

$$\rho' \approx \rho_m - x'_m \sin\theta_m + \frac{1}{2}\frac{x'^2_m}{\rho_m}\cos^2\theta_m. \qquad \text{(D.7)}$$

The quadratic term can be dropped if its phase contribution to the exponential term of (D.2) is small enough, i.e., if

$$k\frac{1}{2}\frac{x'^2_m}{\rho_m}\cos^2\theta_m \quad < \quad \frac{\pi}{8}. \qquad \text{(D.8)}$$

Then

$$\rho' \approx \rho_m - x'_m \sin\theta_m, \qquad \text{(D.9)}$$

where it is assumed that $\pi/8$ is a small enough phase to be negligible. The maximum value that x'_m can attain is $\Delta/2$. Substituting this into (D.8) for x'_m and
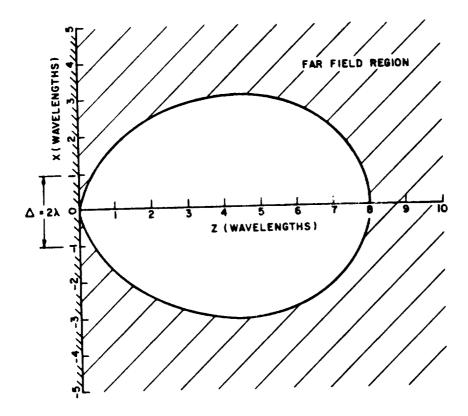
247

Figure 101: Far field region of an aperture of width $\Delta = 2\lambda$.

rearranging yields the result

$$\rho_m \ > \ 2\frac{\Delta^2}{\lambda}\cos^2\theta_m \qquad\qquad (D.10)$$

which is the far field condition often encountered in aperture antenna problems. This region is plotted in Figure 101 for a sub-aperture of width $\Delta = 2\lambda$. (D.10) can be rewritten as

$$\frac{\rho_m}{\Delta} \ > \ 2\frac{\Delta}{\lambda}\cos^2\theta_m \qquad\qquad (D.11)$$

which shows that the far field distance relative to the sub-aperture size increases as the sub-aperture gets large in terms of wavelength. In other words, the distance to far field increases with frequency. The inequality of (D.10) or (D.11) is important

248

because it determines how close the observer can be to the sub-aperture and still use the far field form of the radiation integral for a given sub-aperture size.

Substituting the far field form of ρ' (D.8) back into (D.2) along with the change of variables in (D.4) and integrating reduces (D.2) to

$$\int_{(m-\frac{1}{2})\Delta}^{(m+\frac{1}{2})\Delta} U_i(x')\frac{e^{-jk\rho'}}{\sqrt{\rho'}}dx' \approx \frac{e^{-jk\rho m}}{\sqrt{\rho m}} \int_{-\frac{1}{2}\Delta}^{\frac{1}{2}\Delta} U_i(x'_m + m\Delta)e^{jkx'_m \sin\theta_m}dx'_m$$

(D.12)

which is recognized as a simple Fourier transform relationship. Therefore, the fields radiating from a sub-aperture look like they are due to a non-isotropic line source located in the middle of the sub-aperture with a pattern given by the Fourier transform integral in (D.12).

Substituting this result into (D.2) and (D.2) into (D.1) gives the fields radiating from the full aperture,

$$U(\rho,\theta) = 2\sqrt{\frac{jk}{8\pi}}\cos\theta \sum_{m=-M}^{M} \frac{e^{-jk\rho m}}{\sqrt{\rho m}} \int_{-\frac{1}{2}\Delta}^{\frac{1}{2}\Delta} U_i(x'_m + m\Delta)e^{jkx'_m \sin\theta_m}dx'_m$$

(D.13)

which is valid anywhere as long as the observer is in the far field of all the sub-apertures, according to (D.10). (D.13) says that the fields radiating from an aperture can be represented by a discrete array of non-isotropic line sources which is valid even in the near field of the aperture, subject to the constraint of (D.10).

One advantage of using the sub-aperture expansion of (D.13) is that the far field region of each sub-aperture is much closer to the aperture plane than the far field region of the whole aperture which is given by

$$\rho > 2\frac{d^2}{\lambda}\cos^2\theta.$$

(D.14)

Inspection of (D.3) and (D.10) indicates that the fields of the whole aperture can be found arbitrarily close to the aperture plane using (D.13) by increasing the

number of sub-apertures $(2M + 1)$ appropriately. However, the main advantage of using the sub-aperture expansion technique is that the fields from any particular sub-aperture appear to be originating from a source located at the center of the sub-aperture, provided the observer is in the far field of the sub-aperture. This allows the fields from a particular sub-aperture to be traced in the presence of obstructions, such as waveguide walls, as long as these obstructions are in the far field region of the sub-aperture, using an appropriate field tracing method. The Gaussian beam shooting method developed in Chapter IV and the Generalized Ray Expansion method of Chapter V are examples. However, as is seen in Section 4.3, the Gaussian beam expansion is accurate at any distance from the aperture, not just in the far field of the sub-apertures.

The most common form of excitation of the aperture for scattering problems is a plane wave because it represents a source located at infinity, such as a radar antenna. This is the excitation used throughout this report, although any general aperture field $U_i(x')$ could be used. Therefore, as an example, let the incident field be due to a plane wave which propagates from left to right at an angle of θ_i with the z-axis, as shown in Figure 102. Using the Kirchhoff approximation, the incident field in the aperture is given by

$$U_i(x') = U_o e^{-jkx' \sin \theta_i}. \tag{D.15}$$

where

U_o = magnitude of the incident plane wave,

θ_i = angle between the direction of propagation of the incident plane wave and the z-axis.
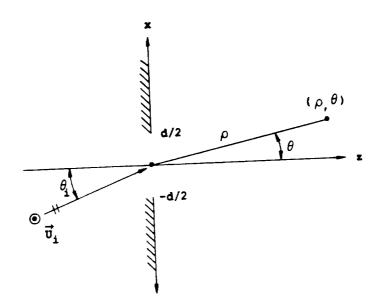
250

Figure 102: Plane wave field incident on an aperture of width d in the $z = 0$ plane.

Integrating (D.15) in (D.13) gives the fields radiating from the aperture as

$$
U(\rho,\theta) \;=\; 2U_o\sqrt{\frac{jk}{8\pi}}\,\Delta \sum_{m=-M}^{M} \frac{e^{-jk(\rho_m + m\Delta\sin\theta_i)}}{\sqrt{\rho_m}}\,\mathrm{sinc}\left[\frac{1}{2}k\Delta(\sin\theta_m - \sin\theta_i)\right]
$$

(D.16)

where

$$
\mathrm{sinc}(x) \;=\; \frac{\sin x}{x}.
$$

(D.17)

The Kirchhoff approximation used in (D.15) is very accurate for high frequencies and values of θ_i and θ which are not too close to grazing. A more accurate representation could be found using, for example, the Physical Theory of Diffraction (PTD) [11], but the improvement in accuracy would usually not be enough to outweigh the added complexity for realistic aperture sizes.

REFERENCES

[1] J.B. Keller, "Geometrical Theory of Diffraction," J. Opt. Soc. Am., Vol. 52, pp. 116-130, 1962.

[2] R.G. Kouyoumjian and P.H. Pathak, "A Uniform Geometrical Theory of Diffraction for an Edge in a Perfectly Conducting Surface," Proc. IEEE, Vol. 62, pp. 1448-1461, November 1974.

[3] P.H. Pathak, "Techniques for High Frequency Problems," Chapter 4 in ANTENNA HANDBOOK - Theory, Applications, and Design, eds. Y.T. Lo and S.W. Lee, Van Nostrand Reinhold, 1988.

[4] R. Mittra and S.W. Lee, Analytical Techniques in the Theory of Guided Waves, The Macmillan Company, New York, 1971.

[5] P.H. Pathak, C.W. Chuang and M.C. Liang, "Inlet Modeling Studies," The Ohio State University ElectroScience Laboratory Technical Report 717674-1, prepared under Contract No. N60530-85-C-0249, for Naval Weapons Center, China Lake, California, October 1986.

[6] A. Altintas, P.H. Pathak, W.D. Burnside, "Electromagnetic Scattering from a Class of Open-Ended Waveguide Discontinuities," The Ohio State University ElectroScience Laboratory Technical Report 716148-9, prepared under Grant No. NSG-1613, for NASA/Langley Research Center, Hampton, Virginia, March 1986.

[7] R.J. Burkholder, C.W. Chuang, and P.H. Pathak, "Electromagnetic Fields Backscattered from an S-Shaped Inlet Cavity with an Absorber Coating on its Inner Walls," The Ohio State University ElectroScience Laboratory Final Report No. 715723-2, prepared under Grant NAG 3-476, for NASA/Lewis Research Center, Cleveland, Ohio, July 30, 1987.

[8] C.W. Chuang, P.H. Pathak, R.J. Burkholder, "A Hybrid Asymptotic Modal-Moment Method Analysis of the EM Scattering by 2-D Open-Ended Linearly Tapered Waveguide Cavities," The Ohio State University ElectroScience Laboratory Technical Report No. 312436-1, prepared for McDonnel Douglas Corporation, St. Louis, MO, December 1988.

[9] P.H. Law, R.J. Burkholder, and P.H. Pathak, "A Hybrid Asymptotic-Modal Analysis of the EM Scattering by an Open-Ended S-Shaped Rectangular Waveguide Cavity," The Ohio State University ElectroScience Laboratory Technical Report No. 719630-2, prepared under Grant NAG 3-476, for NASA/Lewis Research Center, Cleveland, Ohio, December 1988.

252

[10] W.D. Burnside and L. Peters, Jr., "Axial RCS of Finite Cones by the Equivalent Current Concept with Higher Order Diffraction," Radio Science, Vol. 7, No. 10, pp. 943-948, October 1972.

[11] P.Ya. Ufimtsev, "Method of Edge Waves in the Physical Theory of Diffraction," (from the Russian "Method Krayevykh voin v fizicheskoy teoril difraktsii," Izd-Vo Sov. Radio, pp. 1-243 (1962), translation prepared by the U.S. Air Force Foreign Technology Division, Wright-Patterson Air Force Base, Ohio; released for public distribution September 7, 1971.

[12] S.W. Lee, "Comparison of Uniform Asymptotic Theory and Ufimtsev's Theory of EM Edge Diffraction," IEEE Trans. on Antennas and Propagation, Vol. AP-25, No. 2, pp. 162-170, March 1977.

[13] A. Altintas, P.H. Pathak, and M.C. Liang, "A Selective Modal Scheme for the Analysis of EM Coupling into or Radiation from Large Open- Ended Waveguides," Trans. on Antennas and Propagation, Vol. 36, No. 1, pp. 84-96, January 1988.

[14] R.J. Burkholder, "Backscatter Analysis of Two Conducting Inlets," Master's Thesis, The Ohio State University, Department of Electrical Engineering, Columbus, Ohio, August 1985.

[15] N.H. Myung and P.H. Pathak, "A High Frequency Analysis of Electromagnetic Plane Wave Scattering by perfectly-conducting Semi- Infinite Parallel Plate and Rectangular Waveguides with Absorber Coated Inner Walls," The Ohio State University ElectroScience Laboratory Technical Report 715723-1, prepared under Grant NSG 3- 476, for NASA/Lewis Research Center, Cleveland, Ohio, September 1986.

[16] R. Chou, H. Ling and S.W. Lee, "Reduction of the Radar Cross Section of Arbitrarily Shaped Cavity Structures," Electromagnetics Laboratory Report No. 87-6, prepared under support of NASA/Lewis Research Center, Cleveland, Ohio under Contract NAG3-475 and by the NSF under Contract ECS 83-11345, August 1987.

[17] H. Ling, R. Chou and S.W. Lee, "Shooting and Bouncing Rays: Calculating RCS of an Arbitrary Cavity", IEEE Trans. on Antennas and Propagation, Vol. AP-37, No. 2, pp. 194-205, February 1989.

[18] S.W. Lee, H. Ling and R. Chou, "Ray-Tube Integration in Shooting and Bouncing Ray Method", Microwave and Optical Tech. Letters, Vol. 1, No. 8, October 1988.

[19] S.W. Lee and R. Chou, "A Versatile Reflector Antenna Pattern Computation Method: Shooting and Bouncing Rays," Microwave and Optical Technology Letters, Vol. 1, pp. 81-87, 1988.

[20] G.A. Deschamps, "Ray techniques in electromagnetics", Proc. IEEE, Vol. 60, pp. 1022-1035, September 1972.

[21] S.W. Lee, P. Cramer, Jr., K.Woo, and Y. Rahmat-Samii, "Diffraction by an arbitrary subreflector: GTD solution", IEEE Trans. on Antennas and Propagation, Vol. AP-27, pp. 305-316, May 1979 (Correction, Vol. AP-34, p. 272, Feb. 1986).

[22] S.W. Lee, M.S. Sheshadri, V. Jamnejad and R. Mittra, "Reflection at a curved dielectric interface : geometrical optics solution", IEEE Trans. Microwave Theory and Techniques, Vol. MTT-30, pp. 12-19, January 1982.

[23] H. Shirai and L.B. Felsen, "Rays, Modes and Beams for Plane Wave Coupling into a Wide Open-Ended Parallel-Plane Waveguide," Wave Motion, Vol. 9, pp. 301-317, 1987.

[24] H. Shirai and L.B. Felsen, "Rays and Modes for Plane Wave Coupling into a Large Open-Ended Circular Waveguide," Wave Motion, Vol. 9, pp. 461-482, 1987.

[25] L.B. Felsen and S.Y. Shin, "Rays, Beams, and Modes Pertaining to the Excitation of Dielectric Waveguides," IEEE Trans. on Microwave Theory and Techniques, Vol. MTT-23, No. 1, pp. 150-161, January 1975.

[26] J.J. Maciel and L.B. Felsen, "Systematic Study of Fields Due to Extended Apertures by Gaussian Beam Discretization," submitted to IEEE Trans. on Antennas and Propagation.

[27] J. Maciel and L.B. Felsen, "Gaussian Beam Analysis of Propagation from an Extended Plane Aperture Distribution Through Plane and Curved Dielectric Layers," Digest of the National Radio Science Meeting, Univ. of Colorado, Boulder, p.96, Jan. 4-6, 1989.

[28] D. Gabor, "Theory of Communication," J. Inst. Elec. Eng. (London) 93III, 429-457 (1946).

[29] M.J. Bastiaans, "Gabor's Expansion of a Signal into Gaussian Elementary Signals," Proc. IEEE 68, 538-539 (1980).

[30] P.H. Pathak, R.J. Burkholder, Internal memorandum on the use of a generalized reciprocity theorem to deal with the scattering by an arbitrary termination within an otherwise open-ended cavity, 1988. A paper describing this work is in preparation.

[31] R.E. Collin, Foundations of Microwave Engineering, McGraw-Hill, New York, 1966.

[32] R.F. Harrington, Time Harmonic Electromagnetic Fields, McGraw Hill, New York, 1961.

[33] G.A. Deshamps, "The Gaussian Beam as a Bundle of Complex Rays", Electronics Letters, Vol. 7, No. 23, pp. 684-685, Nov. 18, 1971.

[34] J.W. Ra, H.L. Bertoni, and L.B. Felsen, "Reflection and Transmission of Beams at a Dielectric Interface", SIAM J. Appl. Math., Vol. 24, No.3, pp. 396-413, May 1973.

[35] Y.Z. Ruan and L.B. Felsen, "Reflection and Transmission of Beams at a Curved Interface," J. Optical Society of America, Vol. 3, No. 4, pp. 566-578, April 1986.

[36] F.J.V. Hasselmann and L.B. Felsen, "Asymptotic Analysis of Parabolic Reflector Antennas", IEEE Trans. on Antennas and Propagation, Vol. AP-30, No. 4, pp. 677-685, July 1982.

[37] S.Y. Shin and L.B. Felsen, "Multiply Reflected Gaussian Beams in a Circular Cross Section", IEEE Trans. on Microwave Theory and Techniques, Vol. MTT-26, No. 11, pp. 845-851, November 1978.

[38] H. Ling, S.W. Lee, and R.C. Chou, "High-Frequency RCS of Open Cavities with Rectangular and Circular Cross Sections", IEEE Trans. on Antennas and Propagation, Vol. AP-37, No. 5, pp. 648-654, May 1989.